

Exploring the links between quasar winds and radio emission along the Main Sequence at high redshift[★]

A. Deconto-Machado¹, A. del Olmo¹, and P. Marziani²

¹ Instituto de Astrofísica de Andalucía, IAA-CSIC, E-18008, Granada, Spain
e-mail: adeconto@iaa.es, chony@iaa.es

² INAF, Osservatorio Astronomico di Padova, IT 35122, Padova, Italy
e-mail: paola.marziani@inaf.it

Received ; accepted

ABSTRACT

Context. Despite the increasing prevalence of radio-loud (RL) sources at cosmic noon, our understanding of the underlying physics that governs the accretion disc outflows in these particular sources and its dissimilarity with radio-quiet (RQ) quasars remains somewhat limited.

Aims. Disentangling the real impact of the radio-loudness and accretion on the outflow parameters remains a challenge to this day. We present 10 new spectra of high-redshift and high-luminosity quasars and combine it with previous data at both high and low redshift with the aim to evaluate the role of the feedback from RL and RQ AGN. The final high-redshift ($1.5 \lesssim z \lesssim 3.9$) high-luminosity ($47.1 \leq \log(L) \leq 48.5$) sample consists of a combination of 60 quasars from our ISAAC and the Hamburg-ESO surveys. The low-redshift ($z \leq 0.8$) sample has 84 quasars with optical and Faint Object Spectrograph (FOS) reanalyzed data.

Methods. We perform a multicomponent analysis of optical and UV emission line profiles along the quasar main sequence, and provide a relation to estimate the outflow main parameters (mass rate, thrust and kinetic power) in both the BLR and NLR through the analysis of the [O III] λ 5007 and C IV λ 1549 emission lines.

Results. Spectrophotometric properties and line profile measurements are presented for H β + [O III] λ 4959,5007, Si IV λ 1397+O IV λ 1402, C IV λ 1549+He II λ 1640, and the 1900Å blend. High-ionization lines as such C IV λ 1549 and [O III] λ 5007 usually present a significant asymmetry towards the blue especially in radio-quiet sources that is strong evidence of outflow motions. In the ISAAC sample, 72% of the quasars where [O III] is clearly detected present significant outflows, with centroid velocity at half intensity blueshifted to values greater than $\sim 250 \text{ km s}^{-1}$. Radio-loud quasars tend to present slightly more modest blueshifted components in both the UV and optical ranges. The behavior of [O III] λ 5007 mirrors the one of C IV λ 1549, with blueshift amplitudes between the two lines showing a high degree of correlation that appears unaffected by the presence of radio emission.

Conclusions. In contrast to low redshift, both RL and RQ AGN outflow parameters at high luminosity appear in the range needed to provide feedback effects on their host galaxies. Both high- and low- z RL quasars exhibit smaller outflows compared to RQ, suggesting a potential role of radioloudness in mitigating outflow effects. Nevertheless, the radio-loudness effect on the AGN feedback is much less significant than the one of accretion that emerges as the main driver of the nuclear outflows.

Key words. quasars: general – quasars: emission lines – quasars: supermassive black holes

1. Introduction

It is now an established result that quasar spectra do not scatter randomly around an average and that a systematic scheme is needed to organize their spectral diversity. One of the most successful tools to analyze such objects makes use of independent observational properties obtained from the optical and UV emission lines, as well as from soft X-rays (the 4D Eigenvector 1 correlation space; Boroson & Green 1992; Sulentic et al. 2000b). As part of the 4DE1, it is possible to identify a sequence of quasars in the plane defined by two optical parameters: the full width at half maximum of the H β emission line (FWHM(H β)) and the ratio between the intensities of the blend of Fe II emission lines at 4570Å and H β (R_{FeII}). This relation has become to be known as the Main Sequence of quasars (MS; Sulentic et al. 2000a,b; Marziani et al. 2001; Shen & Ho 2014; Marziani et al. 2018). Several multi-frequency correlations associated with the MS are

well established at low redshift and low luminosity (e.g. see the summary tables in Sulentic et al. 2011; Fraix-Burnet et al. 2017).

At low-redshift, it appears that the jetted¹ (radio-loud, RL) sources show a preference for the Pop. B domain in the MS, while the radio-quiet (RQ) are distributed equally between Pop. A and Pop. B (Zamfir et al. 2008). This suggests potential differences in spectral and physical properties between RL and RQ sources. The phenomenology involves broader lines for RL with respect to RQ (as most RL are in Pop. B), and an optical spectrum showing lower Fe II and a higher ionization degree with respect to full samples of RQ quasars in both the BLR and the NLR (Marziani et al. 2003b; Zamfir et al. 2010; Kovačević-Dojčinović & Popović 2015; Coziol et al. 2017; Ganci et al. 2019). Consequently, the low- z radio-quiet sources seem to follow different distributions of Eddington ratio and black hole masses than the radio-loud ones (Woo & Urry 2002; Marziani et al. 2003a;

[★] Based on observations collected at ESO under programs 086.B-0774(A), 085.B-0162(A), and 083.B-0273(A).

¹ Here we define “jetted” sources the ones that present a radio loudness parameter $R_K \gtrsim 1.8$ (also called here as “radio-loud”, Ganci et al. 2019, see also §3.4).

Sikora et al. 2007; Fraix-Burnet et al. 2017). In general, at low- z , RQ sources are the ones that usually present smaller masses and larger Eddington ratio.

Outflows appear to be ubiquitous in both the BLR and NLR (e.g., Coatman et al. 2019; Vietri et al. 2020; Marziani et al. 2022b, and references therein). However, at low z mild-ionization gas outflows observed in jetted sources appear to be weaker than in the RQ ones (Marziani et al. 1996; Bachev et al. 2004; Punsly 2010; Richards et al. 2011). This may not be at odds with the higher ionization degree revealed in RLs (e.g., Buttiglione et al. 2010; Mengistue et al. 2023), although a full physical explanation is still missing, mainly due to the still-limited scope of detailed studies of accretion disk outflows in RL quasars. This difference between RQ and RL outflows is observed at both high- and low-redshift. A key distinction is however that at high redshift, the outflows appear significantly stronger compared to those at low redshift (Richards et al. 2011; Sulentic et al. 2017; Deconto-Machado et al. 2023). At low-redshift ranges, many authors found ionized gas outflows with kiloparsec scales, however their impact is only in the central region of the galaxies (e.g. Kim et al. 2023, and references therein).

More and more RL sources are being discovered at the cosmic noon (e.g., Patil et al. 2022; Breiding et al. 2023, and references therein). Their rest-frame optical properties remain poorly studied since they require high-S/N moderate dispersion IR spectroscopy. For this reason, we obtained new IR spectroscopic observations for other ten high-redshift ($z \sim 1.5 - 2.5$) and high-luminosity ($M_B \lesssim -27$) quasars. The targets are intended to cover the rest-frame $H\beta$ range, and include both RQ and jetted (or RL) objects, completing the sample reported in Deconto-Machado et al. (2023, hereafter Paper I). Our main aim is to clarify the origin of several phenomenological differences between RL and RQ and in particular the relation between accretion status, accretion disk outflows, and the presence of powerful relativistic ejections, exploiting the MS and its correlation with the $C\text{IV}\lambda 1549$ and $[\text{O III}]\lambda\lambda 4959, 5007$ emission.

In addition to the rest-frame optical data, we collected archival rest-frame UV data of the targets in the present paper and in Paper I, and we defined comparison samples for which both rest-frame UV and optical data are available (Section 2). The data analysis includes discussion about UV and optical regions for the two different quasar populations and the spectral types that have been defined along the quasar MS (Section 3). The measurements carried out in both the optical (Fe II , $H\beta$, $+\text{[O III]}\lambda\lambda 4959, 5007$) and UV ($\text{Si IV}\lambda 1397$, $\text{C IV}\lambda 1549$, and the 1900\AA blend) regions are reported in Section 4 whereas their interpretation in terms of the outflow dynamical parameters is presented in Section 5. We show that the RQ and RL population are both associated with high Eddington ratio at high luminosity, and that BLR and NLR scale outflows are consistently powerful, albeit being somewhat weaker in RL sources. This difference between RQ and RL outflows might be due to an apparently minor effect related to the propagation of the relativistic jet. In Section 6, we summarize the key findings and discuss some implications of our results.

2. Samples

2.1. The new ISAAC2 sample

New near-IR spectroscopic observations for ten quasars (hereafter ISAAC2 sample) were obtained to cover the high-redshift ($1.55 \leq z \leq 2.45$) and high-luminosity ($47.18 \leq \log L_{\text{bol}} \leq 48.14$ [erg s^{-1}]) ranges. The redshift range of this sample allows for

Table 1. Source identification.

Source (1)	RA (2)	DEC (3)	z (4)	δz (5)	m_H (6)	M_i (7)
PKS0226-038	02 28 53.26	-03 37 05.30	2.0692	0.0002	15.97	-28.55
PKS0237-23	02 40 08.17	-23 09 15.72	2.2298	0.0008	14.52	-29.79
BZQJ0544-2241	05 44 08.63	-22 40 37.10	1.5547	0.0003	14.90	-27.99
PKS0858-279	09 00 40.03	-28 08 20.35	2.1725	0.0007	13.65	-31.26
CTSJ01.03	09 39 51.10	-18 32 15.00	2.3754	0.0004	14.98	-30.07
WB J0948+0855	09 48 53.60	+08 55 14.45	1.9842	0.0016	15.17	-29.01
CTSJ03.14	10 18 21.75	-21 40 07.80	2.4493	0.0003	15.57	-28.51
PKS1448-232	14 51 02.50	-23 29 31.08	2.2264	0.0002	14.97	-29.13
[HB89]1559+088	16 02 22.73	+08 45 38.42	2.2837	0.0007	15.01	-29.02
FBQS J2149-0811	21 49 48.18	-08 10 16.60	2.1295	0.0002	15.74	-28.48

Notes. Column (1) Source identification according to the different catalogues. Columns (2) and (3) Right ascension (hh mm ss) and Declination (dd mm ss) respectively, at J2000 coordinates. (4) Redshift estimated as explained in Section 2.1. (5) Redshift uncertainty. (6) H -band apparent magnitude (m_H) from the 2-MASS catalogue. (7) i -band absolute magnitude M_i .

the detection and observation of the $H\beta + [\text{O III}]\lambda\lambda 4959, 5007$ region through the transparent window in the near-infrared with the ISAAC spectrograph at VLT. These spectra together with the ones from Paper I complete what we will call from now on the ISAAC sample (32 sources in total), which is described in more details in §2.2.

Table 1 lists the main properties of the ISAAC2 sample. The redshift was estimated using a similar approach to the one of Paper I. For five sources (PKS0226-038, PKS0858-279, CTSJ01.03, CTSJ03.14, and PKS1448-232), the redshift estimation relied on the observed wavelength of the narrow component (NC) of $H\beta$, which is also consistent with the central wavelength of the $[\text{O III}]$ NC. For PKS0237-23, BZQJ0544-2241, [HB89]1559+088, and FBQS J2149-0811, the redshift was determined using the broad component (BC) of $H\beta$, whose peak wavelength agrees with the peak of a very faint $H\beta$ NC in all cases except PKS0237-23 and [HB89]1559+088 where the NC is only barely detected. In the case of WB J0948+0855, the presence of strong telluric bands, combined with the fact that the $H\beta$ region is at the edge of the spectrum, significantly affect the estimation of the $H\beta$ peak centroid, leading to large uncertainties. Therefore, we used $\text{Mg II}\lambda\lambda 2796, 2803$ doublet from the SDSS UV spectrum to determine the redshift for this source (see Appendix A.6). The luminosity distance was estimated from the redshift using the approximation reported in Sulentic et al. (2006), valid for $\Omega_M = 0.3$, $\Omega_\Lambda = 0.7$, and $H_0 = 70 \text{ km s}^{-1} \text{ Mpc}^{-1}$.

2.2. The complete ISAAC sample

Our complete ISAAC sample comprises 32 quasars, consisting of 22 sources from Paper I, along with the ten new objects presented in this work. These quasars are characterized by high redshift values, ranging from $z = 1.55$ to $z = 3.80$, and high luminosity ($47.18 \lesssim \log L_{\text{bol}} \lesssim 48.36$ [erg s^{-1}]), including both radio-loud (10) and radio-quiet (22) sources. The ISAAC sample was selected from the catalogue of Véron-Cetty & Véron (2010, VCV), among the type 1 quasars observable from the Paranal Observatory, with declination $\delta \leq 25^\circ$, and with a redshift between 1 and 4 according to VCV (from where the first estimation of the redshift was obtained), that would allow for good coverage of the $H\beta$ and $[\text{O III}]$ region through the NIR windows with the ISAAC spectrograph at VLT. Fig. 1 shows the distri-

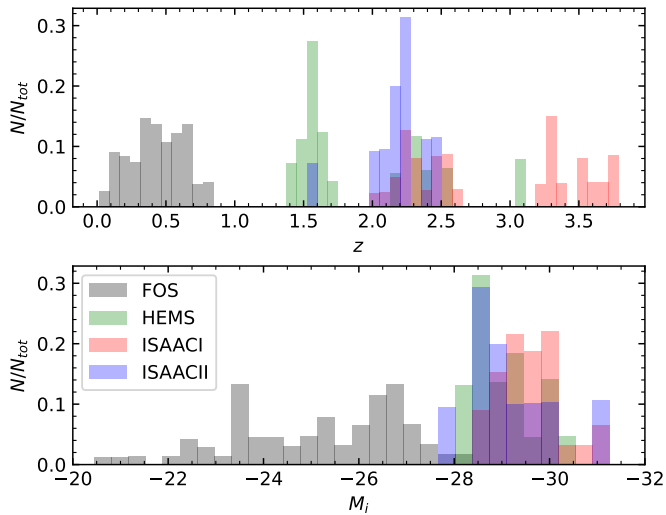


Fig. 1. Distributions of z and M_i for FOS, HEMS, ISAAC1 from Paper I, and the new ISAAC2 data. Each distribution was normalised separately.

Table 2. Log of optical observations with VLT/ISAAC.

Source	Date obs.	Band	DIT	N_{exp}	Airmass
(1)	(start)	(3)	(s)	(5)	start-end
	(2)		(4)		(6)
PKS0226-038	2011-01-27	sH	160	16	1.50-1.87
PKS0237-23	2010-11-17	sH	140	16	1.48-1.78
BZQJ0544-2241	2010-11-24	J	145	24	1.01-1.04
PKS0858-279	2010-10-13	sH	140	8	1.79-1.46
CTSJ01.03	2010-10-27	sH	180	12	1.65-1.41
WB J0948+0855	2011-01-26	sH	160	12	1.27-1.21
CTSJ03.14	2010-11-23	sH	160	12	1.34-1.18
PKS1448-232	2011-01-31	sH	160	16	2.01-1.58
[HB89]1559+088	2011-02-01	sH	170	16	2.19-1.70
FBQS J2149-0811	2010-10-26	sH	160	16	1.09-1.23

Notes. (1) Source identification. (2) Date of observation. (3) Grating used. (4) Individual Detector Integration Time (DIT). (5) Number of exposures with single exposure time equal to DIT. (6) Range of air mass of the observations.

bution in z and M_i of the complete ISAAC sample, along with the other samples considered in this work (described in §2.3). The ISAAC2 sample exhibits a very similar M_i range with the ISAAC1, despite ISAAC1 having a more extended distribution in the z context, with some cases reaching redshifts as high as ~ 3.8 .

2.3. Other samples

This work includes two additional samples, at high and low redshift (including RL and RQ sources), previously published, with UV and optical spectra available that have been analysed using the same approach for the decomposition of the emission line profiles. They consist of:

High-redshift Hamburg-ESO sample (hereafter, HEMS): The HEMS sample consist of the 28 high-luminosity and high-redshift objects with measures reported by Sulentic et al. (2017), where a detailed analysis (with the same methodology used for our ISAAC sample) of the $H\beta$ and $C\text{IV}\lambda 1549$ broad emission lines is presented. This sample was selected for having additional

UV spectra from the original 52 sources with ISAAC $H\beta$ observations of the Hamburg-ESO (HE) sample discussed in Sulentic et al. (2004, 2006) and Marziani et al. (2009). These sources are extremely luminous ($47.5 \lesssim \log L_{\text{bol}} \lesssim 48$ [erg s $^{-1}$]) and are located in a redshift range of $1.4 \lesssim z \lesssim 3.1$. The radio properties of the HEMS sample are listed in Table B.1 in Appendix B, together with the UV and optical full profile measured parameters for this sample and used in this paper. From the 28 quasars, 24 are classified as RQ while four are RL sources. We combine these data with our ISAAC1+ISAAC2 sources to build a high-luminosity sample to be analysed in the present work. As can be seen in Fig. 1, the HEMS sample shares similar i -band absolute magnitudes with the ISAAC sample.

Low-redshift FOS data: The low-luminosity sample was selected from Sulentic et al. (2007) who analyzed the $C\text{IV}\lambda 1549$ emission line parameters of 130 low-redshift sources observed with the Faint Object Spectrograph (FOS) on board HST. 84 out of these 130 quasars have optical spectra available in the recent literature and we have reanalyzed them following the same approach we have performed for the ISAAC data. We use this sample as comparison sample at low L for both optical and UV spectral ranges. Table B.1 also lists the radio properties and the UV and optical full profile parameters (velocity centroids at 1/2 and 1/4 intensity of $C\text{IV}$ and $[\text{OIII}]$) of the FOS sample. This sample includes both RQ and RL (50 and 34 sources, respectively) and has a typical bolometric luminosity of ~ 45.6 [erg s $^{-1}$] and a redshift $z \leq 0.8$, as shown in Fig. 1.

In the analysis carried out along this paper (sections §4, §5), our high- z high-luminosity sample (including RQ and RL sources) will consist of the combination of the full ISAAC (ISAAC1+ISAAC2) and HEMS samples, since both of them share similar redshift and luminosity ranges. This high- z sample consists of 60 sources in total (32 from ISAAC and 28 from HEMS), from which we have $[\text{OIII}]$ detected for 58 objects. In the case of SDSSJ005700.18+143737.7, $[\text{OIII}]$ is located very close to the edge of the spectrum, and for WB J0948+0855, the $[\text{OIII}]$ region is completely affected by absorption lines. From these 58 source, 34 are identified as blue outliers in $[\text{OIII}]$ (i.e. velocity shifts at half intensity $c(1/2)$ higher than -250 km s $^{-1}$, see §4.1), with 20 sources from ISAAC (representing $\sim 62\%$ of the sample) and 14 from HEMS ($\sim 50\%$ of the sample). Regarding $C\text{IV}$ at high- z , we have data available for 48 (20 from ISAAC and 28 from HEMS), wherein blueshifts are identified in all sources but HE2355-4621.

The low- z low-luminosity sample consists of the 84 re-analyzed FOS sources, for which we have both $[\text{OIII}]$ and $C\text{IV}$ measured data. Among them, 11 sources in $[\text{OIII}]$ and 21 in $C\text{IV}$ present a significant blueshifted component. For both emission lines, a source is classified as a blue-outlier and consequently considered to have an outflow if its full profile exhibits a velocity centroid at half peak intensity $c(1/2) < -250$ km s $^{-1}$. Also for the FOS low- z sample, when the $[\text{OIII}]$ full profile shows slightly smaller $c(1/2)$ blueshift, the object is identified with an outflow if its blueshifted component (after the spectral fitting, see section 3.3) has a significant intensity ($\geq 40\%$) relative to the full profile. The list of sources identified as outliers is reported in Table 13.

Throughout Sections 4 and 5, the sample size depends on the analysis done. For the discussions about the general behavior of the profiles or e.g. of the effect of radioloudness on the line profiles both in $C\text{IV}$ and $[\text{OIII}]$, the complete samples are considered (i.e. the 60 sources at high- z and 84 ones at low- z). However,

when addressing outflows and their dynamical parameters, only the objects identified as exhibiting blueshifted components are taking into account.

3. Observations and data analysis

3.1. NIR Observations and Data Reduction

The new spectra were taken in service mode in 2010 and 2011 under the ESO programme 086.B-0774(A), with the infrared spectrometer ISAAC, mounted at the Nasmyth A focus of VLT-U3 (Melipal) at the ESO Paranal Observatory. A summary of the observations is listed in Table 2.

Reductions were performed with an usual methodology in NIR observations using standard IRAF routines, and follow the procedures described in Paper I. Pairs of spectra were taken nodding the telescope between two positions, A and B, displaced on the CCD frame and following an ABBA cycle as it allows a better subtraction of the sky. The wavelength calibration was achieved from xenon/argon arc spectra with rms residuals of 0.4\AA in J and 0.6\AA in H. This wavelength calibration was corrected for small 0-order offsets by measuring the centroids of several OH sky lines against the arc calibration. The 2D wavelength-calibrated spectra (A and B) of each pair AB or BA were rebinned to a common linear wavelength scale. Afterwards, the sky background was subtracted using the double-subtraction technique. For each rebinned wavelength 2D spectra, we computed a frame (A-B or B-A), so that the reduced image (AB or BA) consist of two spectra of the source, one positive and one negative, positioned as separated by the nod throw and in which the sky has been removed. We then extracted the 1D wavelength-calibrated spectra using the task `apsum`, creating one spectrum for each nodding position. The one-dimensional -B (or -A) spectrum was subtracted again to obtain a final 1D A-(-B) = A+B spectrum for each observing AB and BA sequence of the ABBA cycle. Finally, all double-subtracted spectra were stacked together.

The absolute flux calibration was performed through observations, with the same setup that quasar spectra, of standard telluric stars. The standard star spectral energy distribution (SED) were retrieved from Library of Stellar Spectra for spectrophotometric calibration available at ESO². The absolute flux scale for the standard star was provided by the Two Micron All Sky Survey (2MASS, [Skrutskie et al. 2006](#)) magnitudes. Each standard star SED spectrum was then divided by its corresponding spectrum in order to correct for the atmospheric absorption features (IRAF routine `telluric`). Spectra were also corrected for galactic extinction.

As a final step, we evaluate the absolute flux calibration uncertainty on the quasar spectra by performing a comparison between the *J/H*-band magnitudes estimated by convolving the *J/H* 2MASS filter with the observed spectrum and the *J/H* magnitudes in the NASA/IPAC Extragalactic Database (NED). The average difference between 2MASS and our flux estimations is 0.026 mag, with the largest value of 0.091 ± 0.018 mag found for CTSJ01.03.

3.2. Optical data

Eight out of the ten new sources from ISAAC2 sample have available rest-frame UV spectra that cover at least one of

² https://www.eso.org/sci/observing/tools/standards/IR_spectral_library.html

Table 3. UV spectra information.

Source (1)	UV Spect. (2)
PKS0226-038	BOSS
PKS0237-23	Wilkes et al. (1983)
BZQJ0544-2241	Perlman et al. (1998)
PKS0858-279	Stickel et al. (1993)
CTSJ01.03	Tytler et al. (2004)
WB J0948+0855	BOSS
CTSJ03.14	6dFGS
PKS1448-232	...
[HB89]1559+088	SDSS
FBQS J2149-0811	...

Notes. (1) Source identification. (2) Database of reference from which the UV spectra were obtained.

the three regions of our interest (i.e. $\text{Si IV } \lambda 1397 + \text{O IV } \lambda 1402$, $\text{C IV } \lambda 1549 + \text{He II } \lambda 1402$, and the 1900\AA blend regions). In Table 3 we report the database or reference from which each UV spectrum was obtained. For four quasars (PKS0237-23, BZQJ0544-2241, PKS0858-279, and CTSJ01.03) it was necessary to digitize the spectra from the respective references reported in Table 3. This process has been performed using the `WebPlotDigitizer` facility³. The only sources for which we could not find useful UV spectra are PKS1448-232 and FBQS J2149-0811. For these two quasars, there were UV spectra available, but not with the enough S/N required to perform the fittings.

3.3. Data analysis

The spectral analysis has been carried out in two complementary ways, following the methodology described in Paper I. A multicomponent fit was performed, after the spectra were set at rest-frame, using the `specfit` ([Kriss 1994](#)) routine from IRAF package. This routine allows for simultaneous minimum- χ^2 fit of the continuum approximated by a power-law, a scalable Fe II (or Fe III) pseudo-continuum and the spectral line components yielding FWHM, peak wavelength, and intensity of all line components (see Fig. 2 of Paper I for an illustration of the decomposition analysis of the broad lines). We also include absorption lines in case some emission profiles (usually the ones of C IV) are affected by them. In addition, a study of the full broad emission line profiles has been performed, once the continuum power law, Fe II, and narrow components have been subtracted.

3.3.1. $\text{H}\beta$ spectral region

In the $\text{H}\beta$ region fittings, apart from the power-law and the scalable Fe II template, we include for the $\text{H}\beta$ BLR broad emission line: (1) a *broad component* (BC), which is symmetric and typically set at the rest-frame wavelength (Lorentzian-like shape for Pop. A and Gaussian for Pop. B); a *very broad component* (VBC), representing the innermost part of the BLR, characterised by a Gaussian shape and only present in Pop. B; (3) a *blueshifted component* (BLUE), if needed, represented by a Gaussian profile (with the option of being skewed). In addition, we include a narrow component superimposed to the broad $\text{H}\beta$

³ <https://automeris.io/>

Table 4. Measurements on the H β full broad line profile and derived properties of the H β region.

Source	$F_{5100\text{\AA}}$	F_{tot}	W [\AA]	FWHM [km s^{-1}]	A.I.	c(1/4) [km s^{-1}]	c(1/2) [km s^{-1}]	c(3/4) [km s^{-1}]	c(9/10) [km s^{-1}]	R_{FeII}	ST	$\log L_{\text{bol}}$ [erg s^{-1}]	$\log M_{\text{BH}}$ [M_{\odot}]	$\log L/L_{\text{Edd}}$
(1)	(2)	(3)	(4)	(5)	(6)	(7)	(8)	(9)	(10)	(11)	(12)	(13)	(14)	(15)
Population A														
BZQJ0544-2241	4.53	2.52	51	5191 ± 458	-0.05 ± 0.09	-266 ± 402	-174 ± 93	-94 ± 141	-57 ± 170	0.69	A2	47.52	9.66	-0.31
WB J0948+0855 ^(a)	2.88	1.27	43	5580 ± 494	0.00 ± 0.11	-1 ± 456	-1 ± 92	0 ± 149	0 ± 184	0.89	A2	47.45	9.74	-0.46
CTSJ01.03	1.96	1.73	81	4551 ± 403	0.00 ± 0.20	320 ± 372	321 ± 75	321 ± 122	321 ± 150	0.21	A1	47.37	9.52	-0.33
FBQS J2149-0811	1.73	1.80	113	4992 ± 442	0.00 ± 0.11	0 ± 408	0 ± 82	-1 ± 133	-1 ± 165	0.23	A1	47.26	9.55	-0.46
Population B														
PKS0226-038	1.48	0.99	66	5280 ± 420	0.46 ± 0.05	2874 ± 646	109 ± 53	-45 ± 140	-86 ± 190	0.62	B2	47.18	9.44	-0.44
PKS0237-23	5.19	4.48	89	7986 ± 821	0.31 ± 0.11	2546 ± 389	1374 ± 65	730 ± 211	574 ± 262	0.42	B1	47.76	9.85	-0.27
PKS0858-279 ^(a)	12.9	7.84	56	5385 ± 402	0.15 ± 0.11	790 ± 388	299 ± 61	191 ± 141	159 ± 191	0.47	B1	48.14	9.91	0.05
CTSJ03.14 ^(a)	3.44	3.61	102	4056 ± 305	0.07 ± 0.09	271 ± 274	100 ± 52	62 ± 106	50 ± 143	0.38	B1	47.62	9.36	0.08
PKS1448-232	3.43	4.53	129	4397 ± 364	0.54 ± 0.09	3664 ± 745	263 ± 47	150 ± 114	122 ± 153	0.07	B1	47.58	9.43	-0.02
[HB89]1559+088	3.31	3.66	110	5802 ± 514	0.01 ± 0.18	71 ± 750	-314 ± 115	-39 ± 157	13 ± 184	0.29	B1	47.57	9.56	-0.16

Notes. (1) Source identification. (2) Flux of the continuum on the 5100 \AA wavelength, corrected from galactic extinction, in units of $10^{-15} \text{ erg s}^{-1} \text{ cm}^{-2} \text{ \AA}^{-1}$. (3) Full H β line flux (i.e., the flux for all broad line components, BC and VBC, and BLUE whenever appropriate), in units of $10^{-13} \text{ erg s}^{-1} \text{ cm}^{-2}$. (4) H β equivalent width W . (5) FWHM. (6) Asymmetry index (A.I.). (7), (8), (9), (10) Centroid velocity shifts at $\frac{1}{4}$, $\frac{1}{2}$, $\frac{3}{4}$, and $\frac{9}{10}$ fractional intensities. (11) Ratio R_{FeII} (see §4.2). (12) Spectral types according to the quasar main sequence. (13) Bolometric luminosity. (14) Black hole mass. (15) Eddington ratio. ^(a) H β profile may be affected by the correction of the telluric absorptions present in the spectrum (see Appendix A).

Table 5. Results from `specfit` analysis on the broad and narrow profiles of H β .

Source	Full broad profile (BLUE+BC+VBC)									Full narrow profile (SBC+NC)						
	BLUE			BC			VBC			SBC				NC		
	F/F_{tot}	FWHM [km s^{-1}]	Peak [km s^{-1}]	F/F_{tot}	FWHM [km s^{-1}]	Peak [km s^{-1}]	F/F_{tot}	FWHM [km s^{-1}]	Peak [km s^{-1}]	F_{tot}	F/F_{tot}	FWHM [km s^{-1}]	Peak [km s^{-1}]	F/F_{tot}	FWHM [km s^{-1}]	Peak [km s^{-1}]
(1)	(2)	(3)	(4)	(5)	(6)	(7)	(8)	(9)	(10)	(11)	(12)	(13)	(14)	(15)	(16)	(17)
Population A																
BZQJ0544-2241	0.04	5580	-2461	0.96	4877	0	0.35	0.09	1618	-591	0.91	1187	0
WB J0948+0855	1.00	5579	0
CTSJ01.03 ^(a)	1.00	4546	321	1.00	0.18	1437	-1080	0.82	1388	0
FBQS J2149-0811 ^(b)	1.00	4992	0	0.24	0.33	1488	-1263	0.67	1258	0
Population B																
PKS0226-038	0.55	4620	-258	0.45	10495	6340	0.41	0.37	1169	-1051	0.63	901	0
PKS0237-23	0.41	5331	0	0.59	10304	3881	0.11	1.00	654::	230::
PKS0858-279	0.56	4571	6	0.44	10342	2640	6.85	0.55	1273	-1182	0.45	1168	0
CTSJ03.14	0.47	3268	0	0.53	7975	644	0.43	1.00	693	0
PKS1448-232	0.38	3615	16	0.62	14381	5824	1.31	0.61	1045	-724	0.39	1007	0
[HB89]1559+088	0.08	4702	-3110	0.33	3807	0	0.59	14817	1341	0.44	1.00	1581	-759

Notes. (1) Source identification. (2), (3), (4) Relative flux F/F_{tot} , FWHM, and velocity shift of the peak for the BLUE component. (5), (6), (7) Same for the BC. (8), (9), (10) Same for the VBC. (11) Total flux of the H β narrow profile, in units of $10^{-14} \text{ erg s}^{-1} \text{ cm}^{-2}$. (12), (13), (14) Relative flux F/F_{tot} , FWHM, and velocity shift of the peak for the SBC component. (15), (16), (17) Same for the NC. ^(a) Very difficult to separate SBC and NC (see Fig. A.5). ^(b) SBC and NC very weak and uncertain (see Fig. A.10).

that may include up to two components: the proper *narrow component* (NC), usually with $\text{FWHM} \leq 1200 \text{ km s}^{-1}$ and fitted as an unshifted Gaussian; and a *semi-broad component* (SBC), represented by a blue-shifted (symmetric or skewed) Gaussian profile with FWHM and shift similar to the [O III] semi-broad component, if present (see below for [O III] components). Final fitting for each spectrum, based on the best-fit model with the minimum χ^2 , was obtained after performing a set of models both as Pop. A and Pop. B.

Fig. 2 shows the multicomponent decomposition of the H β + [O III] spectral region for one of our sources. The fittings of the complete ISAAC2 sample are shown in Appendix A, along with their respective VLT-ISAAC optical spectra. Measurements on the H β full broad profiles of the ISAAC2 sample are listed in Table 4, where properties derived from the H β region have also been included. L_{bol} has been calculated from

the continuum flux at 5100 \AA and by applying the bolometric correction factor expected for the respective luminosity range as established by Netzer (2019). The black hole mass M_{BH} for each quasar was estimated by using the H β scaling law of Vestergaard & Peterson (2006, Eq. (5)). Eddington ratio (L/L_{Edd}) has been computed by using the bolometric luminosity and with $L_{\text{Edd}} = 1.5 \cdot 10^{38} M_{\text{BH}}$. The corresponding individual components obtained from the `specfit` decomposition of the broad H β profile are reported in Table 5.

The [O III] $\lambda\lambda 4959, 5007$ emission line profiles were modelled assuming that each line consist of a narrower centered Gaussian component (NC) and one (or more) skewed blueshifted Gaussian semi-broad component (SBC) representing bipolar outflow emissions, where the recessing side of the outflow remains obscured (see e.g., Zamanov et al. 2002; Kim et al. 2023, and references therein). Similarly to H β , the results obtained for the full

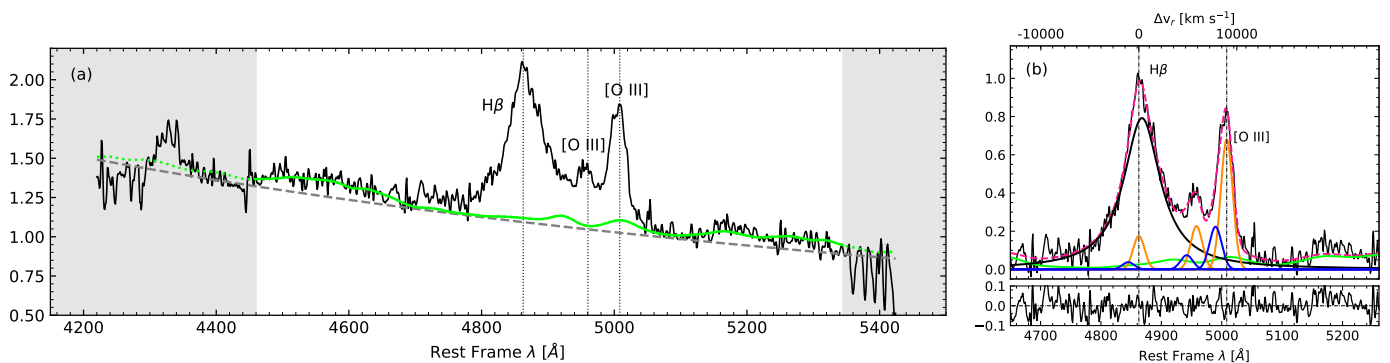


Fig. 2. (a) Rest-frame optical spectrum of CTSJ01.03. The white area shows the spectral region used in the fitting. The gray dashed line indicates the continuum level obtained with the `specfit` multicomponent fitting. Fe II contributions are represented by the green line. (b) example of the $H\beta$ + $[O\text{ III}]$ emission line decomposition (upper panel) and its respective residuals (bottom panel). Black, orange, and blue lines indicate the broad, the narrow, and the blueshifted components of the profile, respectively. The final fit is shown by the pink dashed line.

profile and the components of $[O\text{ III}]\lambda 5007$ are reported in Table 6.

3.3.2. UV spectral region

The UV spectral analysis is performed for three different regions: one centred in the $\text{Si IV}\lambda 1397$ + $\text{O IV}\lambda 1402$ lines, one in which the $\text{C IV}\lambda 1549$ dominates the emission together with a less strong $\text{He II}\lambda 1640$ line, and another region considering the emission lines from the 1900Å blend (consisting mainly of $\text{Al III}\lambda 1860$ doublet, $\text{Si III}\lambda 1892$, and $\text{C III}\lambda 1909$). In the three spectral regions, the continuum was modeled locally by a power-law and the Fe III multiplets (e.g. the strong ones observed on the red side of the 1900Å blend) were modeled using the Vestergaard & Wilkes (2001) empirical template. For some Pop. A sources, an additional Fe III $\lambda 1914$ emission line is needed to fully represent the red side of $\text{C III}\lambda 1909$ (see e.g. Martínez-Aldama et al. 2018). The broad UV lines ($\text{Si IV}\lambda 1397$, $\text{C IV}\lambda 1549$, $\text{He II}\lambda 1640$, and $\text{C III}\lambda 1909$) are fitted by the same three model components employed for $H\beta$ varying their relative contribution to each line flux, as detailed in Paper I.

Table 7 provides measurements for the $\text{C IV}\lambda 1549$ full broad profile and information on the $\text{C IV}\lambda 1549$ and $\text{He II}\lambda 1640$ individual components is given in Table 8. The FWHM and peak shift of the $\text{C IV}\lambda 1549$ and $\text{He II}\lambda 1640$ components were suitable for representing the profiles in all cases save CTSJ03.14, for which the $\text{He II}\lambda 1640$ BLUE is much narrower than the $\text{C IV}\lambda 1549$ one.

Table 9 shows the measurements on the full profile of $\text{Si IV}\lambda 1397$ and $\text{O IV}\lambda 1402$. Similar to the approach taken in Paper I, we also set the $\text{Si IV}\lambda 1397$ BC at rest-frame and select as initial guess a FWHM similar to the one determined for $\text{C IV}\lambda 1549$ BC.

The measurements resulting from the `specfit` analysis of the 1900Å blend are presented in Table 10. As $\text{Si III}\lambda 1892$ has the same peak rest-frame velocity and FWHM of $\text{Al III}\lambda 1860$, we do not report these values for the Si III line in the table.

3.4. Radio data

The radio properties for the complete ISAAC sample are reported in Table 11. The radio fluxes used for estimate these parameters were obtained from the 1.4-GHz NRAO VLA Sky Survey (NVSS, Condon et al. 1998) and from the VLA Faint Images of the Radio Sky at Twenty-Centimeters survey (FIRST,

Gregg et al. 1996; Becker et al. 1995) catalogues. In the case of CTQ 0408, not covered by these two surveys, the upper limit for the flux has been estimated from the SUMSS catalogue (Mauch et al. 2003). The R_K parameter is determined as the ratio between the rest-frame specific fluxes at 1.4 GHz and at the g -band effective wavelength (following Ganci et al. 2019). We then consider three different ranges of radio-loudness: radio-quiet (RQ; $R_K < 10$), radio-intermediate (RI; $10 \leq R_K \leq 70$), and radio-loud (RL; $R_K \geq 70$).

If the object is not detected (for the 50% of the sample: 16 sources, 15 from ISAAC1, and one from ISAAC2), an upper limit on the radio flux is set equal to a detection threshold (~ 2 times the rms, in both FIRST and NVSS catalogs) at the position of the source. Our preference is to rely on the FIRST detection limit as its maps have a higher sensitivity than NVSS and allows for a better restrictive upper limit. However, in cases where the object's position does not fall within the current coverage of the FIRST catalog, we then utilize the NVSS detection limit. When considering the complete ISAAC sample, we have 10 RL, two RI, and 20 RQ sources.

For objects from both HEMS and FOS sample, we re-estimated the values of R_K using the same methodology employed for the ISAAC data. In the HEMS sample, from the 28 sources four are RL and 24 RQ. As mentioned in section 2.3, in the low luminosity FOS sample there are 34 RL and 50 RQ.

By default, we have defined that the sources initially classified as radio-intermediate are considered together as radio-quiet objects unless we have evidences that the source is jetted. The origin of enhancement of radio emission in RIs is possibly related to star formation (Condon et al. 2013; Bonzini et al. 2015; Caccianiga et al. 2015; Ganci et al. 2019), powerful broad line region and extended ionized outflows (Panessa et al. 2019, and references therein), or to intrinsic reddening in the optical fluxes.

4. Results

4.1. ISAAC1 and ISAAC2 basic results: a synopsis

The optical and UV main spectral properties of ISAAC1 and ISAAC2 are fully consistent.

$H\beta$ – The dichotomy between Pop. A and Pop. B is preserved in the complete ISAAC sample, with Pop. A quasars usually presenting lower values of $H\beta$ W and FWHM. However, it is noteworthy that the lowest FWHM($H\beta$) values in ISAAC2 are observed in two Pop. B quasars (CTSJ03.14 and PKS1448-232),

Table 6. Measurements on the [O III] λ 5007 line profile.

Source	F_{tot}	W [Å]	[O III] λ 5007 full profile				SBC			NC		
			FWHM [km s $^{-1}$]	A.I.	$c(1/2)$ [km s $^{-1}$]	$c(9/10)$ [km s $^{-1}$]	F/F_{tot}	FWHM [km s $^{-1}$]	Peak [km s $^{-1}$]	F/F_{tot}	FWHM [km s $^{-1}$]	Peak [km s $^{-1}$]
(1)	(2)	(3)	(4)	(5)	(6)	(7)	(8)	(9)	(10)	(11)	(12)	(13)
Population A												
BZQJ0544-2241 ^(a)	0.27	6	1374 \pm 360	-0.07 \pm 0.04	-369 \pm 40	-339 \pm 88	0.45	1618	-621	0.55	1187	-247
CTSJ01.03	0.44	22	1709 \pm 123	-0.18 \pm 0.02	-191 \pm 33	-88 \pm 553	0.25	1437	-1110	0.75	1388	0
FBQS J2149-0811 ^(a)	0.14	9	1477 \pm 440	-0.20 \pm 0.10	-319 \pm 58	-248 \pm 92	0.25	1488	-1292	0.75	1258	-187
Population B												
PKS0226-038	0.31	22	979 \pm 69	-0.27 \pm 0.16	-46 \pm 16	-18 \pm 31	0.24	1169	-1080	0.76	901	0
PKS0237-23	0.31	6	1602 \pm 109	0.09 \pm 0.01	-805 \pm 21	-922 \pm 42	0.83	1423	-899	0.17	654	-34
PKS0858-279	0.33	3	1506 \pm 234	-0.35 \pm 0.02	-114 \pm 80	27 \pm 42	0.31	1273	-1211	0.69	1168	65
CTSJ03.14	1.34	40	860 \pm 92	-0.29 \pm 0.13	-120 \pm 40	-38 \pm 21	0.27	1774	-504	0.73	693	-38
PKS1448-232	0.36	11	1154 \pm 74	-0.08 \pm 0.02	-271 \pm 17	-240 \pm 36	0.24	1045	-754	0.76	1007	-161
[HB89]1559+088	0.31	10	885 \pm 215	-0.51 \pm 0.03	-605 \pm 69	-538 \pm 52	0.54	1581	-1452	0.46	688	-498

Notes. (1) Source identification. (2) [O III] λ 5007 total flux, in units of 10^{-13} erg s $^{-1}$ cm $^{-2}$. (3) Equivalent width, W. (4), (5), (6), (7) FWHM, asymmetry index, and the centroid velocities at $\frac{1}{2}$ and $\frac{9}{10}$ intensities of the full profile. (8), (9), (10) Relative intensity, FWHM, and peak shift for the [O III] semi-broad (in general blueshifted) component. (11), (12), (13) Same for the [O III] narrow component. ^(a) [O III] λ 5007 may be affected by the correction of the telluric absorptions present in the spectrum (see Appendix A).

Table 7. Measurements on the C IV λ 1549 full broad profile.

Source	W [Å]	FWHM [km s $^{-1}$]	A.I.	$c(1/4)$ [km s $^{-1}$]	$c(1/2)$ [km s $^{-1}$]	$c(3/4)$ [km s $^{-1}$]	$c(9/10)$ [km s $^{-1}$]
(1)	(2)	(3)	(4)	(5)	(6)	(7)	(8)
Population A							
WB J0948+0855	4.99 \pm 0.21	10363 \pm 984	-0.52 \pm 0.03	-6901 \pm 642	-5334 \pm 354	-3008 \pm 366	-2207 \pm 235
CTSJ01.03	19.35 \pm 0.82	4381 \pm 367	-0.38 \pm 0.06	-2250 \pm 421	-1660 \pm 120	-1100 \pm 126	-762 \pm 147
Population B							
PKS0226-038	32.03 \pm 1.36	4898 \pm 508	-0.31 \pm 0.06	-1878 \pm 397	-1148 \pm 153	-665 \pm 139	-474 \pm 141
PKS0237-23	25.47 \pm 1.08	7269 \pm 729	-0.01 \pm 0.06	-1281 \pm 646	-1461 \pm 168	-1213 \pm 217	-1199 \pm 179
CTSJ03.14	30.04 \pm 1.27	4087 \pm 385	-0.30 \pm 0.05	-1632 \pm 369	-650 \pm 105	-481 \pm 113	-471 \pm 113
[HB89]1559+088	27.87 \pm 1.18	4922 \pm 527	-0.06 \pm 0.05	-1492 \pm 340	-1601 \pm 94	-1420 \pm 144	-1241 \pm 145

Notes. (1) Source identification. (2) Equivalent width. (3) FWHM. (4) Asymmetry index. (5), (6), (7) and (8) Velocity centroids at different fractional intensities in km s $^{-1}$.

both of which are blazar candidates and therefore the FWHM may be strongly influenced by the source orientation. Among the ISAAC2 H β Pop. A profiles, all are symmetric except for BZQJ0544-2241, which requires an additional (usually weak) BLUE component to fully represent the H β line. In contrast, the H β profiles in Pop. B sources are all redward asymmetric with the exception of [HB89]1559+088, which is nearly symmetric and also requires a BLUE component. This additional component is added when the blueshift observed in the H β profile does not correspond to the blueshifted SBC observed in [O III] λ 5007. The full ISAAC sample has eight quasars (five Pop. A and three Pop. B) with a BLUE component, which contribution to the profile has an average value of \approx 8%. The mean asymmetry index for the whole ISAAC sample Pop. B is 0.26 (same for only ISAAC2) and they have the full broad profile with an averaged velocity centroid $c(1/4)$ of 1740 km s $^{-1}$. This is attributed to the fact that in Pop. B the most prominent broad component is the VBC, which accounts for 54% of the H β profile in the ISAAC2 sample (57% for the whole ISAAC), with median FWHM and shift values of \approx 10420 and 3149 km s $^{-1}$, respectively. Consistent values are found for the full ISAAC sample, with median values of the FWHM and shift of the VBC of 11760 and 3000 km s $^{-1}$, respectively, in good agreement with the values obtained

in HEMS sources (e.g., Marziani et al. 2009; Sulentic et al. 2017, see also Vietri et al. 2018, 2020; Wolf et al. 2020 for extremely broad H β profiles).

[O III] λ 4959,5007 – In the full ISAAC sample, both populations (A & B) exhibit significant blue shifts, with the most pronounced ones observed in Pop. A sources. In most of the full ISAAC sample both the [O III] SBC and NC are often not in the rest-frame. Additionally, for 18 out of the 32 sources from the whole ISAAC sample (16 from ISAAC1 and two from ISAAC2), the SBC is the strongest component, accounting for \sim 64% of the flux in the case of Pop. A and \sim 52% for Pop. B. Consequently, the two populations A and B also differ in terms of FWHM, with the Pop. A on average showing slightly broader profiles due to the presence of a stronger SBC. Moreover, in contrast to the low- z scenario where the majority of the [O III] λ 5007 profiles exhibit blueshift velocity centroids at half intensity, $c(1/2)$, lower than 250 km s $^{-1}$ (Zamanov et al. 2002; Marziani et al. 2016a), in our complete high- z ISAAC sample the 62% of the sources have blueshifts in [O III] greater than 250 km s $^{-1}$ and are considered outliers. However, in ISAAC2, we do not observe the few very large [O III] profiles (FWHM \sim 4000 km s $^{-1}$) mea-

Table 8. Results from `specfit` analysis on C iv λ 1549 and He II λ 1640.

Source	C iv λ 1549									He II λ 1640										
	C iv λ 1549 BLUE				C iv λ 1549 BC			C iv λ 1549 VBC			He II λ 1640 BLUE				He II λ 1640 BC			He II λ 1640 VBC		
	F_{tot}	F/F_{tot}	FWHM [km s $^{-1}$]	Peak [km s $^{-1}$]	F/F_{tot}	FWHM [km s $^{-1}$]	F/F_{tot}	FWHM [km s $^{-1}$]	Peak [km s $^{-1}$]	F_{tot}	F/F_{tot}	FWHM [km s $^{-1}$]	Peak [km s $^{-1}$]	F/F_{tot}	FWHM [km s $^{-1}$]	F/F_{tot}	FWHM [km s $^{-1}$]	Peak [km s $^{-1}$]		
(1)	(2)	(3)	(4)	(5)	(6)	(7)	(8)	(9)	(10)	(11)	(12)	(13)	(14)	(15)	(16)	(17)	(18)	(19)		
Population A																				
WB J0948+0855	0.75	0.82	22060	-2129	0.25	5558	0.15	0.72	22060	-2129	0.28	5558		
CTSJ01.03	11.87	0.68	9263	-530	0.32	4562	1.82	0.62	9263	-530	0.38	4562		
Population B																				
PKS0226-038	3.43	0.52	10535	-590	0.21	3525	0.28	10908	1842	0.77	0.58	10535	-3180	0.22	3535	0.20	10908	1842		
PKS0237-23	16.85	0.44	10778	-1970	0.20	4209	0.36	10503	2624	3.08	0.40	10778	-1970	0.20	4209	0.40	10503	2624		
CTSJ03.14	5.89	0.48	10299	-1103	0.40	3274	0.13	10500	2035	0.78	0.33	5500	-1025	0.07	3274	0.61	10500	2035		
[HB89]1559+088	4.89	0.46	7129	-1394	0.25	4226	0.29	12931	2035	0.66	0.34	7129	-1394	0.13	4226	0.53	12931	2035		

Notes. (1) Source identification. (2) C iv λ 1549 total flux, in units of 10^{-13} erg s $^{-1}$ cm $^{-2}$. (3), (4), (5) Relative intensity, FWHM, and peak shift for the C iv λ 1549 BLUE component. (6), (7) Relative intensity and FWHM of the C iv λ 1549 BC, which is centered in the respective rest-frame. (8), (9), (10) Relative intensity, FWHM, and peak shift of the C iv λ 1549 VBC. Columns (11)–(19) show the same, but for He II λ 1640.

Table 9. Measurements on the Si iv λ 1397+O iv] λ 1402 broad lines.

Source	$F_{\text{tot}}^{(a)}$	FWHM [km s $^{-1}$]	A.I.	$c(1/2)$ [km s $^{-1}$]	$c(9/10)$ [km s $^{-1}$]
(1)	(2)	(3)	(4)	(5)	(6)
Population A					
WB J0948+0855	0.92	9878 \pm 1013	0.07 \pm 0.03	-2257 \pm 192	-2633 \pm 411
Population B					
PKS0226-038	1.24	6387 \pm 1005	-0.09 \pm 0.12	465 \pm 228	756 \pm 415
PKS0237-23	2.42	5084 \pm 666	0.06 \pm 0.03	965 \pm 119	881 \pm 323
[HB89]1559+088	1.96	7661 \pm 1114	0.00 \pm 0.06	-566 \pm 284	-752 \pm 474

Notes. (1) Source identification. (2) Total flux, in units of 10^{-13} erg s $^{-1}$ cm $^{-2}$. (3) FWHM. (4) Asymmetry index. (5) and (6) Velocity centroids at $\frac{1}{2}$ and $\frac{9}{10}$ fractional intensities.

sured in ISAAC1. This may be a consequence of the fact that ISAAC1 is primarily composed of radio-quiet sources (which typically exhibit broader [O III] λ 4959,5007 profiles than radio-loud ones, see §4.5.2), while a significant fraction of ISAAC2 is classified as radio-loud. Significant [O III] outflows appear to be a common feature at high redshift and have also been observed in other samples (see e.g., Kakkad et al. 2020). As discussed in Paper I, the [O III] profile almost always appear peculiar if compared to the ones of optically selected samples at low redshift (Zamanov et al. 2002; Marziani et al. 2003b; Bian et al. 2005; Zhang et al. 2011; Cracco et al. 2016), with higher shift amplitude and broader widths.

C iv λ 1549 – Consistent results with ISAAC1 are also observed for ISAAC2 C iv λ 1549 profiles. In general, the Pop. B sources from ISAAC2 tend to exhibit slightly larger values of W than Pop. A. This is also observed in the full ISAAC sample (median $W \sim 27$ Å for Pop. B vs. ~ 21 Å for Pop. A). Conversely, Pop. A sources tend to show greater FWHM, asymmetry, and centroid velocities, which is in agreement with the HEMS sample (Sulentic et al. 2017). The BLUE is the strongest component in the full ISAAC sample, and contributes to $\sim 72\%$ and $\sim 51\%$ of the full C iv λ 1549 flux for Pop. A and Pop. B, respectively. Consistently, the largest blueshifts are found for the BLUE components of Pop. A sources, which achieve a median value of $c(1/2)$ of the full C iv λ 1549 profile $\sim -2590 \pm 1890$ km s $^{-1}$ for the entire

ISAAC sample. In the case of Pop. B, this value is $\sim -1530 \pm 760$ km s $^{-1}$. Centroid shifts are comparable to the ones derived in recent works that followed a similar analysis strategy (Coatman et al. 2016; Vietri et al. 2018; Temple et al. 2023, and especially Sulentic et al. (2017) which analyses the HEMS sample). Both [O III] λ 4959,5007 and C iv λ 1549 suggest the presence of extremely powerful winds in the NLR and BLR (Marziani et al. 2016c,b; Fiore et al. 2017; Bischetti et al. 2017). At variance with low- z , low-luminosity sources, the blueshifted emission associated with the winds are prominent in both Pop. A and B, as further discussed in §5.1 and §5.2.

1900Å blend – In ISAAC2 sample we have 1900Å blend data for six of the 10 objects (two Pop. A and four Pop. B). The 1900Å blend properties observed in the ISAAC2 sample also appear consistent with the full ISAAC sample, as well as with the expectations from recent works involving intermediate redshift sources (Temple et al. 2020; Marziani et al. 2022a; Buendia-Rios et al. 2022). Considering the whole ISAAC sample (11 Pop. A and nine Pop. B quasars), we find that the BLUE component in Al III λ 1860 is detected in only five Pop. A with an average blueshift of ~ -1720 km s $^{-1}$ and account for $\sim 40\%$ of the full profile. For Pop. B, all nine sources show Al III λ 1860 profiles well-represented by a single rest-frame BC with averaged FWHM ~ 4240 km s $^{-1}$. For Si III] λ 1892, only three Pop. A exhibit a BLUE component, with an averaged shift of ~ -1880 km s $^{-1}$. Regarding the C III] λ 1909 profiles, Pop. A sources are suitably represented by a rest-frame BC with FWHM ~ 3370 km s $^{-1}$. Nine out of the 11 Pop. A sources needed an additional Fe III component at ~ 1914 Å. The Pop. B C III] λ 1909 profiles are fitted by the combination BC+VBC, where the VBC is weaker than that of H β , as it represents only 37% of the full profile with FWHM of ~ 7240 km s $^{-1}$.

4.2. The optical plane of the 4DE1 parameter space

The classification as A/B population in the quasar MS is based on two parameters that can be measured only on the NIR spectra: the FWHM of H β full broad profile and the strength of the Fe II blend at 4570Å, defined as the ratio between the intensities of the blue blend of Fe II at 4750Å and H β , $R_{\text{Fe II}}$. The Pop. A/Pop. B limit was set according to the luminosity-dependent FWHM value, as explained in Paper I. We measured the parameter $R_{\text{Fe II}}$

Table 10. Results from `specfit` analysis on the 1900Å blend.

Source (1)	Al III λ 1860					Si III λ 1892				C III] λ 1909+Fe III λ 1914											
	Al III λ 1860 BLUE					Al III λ 1860 BC ^(b)				C III] λ 1909 BC ^(b)		C III] λ 1909 VBC			C III] λ 1909 NC ^(b)		Fe III λ 1914				
	F_{tot}	W [Å]	F/F_{tot}	FWHM [km s ⁻¹]	Peak [km s ⁻¹]	F/F_{tot}	FWHM [km s ⁻¹]	F_{tot}	W [Å]	F_{tot}	W [Å]	F/F_{tot}	FWHM [km s ⁻¹]	F/F_{tot}	FWHM [km s ⁻¹]	Peak [km s ⁻¹]	F/F_{tot}	FWHM [km s ⁻¹]	F_{tot}	FWHM [km s ⁻¹]	Peak [km s ⁻¹]
Population A																					
BZQJ0544-2241	12.61	5.44	1.00	5559	9.17	4.03	1.23	5.46	1.00	5382	9.17	5105	3169
WB J0948+0855	8.55	5.31	0.33	3184	-2011	0.67	5549	5.57	4.38	1.28	1.19	1.00	5549	1.46	5177	1618
Population B																					
PKS0226-038	3.38	3.52	1.00	4722	5.26	5.60	0.87	9.97	0.65	4722	0.35	7018	2467	0.06	999
PKS0858-279	32.88	2.96	1.00	4973	44.3	4.05	7.75	7.15	0.66	4973	0.34	8588	4908
CTSJ03.14	2.12	1.64	1.00	3044	2.97	2.46	1.10	9.78	0.83	3044	0.17	6954	2948	0.03	970
[HB89]1559+088	3.42	2.55	1.00	4226	9.15	7.02	0.96	7.65	0.42	4226	0.58	7338	2207	0.01	999

Notes. (1) Source identification. (2) Al III λ 1860 total flux, in units of 10^{-14} erg s⁻¹ cm⁻². (3) Al III λ 1860 Equivalent width W . (4), (5) and (6) Relative intensity, FWHM, and peak shift respectively for the Al III λ 1860 BLUE component. (7) and (8) Relative intensity and FWHM for the Al III λ 1860 BC, centered in the respective rest-frame. (9) and (10) Si III λ 1892 total flux (in units of 10^{-14} erg s⁻¹ cm⁻²) and W . (11), (12) Same for C III] λ 1909. (13) and (14) Relative intensity and FWHM for C III] λ 1909 BC, centered in the respective rest-frame. (15), (16) and (17) Relative intensity, FWHM, and peak shift for the C III] λ 1909 VBC. (18) and (19) Relative intensity and FWHM for the C III] λ 1909 NC, centered in the respective rest-frame. (20), (21) and (22) Fe III λ 1914 total flux (in units of 10^{-14} erg s⁻¹ cm⁻²), FWHM and peak shift.

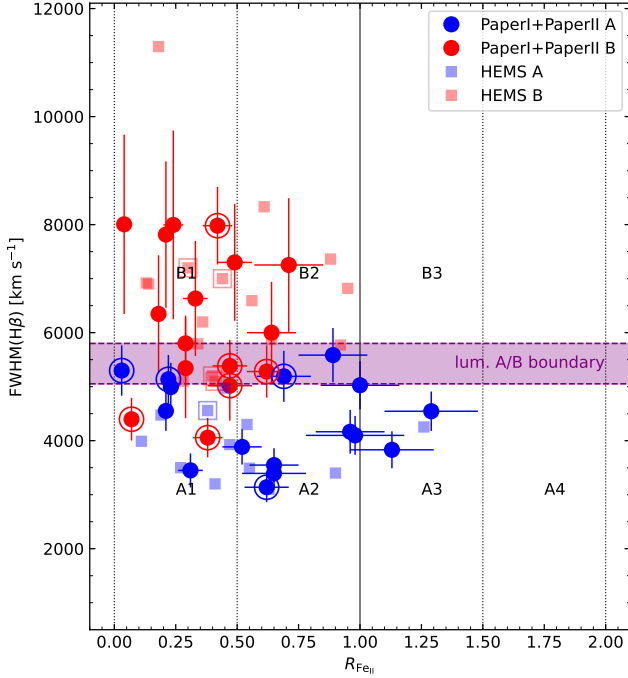


Fig. 3. Location on the MS of the 10 new sources for this work together with the ones from Paper I (circles) and the HEMS sample (squares). Pop. A quasars are represented by blue symbols and Pop. B by red symbols. The radio-loud sources are surrounded by an open circle/square in the plot. Grey region indicates the distribution of the main sequence of quasars at low- z . Purple-shaded area shows the luminosity-dependent boundary between Pops. A and B for high luminosity sources, as described in detail in Paper I.

parameter to assign a number from 1 to 4 to the Spectral Type (ST) covering the range $0 \leq R_{\text{FeII}} \leq 2$ with a step $\Delta R_{\text{FeII}} = 0.5$ (Sulentic et al. 2002).

The location of the whole ISAAC sample in the MS optical plane is shown in Fig. 3, where are also represented the 28 sources belonging to the HEMS sample. As discussed in Paper I, the sources of high luminosity, such as the 10 new quasars presented here, show a displacement in the direction of increasing $\text{FWHM}(\text{H}\beta)$ by $1000 - 1500$ km s⁻¹ respect to the low-

luminosity, low- z samples (see also Sulentic et al. 2017). Of the 10 new sources, six are classified as Pop. B and four as Pop. A. CTSJ03.14 and PKS1448-232 (see the models in Figs. A.7 and A.8, respectively), two RLs classified as B1, are located below the Pop A/B boundary for their luminosity. Both sources are blazar candidates (see Massaro et al. (2014) for CTSJ03.14 and Massaro et al. (2015) for PKS1448-232), implying that the FWHM of H β may be significantly lowered by a pole-on orientation of the line-emitting region. In the complete sample considered in this work (ISAAC1+ISAAC2+HEMS), there are 30 sources classified as Pop. A (including five RL) and 30 classified as Pop. B (with eight of them being RL).

4.3. The role of physical parameters

In Paper I, we show that while the bolometric luminosity, L_{bol} , and the black hole mass (M_{BH}) exhibit trends with the C IV blueshifts, the primary correlation is observed with the Eddington ratio, with the higher C IV blueshift in the higher accretion rate (see e.g. §6.3 of Paper I, and references therein). These results are reconfirmed in the present work. By including the new data from ISAAC2 in the sample composed by both the high- and low- z data, we find a relation between C IV $c(1/4)$ blueshift (< -250 km s⁻¹) and L_{bol} with a slope of 0.21 ± 0.07 (with a Pearson correlation coefficient c.c. of 0.61, $\rho \sim 10^{-9}$). The slope 0.14 ± 0.06 , and Pearson c.c. ~ 0.48 ($\rho \sim 10^{-6}$) suggest an even weaker relation between C IV $c(1/4)$ and the black hole mass M_{BH} . Regarding the Eddington ratio, we find the following relation (with a Pearson c.c. ~ 0.66 and a ρ -value for the null hypothesis $\sim 10^{-11}$):

$$\log |c(1/4)_{\text{CIV}}| = (0.43 \pm 0.05) \log L/L_{\text{Edd}} + (3.39 \pm 0.04).$$

Similar results, albeit less significant, are observed for [O III]. When analyzing the 45 sources (34 high- z and 11 low- z) that exhibit significant [O III] outflows, we find a slope of 0.12 ± 0.07 between [O III] $c(1/4)$ and L_{bol} (Pearson c.c. ~ 0.31 , $\rho \sim 10^{-2}$). Concerning L/L_{Edd} , we obtain (Pearson c.c. ~ 0.48 , $\rho \sim 10^{-4}$):

$$\log |c(1/4)_{[\text{OIII}]}| = (0.33 \pm 0.09) \log L/L_{\text{Edd}} + (2.91 \pm 0.04).$$

In tight agreement with these relations, Fig. 4 shows the dependence of $c(1/4)$ on L/L_{Edd} for the [O III] λ 5007 and C IV λ 1549

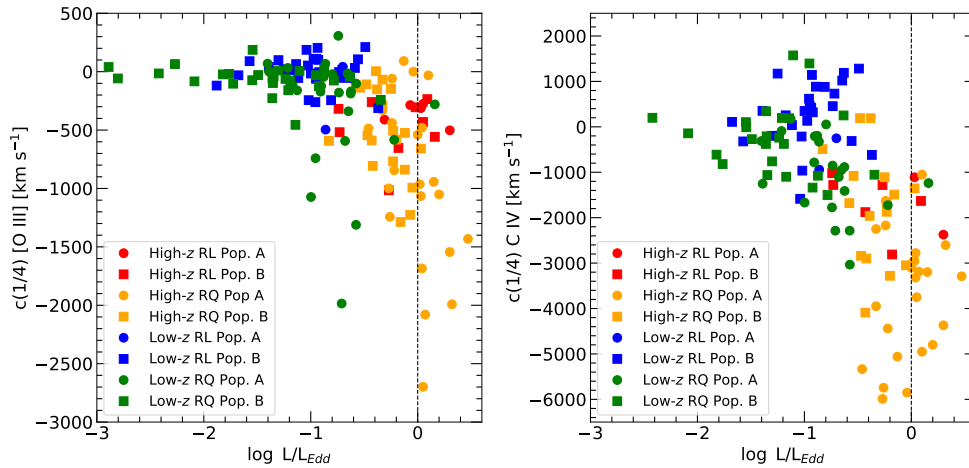


Fig. 4. Velocity centroid $c(1/4)$ versus L/L_{Edd} for $[\text{O III}]\lambda 5007$ (left) and $\text{C IV}\lambda 1549$ (right). Dark green and blue symbols correspond respectively to RQ and RL sources at low- z , while orange (RQ) and red (RL) symbols to high- z quasars. Within each colour, filled squares represent Pop. B sources and the bullets Pop. A quasars.

emission lines, where we have included all the measures of $c(1/4)$ velocity centroids of both lines (blue-shifted or not) and for both low- and high- z samples. For the two emission lines, strong outflows (i.e., $\geq 500 \text{ km s}^{-1}$ for $[\text{O III}]\lambda 5007$ and $\geq 2000 \text{ km s}^{-1}$ for $\text{C IV}\lambda 1549$) are found at Eddington ratios $\log L/L_{\text{Edd}} \geq -0.8$ ($L/L_{\text{Edd}} \sim 0.2$), consistent with previous results (see e.g. Marziani et al. 2003b; Bian et al. 2005; Komossa et al. 2008; Marziani et al. 2016c; Cracco et al. 2016; Coatman et al. 2016; Wang et al. 2018; Ayubinia et al. 2023).

The effect of high Eddington ratio is strengthened at high luminosity. The high- z – low- z comparison is consistent with the weaker luminosity effect (outflow velocity $\propto L^{1/4}$) on both the RL and RQ samples that is expected for radiation driven winds and that becomes appreciable if samples spread over a wide range of luminosity are considered (Laor & Brandt 2002, c.f. Sulentic et al. 2017).

The radioloudness appears to play a role in reducing the outflow velocities in both $[\text{O III}]\lambda 5007$ and $\text{C IV}\lambda 1549$. The sources that present the most significant blueshifts in both $[\text{O III}]\lambda 5007$ and $\text{C IV}\lambda 1549$ are all radio-quiet. Conversely, the radio-loud sources (blue and red symbols) exhibit smaller outflow velocities. This result is in a good agreement with previous findings (e.g., Marziani et al. 2003b; Laor 2018) and is discussed in more details in §4.4 and 4.5.

4.4. Inter-comparison between RL and RQ at low and high z : $[\text{O III}]\lambda 5007$ vs. $\text{C IV}\lambda 1549$

Fig. 5 presents a comparison between $[\text{O III}]\lambda 5007$ and $\text{C IV}\lambda 1549$ in terms of the relative intensity of the outflowing component (SBC for $[\text{O III}]\lambda 5007$ and BLUE for $\text{C IV}\lambda 1549$) with respect to the full profiles, $I_{\text{SBC}}/I_{\text{tot}}$. In this case, we exclusively consider sources that are identified as blue-outliers in $[\text{O III}]\lambda 5007$ and which also present blueshifts in $\text{C IV}\lambda 1549$. Therefore, the sample shown in Fig. 5 has 28 high- z sources (14 from ISAAC and 14 from HEMS) and 9 low- z FOS sample. In addition, in the FOS sample there are seven objects in which only a blueshifted SBC $[\text{O III}]\lambda 5007$ component (with no clear NC) is detected, which nevertheless present shifts in the $c(1/2)$ lower than -250 . Clearly identifying any outflow in these cases would require higher resolution and an improved S/N than the data available in the present work.

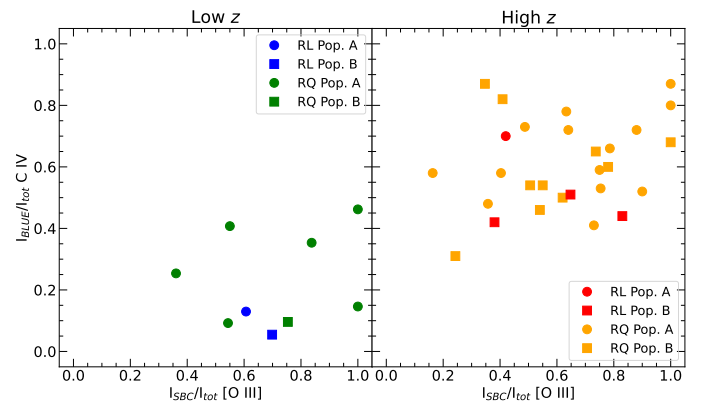


Fig. 5. Comparison between the relative intensities of the blueshifted component for both $[\text{O III}]\lambda 5007$ and $\text{C IV}\lambda 1549$. Low redshift (z) sources represented in the left panel and high z in the right one.

At low redshift, the behaviour of the BLUE component appears to be different in $[\text{O III}]\lambda 5007$ and $\text{C IV}\lambda 1549$ in terms of relative intensity: while the $[\text{O III}]\lambda 5007$ outflowing component can achieve a $I_{\text{SBC}}/I_{\text{tot}}$ up to a nearly $\sim 100\%$ of the total intensity of the full profile, the $\text{C IV}\lambda 1549$ outflowing component never surpasses $\sim 40\%$ of the entire profile, with the lower values found for the RL sources

The right panel of Fig. 5 shows the same analysis but for the high-redshift range. At variance with the low- z sample, both the $[\text{O III}]\lambda 5007$ and $\text{C IV}\lambda 1549$ emission lines exhibit very similar behaviour with respect to their outflowing component, and their ratio $I_{\text{BLUE}}/I_{\text{tot}}$ can vary from $\sim 20\%$ to 100% of the full profile, with the largest contributions found in radio-quiet sources. The radio-loud/radio-quiet difference at high redshift is consistent with the one found at low redshift, with the RL sources presenting clearly fainter $[\text{O III}]\lambda 5007$ SBC and $\text{C IV}\lambda 1549$ BLUE.

We have analyzed the RL and RQ blueshift distributions in an attempt to characterize other parameters affected by radioloudness. Fig. 6 shows the cumulative distribution functions of centroid velocities at 1/4 flux intensity ($c(1/4)$) of both $[\text{O III}]\lambda 5007$ and $\text{C IV}\lambda 1549$ emission lines for the samples by separating them according to the radio classification and the redshift range. All sources with $[\text{O III}]\lambda 5007$ or $\text{C IV}\lambda 1549$ spectral information have been taken into account regardless of the shift. The panel (a) shows a comparison between RL and RQ at low redshift for

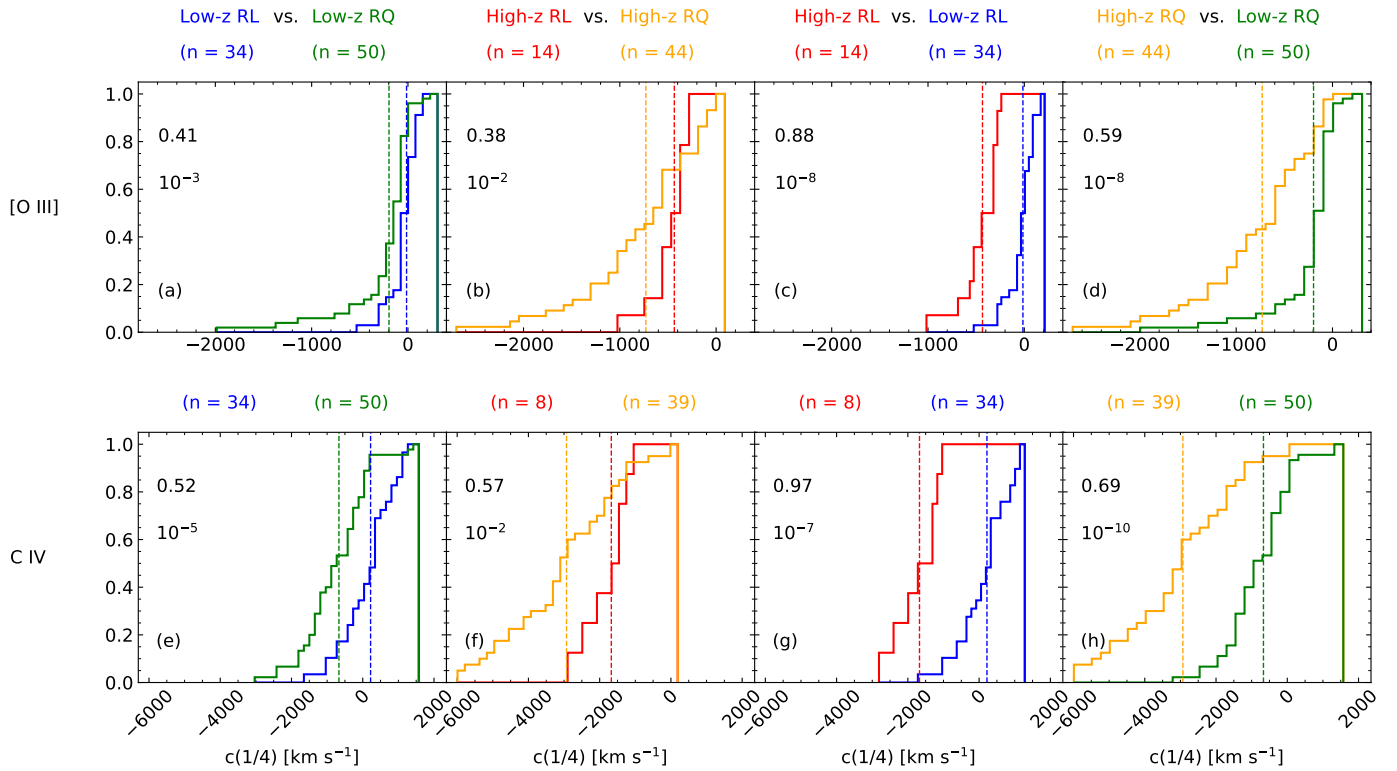


Fig. 6. Centroid velocities at 1/4 intensities ($c(1/4)$) cumulative distributions of the samples separated by radioloudness and redshift ranges for $[O\text{ III}]\lambda 5007$ (top panels) and $C\text{ IV}\lambda 1549$ (bottom panels). Kolmogorov-Smirnov (KS) tests were performed comparing different subsamples identified at the top of the panels. KS statistics for each comparison are shown on the top left of each plot together with the respective ρ -value. Vertical lines indicate the mean value for each subsample.

the $[O\text{ III}]\lambda 5007$ $c(1/4)$. In this case, the Kolmogorov-Smirnov (KS) test reveals that the RL and RQ subsamples are statistically indistinguishable, although the RQ in general present larger values of $c(1/4)$ towards the blue, which indicates stronger outflows than for RL sources. A similar result is found when comparing RL and RQ $c(1/4)$ at high- z (panel (b) of Fig. 6).

Panel (c) of Fig. 6 compares the RL sources at high- and low- z ranges. The KS test indicates that the distributions are significantly different (~ 0.88 , $\rho \sim 10^{-8}$), with the RL sources at high redshift presenting larger outflows velocities (mean value ~ -420 km s^{-1}) than the ones at lower redshifts (~ -40 km s^{-1}). The same is found when comparing RQ sources at high and low redshift (panel (d)). The difference in this case is still significant due to more prominent outflow at high z , with $c(1/4)$ mean values ≈ -740 and ≈ -200 km s^{-1} for high and low z , respectively.

The bottom panels of Fig. 6 show the results for the $C\text{ IV}\lambda 1549$ emission line. In general, the $c(1/4)$ of this line follows the same behaviour of $[O\text{ III}]\lambda 5007$ albeit with stronger outflows. In both RQs and RLs there is a statistically very significant difference between the distributions of $C\text{ IV}$ $c(1/4)$ at high and low redshift. The more extreme difference is found between RL sources at high and low z , where the distributions are completely different (KS coefficient of 0.97, and a probability of coming from the same distribution $\rho \sim 10^{-7}$). The significance is extremely high, even if the RL subsample in the case of $C\text{ IV}\lambda 1549$ at high z counts with only seven sources.

The cumulative distributions of both $[O\text{ III}]\lambda 5007$ and $C\text{ IV}\lambda 1549$ centroid shifts demonstrate that the main difference between samples is when they widely differ in luminosity, not radioloudness. In the two redshift domains considered (corresponding on average to a difference in luminosity of a factor ≈ 60), Fig. 4 and Fig. 6 show

that there is second order effect related to radioloudness, in both $C\text{ IV}\lambda 1549$ and $[O\text{ III}]\lambda 4959,5007$. The effect is more significant at low- z (with a $\rho \sim 10^{-5}$), although a similar difference in shift amplitudes is detected also at high-redshift. In the latter case, the small number of sources makes the effect not statistically significant. Summing up, the effect of radioloudness is consistent in the low- z and high- z samples, with lower blueshifted velocities and outflows in the RLs, albeit weaker than the one due to luminosity and the accretion rate (see section 4.3).

4.5. Trends with radio loudness

4.5.1. Fe II

The relation between the $R_{\text{Fe II}}$ with the radioloudness parameter R_{K} is shown in Fig. 7. In both low- and high- z ranges, the RQ sources are the ones that can present $R_{\text{Fe II}}$ values from ~ 0 up to more than 1, with the most extreme cases found for the low-redshift radio-quiet Pop. A. quasars. With the exception of these extreme sources, the RQ at high and low z present a very similar distribution, with the mean $R_{\text{Fe II}}$ value for low- z RQ is ~ 0.52 , while for high- z RQ it is ~ 0.55 .

The radio-loud quasars tend to present lower values of $R_{\text{Fe II}}$, which rarely exceeds the threshold of $R_{\text{Fe II}} = 1$. The fact that the RL sources are weaker Fe II emitters than the RQ ones has already been observed in previous studies (e.g., Yuan & Wills 2003; Netzer et al. 2004; Sulentic et al. 2004). In general, the sources that present strong Fe II emission are found to also present very high Eddington ratios, which are more frequently typically found in radio-quiet Pop. A. Hence, this difference in $R_{\text{Fe II}}$ between RL and RQ sources may also be linked to the ac-

Table 11. Radio properties of the full ISAAC sample.

Source	$f_{1.4\text{GHz}}$ [mJy]	$P_{1.4\text{GHz}}$	$\log R_K$	Survey	Radio Class.
(1)	(2)	(3)	(4)	(5)	(6)
ISAAC1					
HE 0001-2340	< 0.90	< 0.15	< 0.48	NVSS	RQ
[HB89]0029+073	< 0.24	< 0.08	< -0.12	FIRST	RQ
CTQ 0408	< 2.49	< 0.85	< 0.43	SUMSS	RQ
SDSSJ005700.18+143737.7	< 0.90	< 0.21	< 0.35	NVSS	RQ
H 0055-2659	< 0.90	< 0.38	< 0.60	NVSS	RQ
SDSSJ114358.52+052444.9	< 0.28	< 0.06	< 0.17	FIRST	RQ
SDSSJ115954.33+201921.1	< 0.29	< 0.11	< -0.04	FIRST	RQ
SDSSJ120147.90+120630.2	< 0.29	< 0.11	< -0.26	FIRST	RQ
SDSSJ132012.33+142037.1	< 0.29	< 0.06	< 0.15	FIRST	RQ
SDSSJ135831.78+050522.8	< 0.28	< 0.06	< -0.15	FIRST	RQ
Q 1410+096	< 0.30	< 0.11	< -0.13	FIRST	RQ
SDSSJ141546.24+112943.4	6.50	1.41	1.27	NVSS	RI
B1422+231	284.67	119	2.78	FIRST	RL
SDSSJ153830.55+085517.0	< 0.31	< 0.12	< 0.36	FIRST	RQ
SDSSJ161458.33+144836.9	< 0.28	< 0.06	< -0.13	FIRST	RQ
PKS 1937-101	838	381	2.99	NVSS	RL
PKS 2000-330	446	202	3.14	NVSS	RL
SDSSJ210524.49+000407.3	2.50	0.46	0.54	NVSS	RQ
SDSSJ210831.56-063022.5	< 0.37	< 0.07	< 0.18	FIRST	RQ
SDSSJ212329.46-005052.9	< 0.29	< 0.05	< -0.45	FIRST	RQ
PKS 2126-15	589	207	2.97	NVSS	RL
SDSSJ235808.54+012507.2	< 0.28	< 0.11	< -0.32	FIRST	RQ
ISAAC2					
PKS0226-038	939	135	3.50	NVSS	RL
PKS0237-23	6256	1043	3.80	NVSS	RL
BZQJ0544-2241	133	10.78	2.06	NVSS	RL
PKS0858-279	1474	233	2.77	NVSS	RL
CTSJ01.03	2.90	0.55	0.92	NVSS	RQ
WB J0948+0855	36.50	4.88	1.78	NVSS	RI
CTSJ03.14	151	30.31	2.40	NVSS	RL
PKS1448-232	439	73.03	2.83	NVSS	RL
[HB89]1559+088	4.50	0.79	0.87	NVSS	RQ
FBQS J2149-0811	< 0.36	< 0.05	< 0.02	FIRST	RQ

Notes. (1) Source identification. (2) Radio flux at 1.4 GHz. (3) Radio power P at 1.4 GHz, in units of 10^{26} W Hz $^{-1}$. (4) Radioloudness parameter. (5) The survey from where we obtain the radio data. (6) Radio classification.

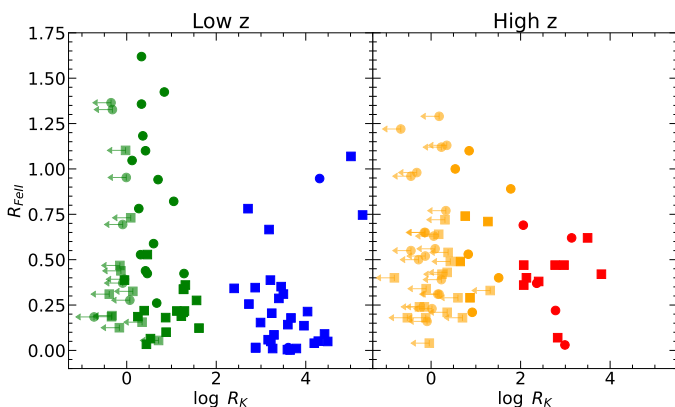


Fig. 7. Relation between radioloudness R_K and R_{FeII} for low- z (left) and high- z (right) ranges. R_K upper limits are indicated by arrows alongside the symbol. Color scheme as in Fig. 4.

cretion rate, which somehow can contribute to enhance the Fe II emission in strong accretors.

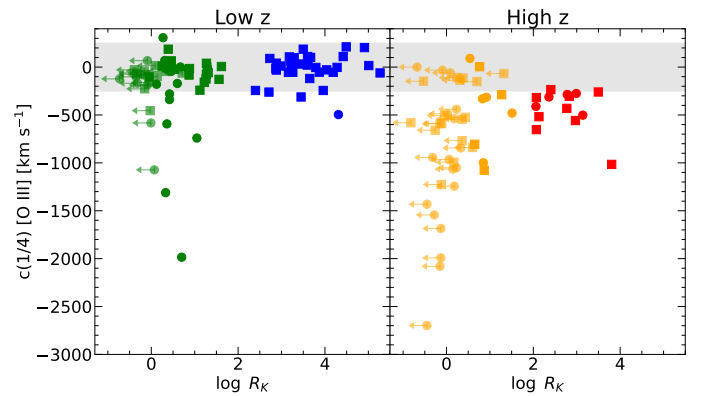


Fig. 8. Relation between radioloudness and velocity centroid at 1/4 intensity of the $[\text{O III}]\lambda 5007$ emission line for low- z (left) and high- z (right) ranges. Grey shaded areas in both plots indicate the $c(1/4)$ range between 250 and -250 km s $^{-1}$. R_K upper limits are indicated by arrows alongside the symbol. Color scheme as in Fig. 4.

The mean R_{FeII} values of low- and high-redshift RL sources are ~ 0.25 and ~ 0.40 , respectively. This result is intriguing, although it may be most easily related to sample differences in Eddington ratio at high- and low- z , with high- z sources at the lowest Eddington ratios missing because they are too faint to be detected in major surveys such as the SDSS (Sulentic et al. 2014).

4.5.2. $[\text{O III}]\lambda 5007$

Fig. 8 shows the relation between R_K and $c(1/4)$ of $[\text{O III}]\lambda 5007$ for low- and high- z ranges separately. In both ranges, RQ sources are the ones with larger outflows velocities compared to RL, with the RQ achieving values of ~ -2000 at low and ~ -2700 km s $^{-1}$ at high z . This difference in outflow velocity between RQ and RL quasars has been already reported in the recent literature (e.g., Marziani et al. 2003b, 2016a; Ganci et al. 2019, and references therein) and may be consequence of the presence of relativistic jets in RL sources that potentially can reduce the impact of the outflows on the optical emission. In contrast, RQ lack such strong radio jets, allowing the outflows to have a more significant influence on the optical emission (e.g., Padovani 2016).

At low redshifts, the majority of the sources (including both RQ and RL) do not exhibit $[\text{O III}]\lambda 5007$ $c(1/4)$ values that exceed 250 km s $^{-1}$, and therefore do not present significant $[\text{O III}]\lambda 5007$ outflows. Only eight objects (seven RQ and one RL) within this redshift range in our FOS sample present relevant $[\text{O III}]\lambda 5007$ blueshifts of ~ -500 km s $^{-1}$.

The right panel of Fig. 8 shows the same analysis but focused on high- z sources. In this redshift range, $\sim 75\%$ of the radio-quiet sources present blueshifts larger than 250 km s $^{-1}$, and in some cases can achieve very strong velocities as is the case of SDSS J212329.46-005052.9 (~ 2700 km s $^{-1}$). All the high-redshift radio-loud sources from our sample present significant blueshifts, with a $[\text{O III}]\lambda 5007$ $c(1/4)$ range between ~ 230 and 1000 km s $^{-1}$.

4.5.3. $\text{C IV}\lambda 1549$

It has been known since long that $[\text{O III}]\lambda 5007$ and $\text{C IV}\lambda 1549$ show similarities in their phenomenology (e.g., Zamanov et al. 2002; Coatman et al. 2019; Deconto-Machado et al. 2023). In

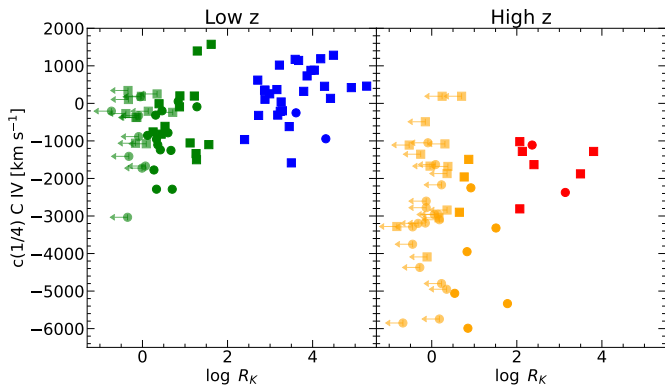


Fig. 9. Relation between radioloudness and velocity centroid at 1/4 intensity of the C IV $\lambda 1549$ emission line for low- z (left) and high- z (right) ranges. R_K upper limits are indicated by arrows alongside the symbol. Color scheme as in Fig. 4.

Fig. 9 we repeat the [O III] $\lambda\lambda 4959, 5007$ analysis described in §4.5.2 for C IV $\lambda 1549$. As for [O III] $\lambda 5007$, the majority of RQ sources at low z present negative values of C IV $\lambda 1549$ $c(1/4)$ while the wide majority of RL have positive values or values very close to 0–500 km s^{−1} to the blue. Regarding the high- z range, it is already known that the largest shifts are also found in RQ sources (see e.g., Richards et al. 2011, 2021, and references therein). This is not different in our high- z sample, case in which practically all sources (including both RQ and RL) present very significant outflow velocities. The average C IV $c(1/4)$ blueshift for RL sources is ~ 1900 km s^{−1}. The relation between the [O III] $\lambda 5007$ and C IV $\lambda 1549$ emission lines does not seem to be affected by the radio emission, however the comparison between RQ and RL at high z for the C IV $\lambda 1549$ emission line is limited by the fact that we have a very small sample of RL in this redshift range (only seven objects, two Pop. A and five Pop. B) and more data are definitely required.

5. Discussion

5.1. Dominance of outflows

C IV $\lambda 1549$ somehow seems to be a magnified version of [O III] $\lambda 5007$, presenting very similar trends however with stronger outflow velocities. The left plot of Fig. 10 shows the relation between the centroid velocity at half intensity ($c(1/2)$) for the full profiles of [O III] $\lambda 5007$ and C IV $\lambda 1549$ at high redshift, including the sources from HEMS, Paper I, and from the present paper. The result reported in Paper I is strengthened: ISAAC2 objects that present strong shifts in the [O III] $\lambda\lambda 4959, 5007$ emission line profiles do present them also in C IV $\lambda 1549$. The bisector linear relation after including all ISAAC data is

$$c(1/2)_{\text{C IV}} = (1.42 \pm 0.23) \times c(1/2)_{[\text{O III}]} + (-1071 \pm 148)$$

with a correlation coefficient ≈ 0.51 . This trend is consistent with the results reported by Coatman et al. (2019) and Vietri et al. (2020) at high redshift.

In both [O III] and C IV, the largest blueshifts are found in Pop. A sources (represented by orange bullets in the figures), which usually present the largest accretion rates. Fig. 10 also shows that the largest outflow velocities in [O III] and in C IV are found in radio-quiet sources, indicating that the accretion may be the main driver of these outflows (Nesvadba et al. 2007; Kukreti et al. 2023). A similar relation is found when considering the $c(1/2)$ of only the outflowing (BLUE) components of

both [O III] $\lambda 5007$ and C IV $\lambda 1549$ emission lines, as shown in the right plot of Fig. 10. In this case, the orthogonal linear relation (with a c.c. of 0.40) is given by:

$$c(1/2)_{\text{C IV, BLUE}} = (1.27 \pm 0.99) \times c(1/2)_{[\text{O III}], \text{BLUE}} + (-1432 \pm 1323)$$

At high z , the outflows appear to be more prominent than at low z (see also Fig. 4), consolidating the idea of accretion rate as the main driver of the outflows. The accretion rate in most of the sources at high z is higher ($-0.6 \lesssim \log L/L_{\text{Edd}} \lesssim 0.4$) than in the case of sources at low z ($-2 \lesssim \log L/L_{\text{Edd}} \lesssim 0$, see also e.g., Cavaliere & Vittorini 2000; Hopkins et al. 2006), even if the difference could be in part due to a selection effect, as recalled in Section 4.5.

5.2. Dynamical parameters of the outflows

The mass outflow rate (\dot{M}), the kinetic power (\dot{E}_{kin}), and the thrust ($\dot{M} v_o$) were estimated adopting a simple biconical outflow, and by using an analogous methodology to the one of Marziani et al. (2016b, 2017). It is summarized in Appendix C. In this framework, the relations are formally identical for [O III] and C IV $\lambda 1549$, and namely:

$$\dot{M}_{\text{ion}} \propto L^{\text{out}} Z^{-1} n_{\text{H}}^{-1},$$

where L is the outflow-emitted line luminosity, n_{H} the electron density and Z the metallicity. The mass outflow rate ($\dot{M}_{\text{ion}}^{\text{out}}$) and the thrust ($\dot{M}_{\text{ion}}^{\text{out}} v_{\text{out}}$) at a radius r and with an outflow velocity v_{out} , might be written as:

$$\dot{M}_{\text{ion}}^{\text{out}} \propto L^{\text{out}} v_{\text{out}} r^{-1} Z^{-1} n_{\text{H}}^{-1}$$

$$\dot{M}_{\text{ion}}^{\text{out}} v_{\text{out}} \propto L^{\text{out}} v_{\text{out}}^2 r^{-1} Z^{-1} n_{\text{H}}^{-1}$$

The kinetic power, \dot{E}_{kin} , is then given by $\dot{E}_{\text{out}} \sim \frac{1}{2} \dot{M}_{\text{out}} v_{\text{out}}^2$, which leads to

$$\dot{E}_{\text{kin}} \propto L^{\text{out}} v_{\text{out}}^3 r^{-1} Z^{-1} n_{\text{H}}^{-1}$$

The parameters entering the previous equations are estimated utilizing different relations for [O III] and C IV, and will be briefly discussed in next sections and Appendix C. The adopted parameters and relevant scaling relations are summarized in Table 12.

When estimating wind parameters in quasars, such as mass outflow rate, thrust, and kinetic power, several sources of error can affect the accuracy of these measurements. These errors arise from various observational and methodological issues, including the complexity of the line profiles, spatial resolution limitations, and assumptions inherent in the models used for interpretation, where the last two are expected to be the dominating sources of uncertainties in the estimation of the wind parameters. Specifically for C IV $\lambda 1549$, the uncertainty in the conversion between line luminosity and ionized gas could be ~ 3 at a 3 σ confidence level. We have considered a range of densities of 0.5 dex around $\log n_{\text{H}}$ radius of the emitting region; Z estimates in quasars suggest very high metallicity, and a range around $5Z_{\odot}$, where between 2 and 20 times solar seems possible both at high and low redshifts (Hamann & Ferland 1993; Garnica et al. 2022; Floris et al. 2024). The geometry of the outflow would contribute a factor 3, via the comparison between the spherically symmetric case and a flat layer. The 1 σ uncertainty in the emitting radius is $\pm 30\%$ if ascribed only to the uncertainty of the scaling law parameter, while uncertainty on the outflow velocity is typically $\sim 30\%$. Propagating quadratically these uncertainties would result in a typical factor ≈ 5 at 1 σ confidence level.

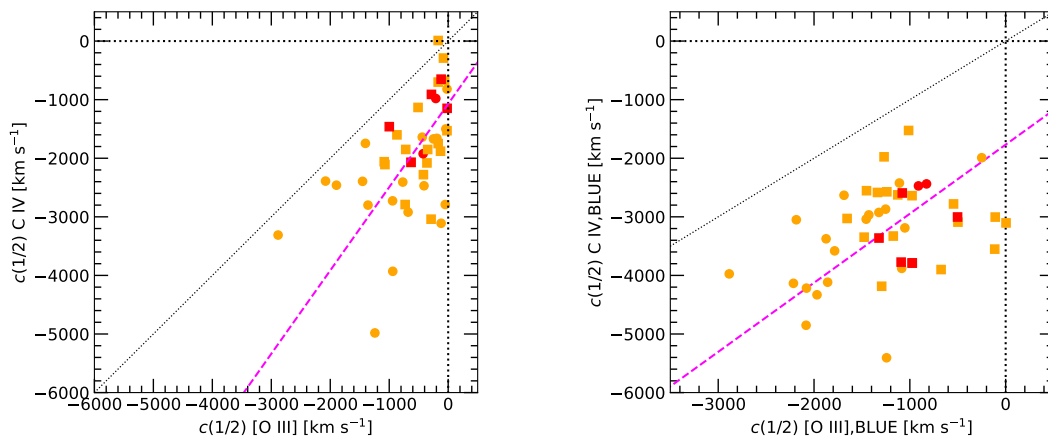


Fig. 10. Centroid velocity at 1/2 flux intensity ($c(1/2)$) of C IV $\lambda 1549$ vs. $c(1/2)$ of [O III] $\lambda 5007$ for the full (*left*) and outflow (*right*) profiles of the high- z sample. The magenta lines indicate the linear regression between $c(1/2)$ of C IV and [O III] for both cases obtained through the bisector method. Dotted black lines represent the 1:1 relation. Color scheme is the same as in Fig. 4.

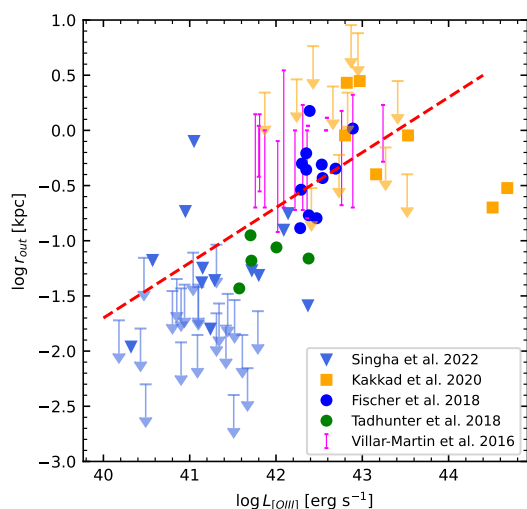


Fig. 11. Relation between the outflow radius in kpc and the luminosity of the [O III] $\lambda 5007$ emission line for the five plotted samples. Red dashed line represents the adopted least squares linear regression. Magenta vertical lines symbolise the minimum and maximum estimated radii in the Villar-Martín sample. Arrows correspond to upper limits.

Similar considerations were applied to [O III]: a factor of ≈ 3 at 1σ in density, a factor of ≈ 2 in Z and in the luminosity-to-ionized mass gas conversion, and a factor of ≈ 2 in the zero point of the radius-luminosity ($L([\text{O III}]])$ relation. These factors contribute to a comparable uncertainty estimate, a factor of ≈ 5 at 1σ confidence level, and should be taken into account in the interpretation of the analysis that follows.

5.2.1. [O III] $\lambda 5007$

The considered situation is the one in which the outflow radius r is allowed to vary depending on the [O III] $\lambda 5007$ luminosity of each source. In the case of sources spanning four orders of magnitude in luminosity, it is nonphysical to assume that the size of the emitting region is constant, as there is evidence of compact emission at low- z (Zamanov et al. 2002), and of kpc-sized outflows at high-luminosity (e.g., Harrison et al. 2014). Conventional scaling laws of narrow-line regions with luminosity are

Table 12. Summary of assumed scaling relations and parameter values for wind dynamics.

Parameter	Low z		High z	
	C IV	[O III]	C IV	[O III]
M_{ion}	$\propto L_{\text{C IV}}^{\text{out}}$	$\propto L_{[\text{O III}]}^{\text{out}}$	$\propto L_{\text{C IV}}^{\text{out}}$	$\propto L_{[\text{O III}]}^{\text{out}}$
$Z [Z_{\odot}]$	5	5	5	2
$n_{\text{H}} [\text{cm}^{-3}]$	$10^{9.5}$	10^3	$10^{9.5}$	10^3
$r [\text{cm}]$	$\propto \lambda L_{\lambda}(1350)$	$\propto L([\text{O III}])$	$\propto \lambda L_{\lambda}(1350)$	$\propto L([\text{O III}])$
$v [\text{km s}^{-1}]$	$c(\frac{1}{2}) + 2\sigma$	$c(\frac{1}{2})$	$c(\frac{1}{2}) + 2\sigma$	$c(\frac{1}{2})$

not expected to exclusively trace the outflowing [O III] component (Bennert et al. 2002, 2006).

In Fig. 11 is shown the outflow radius as a function of the [O III] $\lambda 5007$ luminosity for the integral field spectroscopy (IFU) data analyzed by Villar-Martín et al. (2016), Fischer et al. (2018), Tadhunter et al. (2018), Kakkad et al. (2020), and Singha et al. (2022) where is also represented a least squares linear relation between these two quantities, imposing a slope of 0.5:

$$\log(r) = (0.5) \times \log(L_{[\text{O III}], \text{full}}) + (-21.7 \pm 0.1). \quad (1)$$

The slope 0.5, which gives a reasonable representation of the radius- $L_{[\text{O III}]}$ relation in Fig. 11, is imposed to ensure consistent ionization conditions as a function of luminosity. This scaling relation was then applied to our sources, considering the luminosity of the entire [O III] emission line profile. Our low- z sample exhibits [O III] luminosities (full profile) ranging from approximately $10^{40.6}$ up to $10^{43.1}$ erg s^{-1} , while the high- z sources have luminosities between $10^{43.4}$ and $10^{44.9}$ erg s^{-1} . Consequently, we find [O III] outflows radius r ranging from ~ 0.04 to 0.71 kpc at low- z , in agreement with recent values obtained for IFU resolved [O III] in low- z AGN (see e.g. Deconto-Machado et al. 2022), and from 0.97 to 5.81 kpc at high- z .

The parameters used to estimate the outflow properties associated with the [O III] $\lambda 5007$ emission line are listed in Table 13. The estimated values of the mass rate \dot{M}_{out} , derived from equation C.2 in the Appendix, span from ~ 0.08 to $3.43 M_{\odot} \text{ yr}^{-1}$ for low luminosities ($\lesssim 10^{46}$ erg s^{-1}) and from ~ 6.2 to $114.0 M_{\odot} \text{ yr}^{-1}$ for higher luminosities.

The relations between the [O III] outflow kinetic power \dot{E}_{kin} , and thrust $\dot{M}_{\text{out}} v_o$ with the bolometric luminosity L_{bol} are shown in Fig. 12. We have assumed a density $n_{\text{H}} = 10^3 \text{ cm}^{-3}$ for

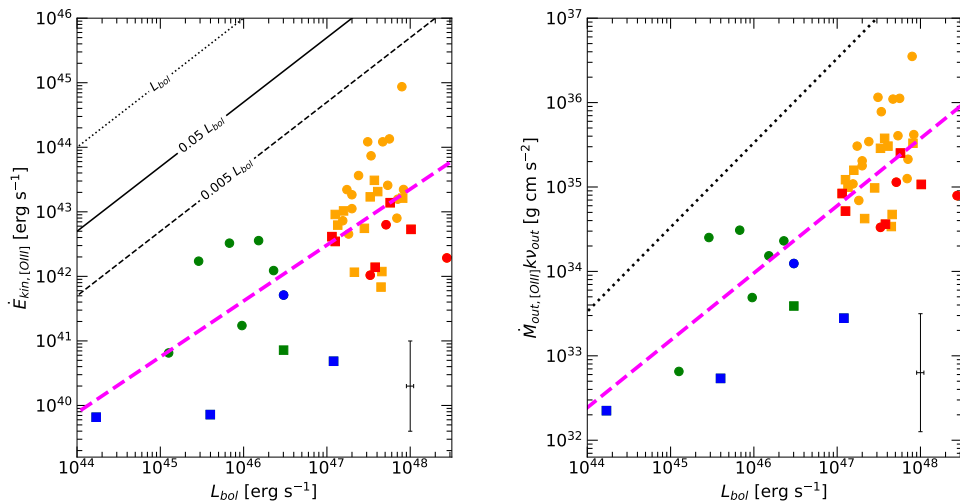


Fig. 12. Kinetic power \dot{E}_{kin} (left) and thrust (right) vs. bolometric luminosity for the [O III] λ 5007 outflow. The two outflow parameters were estimated varying the outflow radius according with Eq. 1 and assuming $v_{\text{out}} = c(1/2)$. Magenta dashed lines indicate the least-squares linear regression. Black dotted, continuous, and dashed lines on the left plot show $\dot{E}_{\text{kin}} = L_{\text{bol}}$, $\dot{E}_{\text{kin}} = 0.05L_{\text{bol}}$, and $\dot{E}_{\text{kin}} = 0.005L_{\text{bol}}$ respectively. Dotted line in the right panel indicates $\dot{M}_{\text{out}}v_o = L_{\text{bol}}/c$. Typical uncertainties are displayed in the bottom-right corner of the plots. Color scheme as in Fig. 4.

both high- and low- z contexts. For metallicity, we have adopted $Z = 5Z_{\odot}$ for low- z , considering the compactness of the outflow, and $Z = 2Z_{\odot}$ for high- z , aligning with the typical values used in the computations for the NLR metallicity at high z (see e.g., Xu et al. 2018). Additionally, as detailed in Section C.1, we assume the outflow velocity to be $c(1/2)$ of the BLUE component. If we instead follow the assumption of $c(1/2) + 2\sigma$ as done by Fiore et al. (2017), it would result in an outflow velocity ~ 2.5 larger in our estimates of the outflow parameters. Typical errors are represented in the errorbars of Fig. 12. The results of the linear correlation analysis between these outflow parameters for [O III] λ 5007 and C IV λ 1549 are reported in Table 14. We find correlation coefficients of 0.66 and 0.74 (with ρ -value of $\sim 10^{-7}$ and $\sim 10^{-9}$, respectively) between the kinetic power and the thrust with the bolometric luminosity. Similar correlations have already been extensively discussed by other authors (e.g. Carniani et al. 2015; Feruglio et al. 2015; Fiore et al. 2017, and references therein).

In our analysis of [O III] \dot{E}_{kin} with luminosity-dependent r , none of the sources display a ratio reaching at least 5% of the bolometric luminosity (filled line in Fig. 12), a threshold needed for a significant impact on the host galaxy dynamics, to account for the black hole mass - velocity dispersion correlation and host-spheroid co-evolution (e.g., Di Matteo et al. 2005). Star formation quenching might be easier, if an AGN outflow induces a wind in the diffuse interstellar medium that in turns induces a flattening and shredding of molecular clouds (Hopkins & Elvis 2010). A threshold for this effect occurs when the kinetic efficiency is much lower than the 5% limit, $\dot{E}_{\text{kin}}/L_{\text{bol}} \sim 5 \times 10^{-3}$ (short dashed line in Fig. 12). Based on the criteria of both Hopkins & Elvis (2010) and Di Matteo et al. (2005), the [O III] λ 5007 outflows parameters accepted at phase value are not providing an efficient feedback mechanism neither at low- nor at high- z (although see the discussion of Section 5.2.3). Similar results have recently been found at low redshift (Kim et al. 2023, and references therein). They derived $\dot{E}_{\text{kin}} \lesssim 0.1\% L_{\text{bol}}$ for a sample of low- z type-1 AGN. It is likely that part of the [O III] emitting gas has already dissipated part of its energy and momentum, as the emitting regions can be extended over several kpc. By the same token, the AGN outflows traced by the [O III] emission are likely

Table 14. Least-squares linear relations ($y = a + b * x$) between different outflows properties and the bolometric luminosity.

y (1)	x (2)	Sources (3)	$a \pm \delta a$ (4)	$b \pm \delta b$ (5)	RMSE (6)	CC (7)	ρ (8)
[O III] λ 5007							
$\log \dot{E}_{\text{kin},44}$	$\log L_{\text{bol},44}$	45	-4.09 ± 0.44	0.86 ± 0.14	0.009	0.69	1.7
$\log \dot{M}_{\text{out}}v_{o,34}$	$\log L_{\text{bol},44}$	45	-1.62 ± 0.31	0.79 ± 0.09	0.017	0.78	2.7
C IV λ 1549							
$\log \dot{E}_{\text{kin},44}$	$\log L_{\text{bol},44}$	68	-3.59 ± 0.25	1.24 ± 0.08	0.075	0.87	2.1
$\log \dot{M}_{\text{out}}v_{o,34}$	$\log L_{\text{bol},44}$	68	-2.08 ± 0.22	1.19 ± 0.07	0.069	0.90	3.7

Notes. (1), (2) Fitted parameters. (3) Number of sources. (4), (5) Linear correlation coefficients. (6) Root mean square root. (7), (8) Pearson r score and its associated null hypothesis probability value.

to impact on the central kiloparsecs scales, but their effects on galactic scale is more debatable.

The thrust ranges from $\sim 2.2 \times 10^{32}$ to 3.1×10^{34} g cm s $^{-2}$, in the case of the low-luminosity sample; at high luminosity, the thrust increases significantly to the larger outflow masses and higher velocities and the values are found between $\sim 3.3 \times 10^{34}$ to 3.5×10^{36} g cm s $^{-2}$. In all cases, however, the [O III] thrust is $\ll L/c$, in agreement with Vietri et al. (2020).

5.2.2. C IV λ 1549

The ionized gas mass producing the C IV λ 1549 line was estimated following the results obtained from CLOUDY photoionization computations by using two different spectral energy distributions (SEDs) representing the two main samples of sources considered in this work: a SED from Mathews & Ferland (1987) for the low- z FOS sample, and the more appropriate SED from Krawczyk et al. (2013) for high luminosity high- z ISAAC and HEMS samples, and taking also into account the constraints imposed by the measures of observed quantities in the spectra as

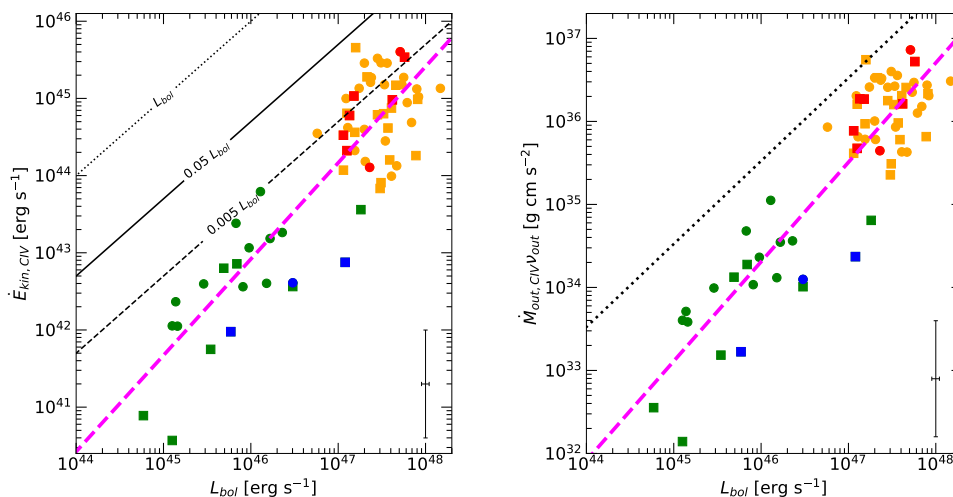


Fig. 13. Kinetic power \dot{E}_{kin} (*left plot*), and thrust (*right*) vs. bolometric luminosity for the C IV 1549 emission line. The two outflow parameters estimated varying outflow radius depending on λL_{λ} as defined in Kaspi et al. (2021). Magenta dashed lines indicate the least squares linear regression. Black dotted, continuous, and dashed lines show $\dot{E}_{\text{kin}} = L_{\text{bol}}$, $\dot{E}_{\text{kin}} = 0.05 L_{\text{bol}}$, and $\dot{E}_{\text{kin}} = 0.005 L_{\text{bol}}$ respectively. Dotted line in the right panel indicates $\dot{M}_{\text{out}} v_o = L_{\text{bol}}/c$. Typical uncertainties are displayed in the bottom-right corner of the plots. Color scheme as in Fig. 4.

Table 15. Average values and standard deviations of the [O III] $\lambda 5007$ and C IV $\lambda 1549$ outflow parameters for the different samples.

Sample	[O III] $\lambda 5007$			C IV $\lambda 1549$		
	\dot{M}_{out} [$M_{\odot} \text{ yr}^{-1}$]	$\dot{M}_{\text{out}} v_o$ [$10^{35} \text{ g cm s}^{-2}$]	\dot{E}_{kin} [$10^{43} \text{ erg s}^{-1}$]	\dot{M}_{out} [$M_{\odot} \text{ yr}^{-1}$]	$\dot{M}_{\text{out}} v_o$ [$10^{36} \text{ g cm s}^{-2}$]	\dot{E}_{kin} [$10^{45} \text{ erg s}^{-1}$]
(1)	(2)	(3)	(4)	(5)	(6)	(7)
ISAAC	34.35 ± 24.73	3.12 ± 3.48	3.50 ± 5.30	38.59 ± 20.25	3.05 ± 1.53	2.03 ± 1.16
HEMS	28.71 ± 30.01	4.07 ± 9.03	10.11 ± 29.33	24.32 ± 14.51	1.18 ± 0.87	0.48 ± 0.45
FOS	1.58 ± 1.12	0.11 ± 0.11	0.24 ± 0.34	0.37 ± 0.39	0.01 ± 0.01	0.01 ± 0.01

Notes. (1) Sample identification. (2), (3), (4) Outflow mass rate, thrust, and kinetic power of [O III] outflows. (5), (6), (7) Same for C IV outflows.

the $W(\text{C IV})$ or the $\text{C IV } \lambda 1549/\text{H}\beta$ ratio. All the calculations and assumptions for the C IV outflow parameters are reported in Appendix C.2. For C IV 1549, we consider that (at variance with the [O III]), the C IV outflow is accelerated to a final outflow velocity of $c(1/2) + 2\sigma$ of the blueshifted component.

As for [O III], we estimated the radius r independently for each source, and based on the luminosity at 1350\AA . In the case of C IV, we use the consolidated scaling relation of Kaspi et al. (2021):

$$\frac{r_{\text{BLR}}}{10 \text{ lt days}} = (0.34 \pm 0.11) \left(\frac{\lambda L_{\lambda}(1350\text{\AA})}{10^{43} \text{ erg s}^{-1}} \right)^{0.45 \pm 0.05}, \quad (2)$$

where r_{BLR} is the radius of the BLR.

For our sources, the specific luminosities at 1350\AA range from approximately $10^{44.5}$ up to $10^{46.5} \text{ erg s}^{-1}$ at low z and from $10^{45.9}$ to $10^{47.6} \text{ erg s}^{-1}$ at high z . With these luminosity values, we find C IV 1549 outflow radii varying from 0.06 to 0.37 pc at high z and 0.01 to 0.11 pc at low z .

In Table 13 we list the properties of the C IV 1549 used in estimating the outflow parameters. The relations between the C IV outflow parameters and the bolometric luminosity are shown in Fig. 13 and the respective linear correlations are reported in Table 14. The outflow parameters considered in this work (kinetic power \dot{E}_{kin} and thrust $\dot{M}_{\text{out}} v_o$) show very good correlations with the bolometric luminosity (as expected), reaching correlation coefficients ~ 0.9 and $P \ll 10^{-20}$ in both cases.

The left plot of Fig. 13 shows the kinetic power of C IV outflows. We find that 15 from 42 high- z sources present a $\dot{E}_{\text{kin}}/L_{\text{bol}}$ ratio $\geq 5 \times 10^{-3}$, 8 of them have $\dot{E}_{\text{kin}}/L_{\text{bol}}$ around 0.01 and 3 sources exhibit a ratio close to 0.05 (between 1 to 3%). The situation is different when we consider the low- z sample. In this case, only two sources, [HB89]1259+593 and [HB89]1543+489, have a $\dot{E}_{\text{kin}}/L_{\text{bol}}$ ratio $\geq 5 \times 10^{-3}$. This is hardly surprising, considering that the luminosity of the BLUE component is highly correlated with 1350\AA luminosity with a slope $\approx 1.8 \gg 1$, and that outflow velocities are systematically higher at high L . At high L , the kinetic power reach values for which a substantial feedback effect might be possible: a considerable fraction of sources present $\dot{E}_{\text{kin}} \geq 0.005 L_{\text{bol}}$ and some of them are close to the limit $0.05 L_{\text{bol}}$ that is the minimum energetic requirement for feedback to lead to the black hole mass - host velocity dispersion relation according to Di Matteo et al. (2005).

The right panel of Fig. 13 shows the behavior of the thrust in different luminosity ranges. Thrust values from $\sim 10^{35}$ to $10^{36} \text{ g cm s}^{-2}$ at high luminosity and from $\sim 10^{32}$ to $10^{35} \text{ g cm s}^{-2}$ at low L . At high luminosity, the thrust values are slightly closer to their AGN L/c momentum rate than at low luminosity. It seems reasonable that the C IV emitting gas in the inner BLR may not have yet suffered losses in energy and momentum (unlike [O III]). In simple word, this would imply that, at least at high L , the outflow is somehow able to exploit the full luminosity of the continuum for its acceleration. Radiative acceleration is apparently less efficient at low- z . The reason for the difference

– at low luminosity most sources remain substantially below the threshold lines at $0.005 L_{\text{bol}}$ and L_{bol}/c – is not entirely clear. A simple explanation is that the acceleration might be involving a smaller fraction of the gas mass at low L . Lowering the gas density by an order of magnitude would reconcile the low- z values with the critical limits. A lower density (or a higher degree of ionization, see Appendix C.2) would increase the gas mass needed to explain the observed line luminosity and thus increase the outflowing gas mass proportionally. Lower density gas might be associated with lower column density gas that can be more efficiently accelerated (Netzer & Marziani 2010).

We conclude that there is the possibility of a significant feedback effect due to the mildly ionized BLR outflow from the high ionization broad line gas observed in luminous quasars at the cosmic noon, and that this possibility appears more remote for lower-luminosity, low- z quasars. This conclusion appears to be valid for both RQ and RL sources: the slightly lower velocities measured on the C IV $\lambda 1549$ profile of the RLs are not enough to significantly affect the outflow dynamical parameters with respect to the RQ population (Fig. 13).

5.2.3. Comparison between the outflow parameters of [O III] $\lambda 5007$ and C IV $\lambda 1549$

The average values and standard deviations of [O III] $\lambda 5007$ and C IV $\lambda 1549$ outflow parameters for the three analysed samples (ISAAC and HEMS at high- z , and FOS at low- z) are listed in Table 13. Fig. 14 presents a comparison between the estimated kinetic power and thrust for the [O III] $\lambda 5007$ (left panel) and C IV $\lambda 1549$ (right panel) emission lines. From the results obtained independently for [O III] and C IV and at high- and low- z , in the previous sections, as well as from the comparison of the outflow parameters in the BLR and NLR through the analysis of both lines, we infer that:

- The ISAAC and HEMS (high-redshift) samples share similar values for the outflow parameters, mass outflow rate, thrust, and kinetic power. This is true for both [O III] and C IV, with the C IV consistently stronger wind parameter than those estimated from [O III]. The FOS (low-redshift) sample exhibits substantially lower values for all outflow parameters (\approx one and two orders of magnitude in [O III] and C IV respectively).
- At high redshift, the C IV outflow parameters indicate a significant influence: 16 out of 42 have $\dot{E}_{\text{kin}} > 0.005 L_{\text{bol}}$, and in some cases, it approaches $\sim 3\%$ of L_{bol} . Regarding [O III], our results suggest that although the outflowing gas at high redshift seems to be induced by the AGN, its impact is possibly restricted to the central kiloparsecs, due to its low efficiency.
- In contrast to the outflows at low redshift, some of the C IV outflows at high redshift exhibit thrust values on the order of L_{bol}/c , suggesting that the outflowing gas in this scenario may be momentum-conserving. This characteristic is not observed in [O III] for both high- and low-redshift ranges.
- It is intriguing that at low- z , C IV and [O III] have consistent thrust values at variance with high-luminosity sources (Fig. 14), even if both of them fall short of the L/c line. Accepted at face value, this might be a consequence of the compactness of the emitting regions in low- z quasars: $\dot{M}_{\text{out}} v_0$ is inversely proportional to the radius and in the case of the low-luminosity NLSy1s, the [O III] emitting regions might be very compact ($\lesssim 10$ pc), therefore preserving a signature of the AGN radiative acceleration.

5.3. A tentative physical explanation for the RL/RQ difference in wind profiles

Observations of the C IV $\lambda 1549$ line in the ISAAC sample suggest systematically lower blueshifts for radio-loud than for radio-quiet quasars in agreement with previous studies both at high and low- z (see e.g. Wills et al. 1995; Sulentic et al. 1995; Corbin & Boroson 1996; Marziani et al. 1996; Richards et al. 2011). According to Sulentic et al. (2015, and references therein), two phenomena might be relevant here.

First, the pressure exerted by the jet in its propagation surpasses the thermal pressure of the BLR gas and the hydrostatic pressure of the expected emitting gas for the blueshifted component attributed to the accretion disc wind. This suggests the existence of an “avoidance zone” near the radio axis, that may be wider in case of powerful relativistic jets, potentially suppressing emission along radial lines close to the jet axis. In addition, the impact on the inner BLR due to the cocoon associated with the relativistic ejection. The wind might start farther from the central BH due to cocoon pressure, reaching a lower terminal velocity.

6. Conclusions

We presented an additional sample of 10 high-redshift, high-luminosity quasars observed with the VLT/ISAAC spectrograph that complete our ISAAC sample, discussed in Paper I. These data cover the H β spectral range, shifted to the near-infrared due to its redshift, and are combined with rest-frame UV spectra, observed in the optical, available in the literature. The analysis at high redshift involves 32 sources from our ISAAC sample and 28 sources from the HEMS survey, including both RL and RQ and with bolometric luminosities in the range from $\approx 10^{47}$ to $10^{48.5}$ [erg s $^{-1}$]. A comparison sample is made with 84 low-redshift, low-luminosity sources selected from the FOS data. We performed a spectroscopic exploration of UV and optical emission line diagnostics along the quasar main sequence, including a dedicated analysis of the differences between RL and RQ sources at both high and low redshifts. Additionally, we investigated the main feedback properties from both the BLR and NLR using high-ionization lines (C IV and [O III], respectively). Our main conclusions are as follows.

1. The shift in the Main Sequence towards broader H β profiles and higher R $_{\text{Fe II}}$ observed at high redshift in Paper I, is confirmed with the inclusion of the 10 new sources. RL quasars from our high- z sample consistently exhibit a tendency towards lower R $_{\text{Fe II}}$ compared to the RQ ones.
2. High- z RL/RQ have stronger outflows than low- z RL/RQ as inferred from both [O III] $\lambda 5007$ and C IV $\lambda 1549$, which indicates that the accretion rate may be the primary driver of these outflows.
3. RL have smaller outflows compared to RQ in both high- and low- z ranges. This suggests that the radio-loudness has a second order effect on the outflow. However, more data on high- z RL is needed.
4. Both RQ and RL outflows may induce a significant feedback effect at the high luminosity encountered in the high- z sample.
5. In the end, the outflow “power” is proportional to the AGN luminosity, via the line luminosity that enters linearly, and the increase of outflow velocity with luminosity that is expected to be weaker ($\propto L^{\frac{1}{4}}$ for a radiation driven wind), but to become significant if a luminosity range as large as $\sim 10^3 - 10^4$ is considered, as in the case of the samples presented in this paper. Within limited luminosity ranges, the

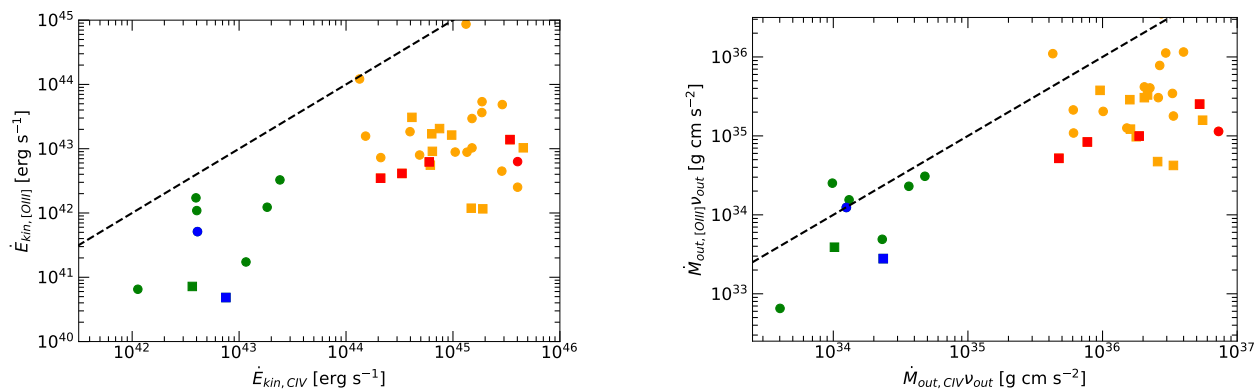


Fig. 14. Comparison between the kinetic power \dot{E}_{kin} (left), and thrust (right) of [O III] λ 5007 and C IV λ 1549 outflows, for high- z (orange and red symbols) and low- z (blue and green symbols) sources. Both parameters have been estimated by evaluating the outflow radius in each source according Eqs.1 and 2 for [O III] and C IV respectively. Black dashed lines indicate the 1:1 relation. Color scheme as in Fig. 4.

dominant effect is associated with the radiative output per unit mass (i.e., the Eddington ratio).

6. The C IV λ 1549 line follows the same trends of [O III] λ 5007, however with larger outflow velocities and stronger outflow parameters. The relations between these two emission lines does not seem to be affected by the radio emission.

Our findings suggest that, regardless of the influence of accretion and radio emission, the outflow is likely to significantly affect the host galaxy at high luminosity. Less clear is the role of outflows from the BLR and NLR at low- z due to the much lower luminosity, and smaller outflow velocity.

Acknowledgements. The authors thank the anonymous referee for his/her valuable suggestions that helped us to improve the present paper. A.D.M. and A.d.O. acknowledge financial support from the Spanish MCIU through projects PID2019-106027GB-C41, PID2022-140871NB-C21 by “ERDF A way of making Europe”, and the Severo Ochoa grant CEX2021- 515001131-S funded by MCIN/AEI/10.13039/501100011033. A.D.M. acknowledges the support of the INPhINIT fellowship from “la Caixa” Foundation (ID 100010434). The fellowship code is LCF/BQ/DI19/11730018. A.D.M. is very thankful for the kind hospitality at the Padova Astronomical Observatory. This research has made use of the NASA/IPAC Extragalactic Database (NED) which is operated by the Jet Propulsion Laboratory, California Institute of Technology, under contract with the National Aeronautics and Space Administration. In this work, we made use of astronomical tool IRAF, which is distributed by the National Optical Astronomy Observatories, and archival data from FIRST, NVSS, and 2MASS. Funding for SDSS-III has been provided by the Alfred P. Sloan Foundation, the Participating Institutions, the National Science Foundation, and the U.S. Department of Energy Office of Science. The SDSS-III web site is <http://www.sdss3.org/>.

References

- Ayubinia, A., Woo, J.-H., Rakshit, S., & Son, D. 2023, *ApJ*, 954, 27
- Bachev, R., Marziani, P., Sulentic, J. W., et al. 2004, *ApJ*, 617, 171
- Becker, R. H., White, R. L., & Helfand, D. J. 1995, *ApJ*, 450, 559
- Bennert, N., Falcke, H., Schulz, H., Wilson, A. S., & Wills, B. J. 2002, *ApJ*, 574, L105
- Bennert, N., Jungwiert, B., Komossa, S., Haas, M., & Chini, R. 2006, *A&A*, 459, 55
- Bian, W., Yuan, Q., & Zhao, Y. 2005, *MNRAS*, 364, 187
- Bischetti, M., Piconcelli, E., Vietri, G., et al. 2017, *A&A*, 598, A122
- Bonzini, M., Mainieri, V., Padovani, P., et al. 2015, *MNRAS*, 453, 1079
- Boroson, T. A. & Green, R. F. 1992, *ApJS*, 80, 109
- Breiding, P., Chiaberge, M., Lambrides, E., et al. 2023, arXiv e-prints, arXiv:2305.11804
- Buendia-Rios, T. M., Negrete, C. A., Marziani, P., & Dultzin, D. 2022, arXiv e-prints, arXiv:2209.05526
- Buttiglione, S., Capetti, A., Celotti, A., et al. 2010, *A&A*, 509, A6
- Caccianiga, A., Antón, S., Ballo, L., et al. 2015, *MNRAS*, 451, 1795
- Cano-Díaz, M., Maiolino, R., Marconi, A., et al. 2012, *A&A*, 537, L8
- Carniani, S., Marconi, A., Maiolino, R., et al. 2015, *A&A*, 580, A102
- Cavaliere, A. & Vittorini, V. 2000, *ApJ*, 543, 599
- Coatman, L., Hewett, P. C., Banerji, M., & Richards, G. T. 2016, *MNRAS*, 461, 647
- Coatman, L., Hewett, P. C., Banerji, M., et al. 2019, *MNRAS*, 486, 5335
- Condon, J. J., Cotton, W. D., Greisen, E. W., et al. 1998, *AJ*, 115, 1693
- Condon, J. J., Kellermann, K. I., Kimball, A. E., Ivezić, Ž., & Perley, R. A. 2013, *ApJ*, 768, 37
- Corbin, M. R. & Boroson, T. A. 1996, *ApJS*, 107, 69
- Coziol, R., Andernach, H., Torres-Papaqui, J. P., Ortega-Minakata, R. A., & Moreno del Rio, F. 2017, *MNRAS*, 466, 921
- Cracco, V., Ciroi, S., Berton, M., et al. 2016, *MNRAS*, 462, 1256
- Deconto-Machado, A., del Olmo Orozco, A., Marziani, P., Perea, J., & Stirpe, G. M. 2023, *A&A*, 669, A83
- Deconto-Machado, A., Riffel, R. A., Ilha, G. S., et al. 2022, *A&A*, 659, A131
- Di Matteo, T., Springel, V., & Hernquist, L. 2005, *Nature*, 433, 604
- Diamond-Stanic, A. M., Fan, X., Brandt, W. N., et al. 2009, *ApJ*, 699, 782
- Duras, F., Bongiorno, A., Piconcelli, E., et al. 2017, *A&A*, 604, A67
- Duras, F., Bongiorno, A., Ricci, F., et al. 2020, *A&A*, 636, A73
- Ferland, G. J., Chatzikos, M., Guzmán, F., et al. 2017, *Rev. Mexicana Astron. Astrofis.*, 53, 385
- Feruglio, C., Fiore, F., Carniani, S., et al. 2015, *A&A*, 583, A99
- Fiore, F., Feruglio, C., Shankar, F., et al. 2017, *A&A*, 601, A143
- Fischer, T. C., Kraemer, S. B., Schmitt, H. R., et al. 2018, *ApJ*, 856, 102
- Floris, A., Marziani, P., Panda, S., et al. 2024, arXiv e-prints, arXiv:2405.04456
- Fraix-Burnet, D., Marziani, P., D’Onofrio, M., & Dultzin, D. 2017, *Frontiers in Astronomy and Space Sciences*, 4, 1
- Ganci, V., Marziani, P., D’Onofrio, M., et al. 2019, *A&A*, 630, A110
- Garnica, K., Negrete, C. A., Marziani, P., et al. 2022, *A&A*, 667, A105
- Gregg, M. D., Becker, R. H., White, R. L., et al. 1996, *AJ*, 112, 407
- Hamann, F. & Ferland, G. 1993, *ApJ*, 418, 11
- Harrison, C. M., Alexander, D. M., Mullaney, J. R., & Swinbank, A. M. 2014, *MNRAS*, 441, 3306
- Hopkins, P. F. & Elvis, M. 2010, *MNRAS*, 401, 7
- Hopkins, P. F., Hernquist, L., Cox, T. J., et al. 2006, *ApJS*, 163, 1
- Jin, C., Done, C., Ward, M., et al. 2023, *MNRAS*, 518, 6065
- Kakkad, D., Mainieri, V., Vietri, G., et al. 2020, *A&A*, 642, A147
- Kaspi, S., Brandt, W. N., Maoz, D., et al. 2021, *ApJ*, 915, 129
- Kim, C., Woo, J.-H., Luo, R., et al. 2023, *ApJ*, 958, 145
- Kinney, A. L., Rivolo, A. R., & Koratkar, A. P. 1990, *ApJ*, 357, 338
- Komossa, S., Xu, D., Zhou, H., Storchi-Bergmann, T., & Binette, L. 2008, *ApJ*, 680, 926
- Kovačević-Dojčinović, J. & Popović, L. Č. 2015, *ApJS*, 221, 35
- Krawczyk, C. M., Richards, G. T., Mehta, S. S., et al. 2013, *ApJS*, 206, 4
- Kriss, G. 1994, *A.S.P. Conference Series*, 61, 437
- Kukreti, P., Morganti, R., Tadhunter, C., & Santoro, F. 2023, *A&A*, 674, A198
- Laor, A. 2018, *Monthly Notices of the Royal Astronomical Society*
- Laor, A. & Brandt, W. N. 2002, *ApJ*, 569, 641
- Martínez-Aldama, M. L., del Olmo, A., Marziani, P., et al. 2018, *A&A*, 618, A179
- Marziani, P., Deconto-Machado, A., & Del Olmo, A. 2022a, *Galaxies*, 10, 54
- Marziani, P., Dultzin, D., Sulentic, J. W., et al. 2018, *Frontiers in Astronomy and Space Sciences*, 5, 6
- Marziani, P., Martínez Carballo, M. A., Sulentic, J. W., et al. 2016a, *Ap&SS*, 361, 29

- Marziani, P., Martínez Carballo, M. A., Sulentic, J. W., et al. 2016b, *Ap&SS*, 361, 29
- Marziani, P., Negrete, C. A., Dultzin, D., et al. 2017, *Frontiers in Astronomy and Space Sciences*, 4, 16
- Marziani, P., Olmo, A. d., Negrete, C. A., et al. 2022b, *ApJS*, 261, 30
- Marziani, P., Sulentic, J. W., Dultzin-Hacyan, D., Calvani, M., & Moles, M. 1996, *ApJS*, 104, 37
- Marziani, P., Sulentic, J. W., Stirpe, G. M., et al. 2016c, *Ap&SS*, 361, 3
- Marziani, P., Sulentic, J. W., Stirpe, G. M., Zamfir, S., & Calvani, M. 2009, *A&A*, 495, 83
- Marziani, P., Sulentic, J. W., Zamanov, R., et al. 2003a, *ApJS*, 145, 199
- Marziani, P., Sulentic, J. W., Zwitter, T., Dultzin-Hacyan, D., & Calvani, M. 2001, *ApJ*, 558, 553
- Marziani, P., Zamanov, R. K., Sulentic, J. W., & Calvani, M. 2003b, *MNRAS*, 345, 1133
- Massaro, E., Maselli, A., Leto, C., et al. 2015, *Ap&SS*, 357, 75
- Massaro, F., Giroletti, M., D'Abrusco, R., et al. 2014, *ApJS*, 213, 3
- Mathews, W. G. & Ferland, G. J. 1987, *ApJ*, 323, 456
- Mauch, T., Murphy, T., Buttery, H. J., et al. 2003, *MNRAS*, 342, 1117
- Mengistuae, S. T., Del Olmo, A., Marziani, P., et al. 2023, *MNRAS*, 525, 4474
- Nesvadba, N. P. H., Lehnert, M. D., De Breuck, C., Gilbert, A., & van Breugel, W. 2007, *A&A*, 475, 145
- Netzer, H. 2019, *MNRAS*, 488, 5185
- Netzer, H. & Marziani, P. 2010, *ApJ*, 724, 318
- Netzer, H., Shemmer, O., Maiolino, R., et al. 2004, *ApJ*, 614, 558
- Osterbrock, D. E. & Ferland, G. J. 2006, *Astrophysics of gaseous nebulae and active galactic nuclei*
- Padovani, P. 2016, *A&A Rev.*, 24, 13
- Panessa, F., Baldi, R. D., Laor, A., et al. 2019, *Nature Astronomy*, 3, 387
- Patil, P., Whittle, M., Nyland, K., et al. 2022, *ApJ*, 934, 26
- Perlman, E. S., Padovani, P., Giommi, P., et al. 1998, *AJ*, 115, 1253
- Punsly, B. 2010, *ApJ*, 713, 232
- Richards, G. T., Kruczek, N. E., Gallagher, S. C., et al. 2011, *AJ*, 141, 167
- Richards, G. T., McCaffrey, T. V., Kimball, A., et al. 2021, *AJ*, 162, 270
- Shemmer, O., Trakhtenbrot, B., Anderson, S. F., et al. 2010, *ApJ*, 722, L152
- Shen, Y. & Ho, L. C. 2014, *Nature*, 513, 210
- Sikora, M., Stawarz, Ł., & Lasota, J.-P. 2007, *ApJ*, 658, 815
- Singha, M., Husemann, B., Urrutia, T., et al. 2022, *A&A*, 659, A123
- Skrutskie, M. F., Cutri, R. M., Stiening, R., et al. 2006, *AJ*, 131, 1163
- Śniegowska, M., Marziani, P., Czerny, B., et al. 2021, *ApJ*, 910, 115
- Stickel, M., Kuehr, H., & Fried, J. W. 1993, *A&AS*, 97, 483
- Sulentic, J., Marziani, P., & Zamfir, S. 2011, *Baltic Astronomy*, 20, 427
- Sulentic, J. W., Bachev, R., Marziani, P., Negrete, C. A., & Dultzin, D. 2007, *ApJ*, 666, 757
- Sulentic, J. W., del Olmo, A., Marziani, P., et al. 2017, *A&A*, 608, A122
- Sulentic, J. W., Martínez-Carballo, M. A., Marziani, P., et al. 2015, *MNRAS*, 450, 1916
- Sulentic, J. W., Marziani, P., del Olmo, A., et al. 2014, *A&A*, 570, A96
- Sulentic, J. W., Marziani, P., & Dultzin-Hacyan, D. 2000a, *ARA&A*, 38, 521
- Sulentic, J. W., Marziani, P., Dultzin-Hacyan, D., Calvani, M., & Moles, M. 1995, *ApJL*, 445, L85
- Sulentic, J. W., Marziani, P., Zamanov, R., et al. 2002, *ApJ*, 566, L71
- Sulentic, J. W., Repetto, P., Stirpe, G. M., et al. 2006, *A&A*, 456, 929
- Sulentic, J. W., Stirpe, G. M., Marziani, P., et al. 2004, *A&A*, 423, 121
- Sulentic, J. W., Zwitter, T., Marziani, P., & Dultzin-Hacyan, D. 2000b, *ApJL*, 536, L5
- Sulentic, J. W., Zwitter, T., Marziani, P., & Dultzin-Hacyan, D. 2000c, *ApJ*, 536, L5
- Tadhunter, C., Rodríguez Zaurín, J., Rose, M., et al. 2018, *MNRAS*, 478, 1558
- Temple, M. J., Ferland, G. J., Rankine, A. L., et al. 2020, *MNRAS*, 496, 2565
- Temple, M. J., Mathews, J. H., Hewett, P. C., et al. 2023, *arXiv e-prints*, arXiv:2301.02675
- Tytler, D., O'Meara, J. M., Suzuki, N., et al. 2004, *AJ*, 128, 1058
- Véron-Cetty, M. P. & Véron, P. 2010, *A&A*, 518, A10
- Vestergaard, M. & Peterson, B. M. 2006, *ApJ*, 641, 689
- Vestergaard, M. & Wilkes, B. J. 2001, *ApJS*, 134, 1
- Vietri, G., Maimieri, V., Kakkad, D., et al. 2020, *A&A*, 644, A175
- Vietri, G., Piconcelli, E., Bischetti, M., et al. 2018, *A&A*, 617, A81
- Villar-Martín, M., Arribas, S., Emonts, B., et al. 2016, *MNRAS*, 460, 130
- Wang, J., Xu, D. W., & Wei, J. Y. 2018, *ApJ*, 852, 26
- Wilkes, B. J., Wright, A. E., Jauncey, D. L., & Peterson, B. A. 1983, *PASA*, 5, 2
- Wills, B. J., Thompson, K. L., Han, M., et al. 1995, *ApJ*, 447, 139
- Wolf, J., Salvato, M., Coffey, D., et al. 2020, *MNRAS*, 492, 3580
- Woo, J.-H. & Urry, C. M. 2002, *ApJ*, 581, L5
- Wu, J., Brandt, W. N., Anderson, S. F., et al. 2012, *ApJ*, 747, 10
- Xu, F., Bian, F., Shen, Y., et al. 2018, *MNRAS*, 480, 345
- Yuan, M. J. & Wills, B. J. 2003, *ApJ*, 593, L11
- Zamanov, R., Marziani, P., Sulentic, J. W., et al. 2002, *ApJ*, 576, L9
- Zamfir, S., Sulentic, J. W., & Marziani, P. 2008, *MNRAS*, 387, 856
- Zamfir, S., Sulentic, J. W., Marziani, P., & Dultzin, D. 2010, *MNRAS*, 403, 1759
- Zhang, K., Dong, X.-B., Wang, T.-G., & Gaskell, C. M. 2011, *ApJ*, 737, 71

Table 13. Properties of the [O III] λ 5007 and C IV λ 1549 outflows for the objects of each sample considered in this work that present clear outflows.

Source (1)	[O III]						C IV				
	L_{bol} [erg s $^{-1}$] (2)	L_{full} [erg s $^{-1}$] (3)	L_{SBC} [erg s $^{-1}$] (4)	r_{out} [kpc] (5)	$I_{\text{SBC}}/I_{\text{tot}}$ (6)	$c(1/2)_{\text{SBC}}$ [km s $^{-1}$] (7)	L_{BLUE} [erg s $^{-1}$] (8)	$L(1350\text{\AA})$ [erg s $^{-1}$] (9)	r_{out} [pc] (10)	$c(1/2)_{\text{BLUE}}$ [km s $^{-1}$] (11)	$\text{FWHM}_{\text{BLUE}}$ [km s $^{-1}$] (12)
ISAAC1+ISAAC2											
[HB89] 0029+073	47.65	44.02	43.97	2.03	1.00	-396					no C IV spectrum available
SDSSJ005700.18+143737.7	47.56	[O III] not covered by the spectrum					44.74	46.73	0.14	-4765	13187
PKS0226-038	47.18	full [O III] $c(1/2) > -250$ km s $^{-1}$					44.77	46.81	0.15	-2593	10535
PKS0237-23	47.76	44.06	43.98	2.13	0.83	-1091	45.43	47.48	0.30	-3773	10778
BZQJ0544-2241	47.52	43.81	43.47	1.60	0.45	-620					C IV at the edge of the spectrum
CTSJ01.03	47.37	full [O III] $c(1/2) > -250$ km s $^{-1}$					45.49	47.68	0.37	-2423	9263
WB J0948+0855	47.45	no [O III] outflow detected					44.29	46.97	0.17	-6917	22060
CTSJ03.14	47.62	full [O III] $c(1/2) > -250$ km s $^{-1}$					45.05	47.59	0.33	-3003	10299
SDSSJ114358.52+052444.9	47.20	43.41	43.31	1.02	0.78	-1294	45.17	47.30	0.25	-4185	14345
SDSSJ115954.33+201921.1	47.66	44.32	44.06	2.89	0.55	-498	45.21	47.47	0.29	-3090	9933
SDSSJ120147.90+120630.2	47.91	44.65	44.49	4.20	0.62	-977	45.32	47.40	0.27	-2639	7464
SDSSJ132012.33+142037.1	47.24	43.98	43.79	1.95	0.64	-1428	45.04	46.87	0.16	-2967	8739
SDSSJ135831.78+050522.8	47.49	44.16	44.13	2.39	0.90	-2079	45.05	47.12	0.20	-4217	11983
Q1410+096	47.73	44.34	44.20	2.95	0.73	-1254	44.88	47.15	0.21	-4135	10881
PKS1448-232	47.58	44.11	43.49	2.27	0.24	-753					no C IV spectrum available
SDSSJ153830.55+085517.0	47.33	43.56	43.56	1.20	1.00	-544	45.31	47.39	0.27	-2780	10024
[HB89]1559+088	47.57	44.06	43.82	2.15	0.56	-1611	44.92	47.21	0.22	-2554	7129
SDSSJ161458.33+144836.9	47.53	44.18	44.06	2.45	0.75	-1874	45.15	47.26	0.24	-3375	9333
PKS1937-101	48.44	44.79	44.55	4.97	0.57	-483					no C IV spectrum available
PKS2000-330	47.71	44.43	44.06	3.27	0.42	-826	45.27	46.50	0.11	-4325	7835
SDSSJ210524.49+000407.3	47.79	full [O III] $c(1/2) > -250$ km s $^{-1}$					44.71	47.40	0.27	-5071	10418
SDSSJ210831.56-063022.5	47.30	43.37	43.37	0.97	1.00	-1243	44.88	47.22	0.23	-5406	13618
SDSSJ212329.46-005052.9	47.75	43.95	43.90	1.88	0.88	-2376	45.21	47.51	0.31	-3974	10217
PKS2126-15	48.01	44.38	43.85	3.08	0.30	-988					no C IV spectrum available
FBQSJ2149-0811	47.26	43.68	43.08	1.38	0.25	-1291					no C IV spectrum available
SDSSJ235808.54+012507.2	47.92	44.40	44.40	3.15	1.00	-1052	45.04	47.08	0.20	-3189	8302
HEMS											
HE0035-2853	47.19	full [O III] $c(1/2) > -250$ km s $^{-1}$					44.79	46.73	0.14	-3028	5530
HE0043-2300	47.36	full [O III] $c(1/2) > -250$ km s $^{-1}$					44.73	46.75	0.14	-2472	3840
HE0058-3231	47.49	full [O III] $c(1/2) > -250$ km s $^{-1}$					44.63	46.70	0.13	-3004	5200
HE0109-3518	47.61	full [O III] $c(1/2) > -250$ km s $^{-1}$					45.31	47.63	0.35	-1991	3020
HE0122-3759	47.38	43.65	43.35	1.34	0.63	-2083	45.17	47.08	0.20	-4851	7520
HE0203-4627	47.10	43.41	42.80	1.02	0.24	-1322	44.25	46.46	0.10	-3362	6450
HE0205-3756	47.85	46.84	43.56	1.73	0.48	-1456	45.14	47.11	0.20	-3040	4640
HE0248-3628	46.76	full [O III] $c(1/2) > -250$ km s $^{-1}$					44.80	46.98	0.18	-3880	5140
HE0251-5550	47.84	44.42	43.74	3.22	0.16	-1253	45.45	47.38	0.27	-2869	4170
HE0349-5249	47.89	full [O III] $c(1/2) > -250$ km s $^{-1}$					45.07	47.06	0.19	-3104	5525
HE0359-3959	47.11	[O III] region dominated by Fe II					44.11	46.54	0.11	-6042	7940
HE0436-3709	47.48	full [O III] $c(1/2) > -250$ km s $^{-1}$					44.05	45.97	0.06	-3551	5670
HE0507-3236	47.19	43.82	43.32	1.61	0.36	-1323	44.68	46.69	0.13	-2925	4720
HE0512-3329	47.30	43.77	43.31	1.52	0.40	-1785	44.63	46.32	0.09	-3581	5000
HE0926-0201	47.61	44.31	44.01	2.84	0.41	-1338	45.36	47.13	0.21	-2584	5560
HE0940-1050	47.90	44.93	44.26	5.81	0.75	-4857	45.40	47.48	0.30	-4331	6270
HE1039-0724	47.06	full [O III] $c(1/2) > -250$ km s $^{-1}$					44.70	46.73	0.14	-1976	4350
HE1104-1805	47.54	full [O III] $c(1/2) > -250$ km s $^{-1}$					45.08	47.15	0.21	-2632	4610
HE1120+0154	47.59	full [O III] $c(1/2) > -250$ km s $^{-1}$					45.08	47.06	0.19	-1526	4400
HE1347-2457	48.17	[O III] region dominated by Fe II					45.54	47.53	0.31	-5538	7720
HE1349+0007	47.10	43.42	43.08	1.03	0.35	-1477	45.06	46.85	0.16	-3347	5377
HE1409+0101	47.52	44.18	44.03	2.46	0.74	-1173	45.11	46.97	0.17	-3328	5390
HE2147-3212	47.09	full [O III] $c(1/2) > -250$ km s $^{-1}$					44.96	46.82	0.15	-4116	6650
HE2156-4020	47.45	43.66	43.34	1.35	0.51	-1126	45.46	47.38	0.27	-2625	5000
HE2202-2557	47.13	43.53	43.20	1.16	0.38	-1240	45.22	46.66	0.13	-2573	4490
HE2349-3800	47.06	43.69	43.41	1.40	0.65	-975	44.48	46.45	0.10	-3788	5710
HE2352-4010	47.67	44.25	44.11	2.67	0.79	-2185	44.82	47.14	0.21	-3050	3760
FOS											
PG 0044+030	46.48	43.05	43.00	0.66	0.75	-366	42.01	46.01	0.06	-3251	4580

Table 13. Properties of the [O III] λ 5007 and C IV λ 1549 outflows for the objects of each sample considered in this work. (cont.)

Source (1)	[O III]						C IV				
	L_{bol} [erg s $^{-1}$] (2)	L_{full} [erg s $^{-1}$] (3)	L_{SBC} [erg s $^{-1}$] (4)	r_{out} [kpc] (5)	$I_{\text{SBC}}/I_{\text{tot}}$ (6)	$c(1/2)_{\text{SBC}}$ [km s $^{-1}$] (7)	L_{BLUE} [erg s $^{-1}$] (8)	$L(1350\text{\AA})$ [erg s $^{-1}$] (9)	r_{out} [pc] (10)	$c(1/2)_{\text{BLUE}}$ [km s $^{-1}$] (11)	$\text{FWHM}_{\text{BLUE}}$ [km s $^{-1}$] (12)
Mrk 1502	45.46	41.14	40.73	0.07	0.55	-1352	41.25	44.58	0.01	-2270	6750
3C 057	46.48	43.10	42.84	0.71	0.61	-817	42.38	46.45	0.10	-3355	3697
3C 84	44.23	42.32	41.25	0.28	0.91	-437	C IV strongly affected by noise				
LEDA 75249	45.84	no [O III] outflow detected					42.01	45.53	0.04	-2206	6318
[HB89] 0850+440	46.18	42.37	42.10	0.31	0.54	-1396	42.12	45.71	0.05	-2926	3739
SDSS J100402.61+285535.3	46.36	42.88	42.77	0.55	0.70	-1058	42.18	45.81	0.05	-3198	8043
PG 1116+215	45.98	42.83	42.44	0.52	0.36	-700	41.93	45.68	0.05	-2882	8348
LBQS 1138+0204	45.69	no [O III] outflow detected					41.57	45.32	0.03	-2553	8122
3C 273	47.08	43.10	42.94	0.71	0.69	-344	42.62	46.35	0.09	-1645	5587
SBS 1259+593	46.11	no [O III] outflow detected					42.74	46.15	0.07	-3866	8394
FBQS J131217.7+351521	45.60	42.15	41.98	0.24	0.62	-264	full C IV $c(1/2) > -250$, strongly affected by absorption				
FBQS J1405+2555	45.14	no [O III] outflow detected					41.23	45.37	0.03	-3841	6074
[HB89] 1415+451	45.10	40.62	40.60	0.04	1.00	-593	41.21	44.65	0.02	-1472	4862
[HB89] 1425+267	45.54	no [O III] outflow detected					40.64	44.82	0.02	-4283	3543
Mrk 478	45.16	no [O III] outflow detected					41.26	44.89	0.02	-1526	5032
[HB89] 1444+407	45.91	no [O III] outflow detected					41.92	45.64	0.04	-3110	4232
[HB89] 1538+477	47.26	no [O III] outflow detected					42.64	46.49	0.11	-3492	9104
[HB89] 1543+489	45.83	41.89	41.81	0.18	0.84	-2105	42.30	45.81	0.05	-3301	7901
Mrk 509	45.10	no [O III] outflow detected					39.73	44.52	0.01	-2713	3069
PG 2112+059	46.22	no [O III] outflow detected					42.33	45.90	0.06	-3120	6573
MR 2251-178	44.77	no [O III] outflow detected					40.32	44.54	0.01	-2363	2334
[HB89] 2349-014	45.77	no [O III] outflow detected					40.17	44.53	0.01	-5746	6476

Notes. (1) Source identification. (2) Bolometric luminosity. (3) Luminosity of the [O III] full profile applied in the scaling law for estimating the outflow radius r_{out} (Eq. 1). (4) Luminosity of only the [O III] outflowing component, named AS SBC for [O III]. (5) [O III] outflow radius estimated using the Eq. 1. (6) [O III] SBC relative intensity. (7) Outflow velocity that we assume to be the centroid at $\frac{1}{2}$ intensity of the [O III] SBC component. (8) Luminosity of the C IV outflowing BLUE component. (9) Specific luminosity at 1350Å, entering in Eq. 2. (10) Estimated C IV outflow radius. (11) C IV outflow velocity. (12) FWHM of the C IV λ 1549 BLUE component.

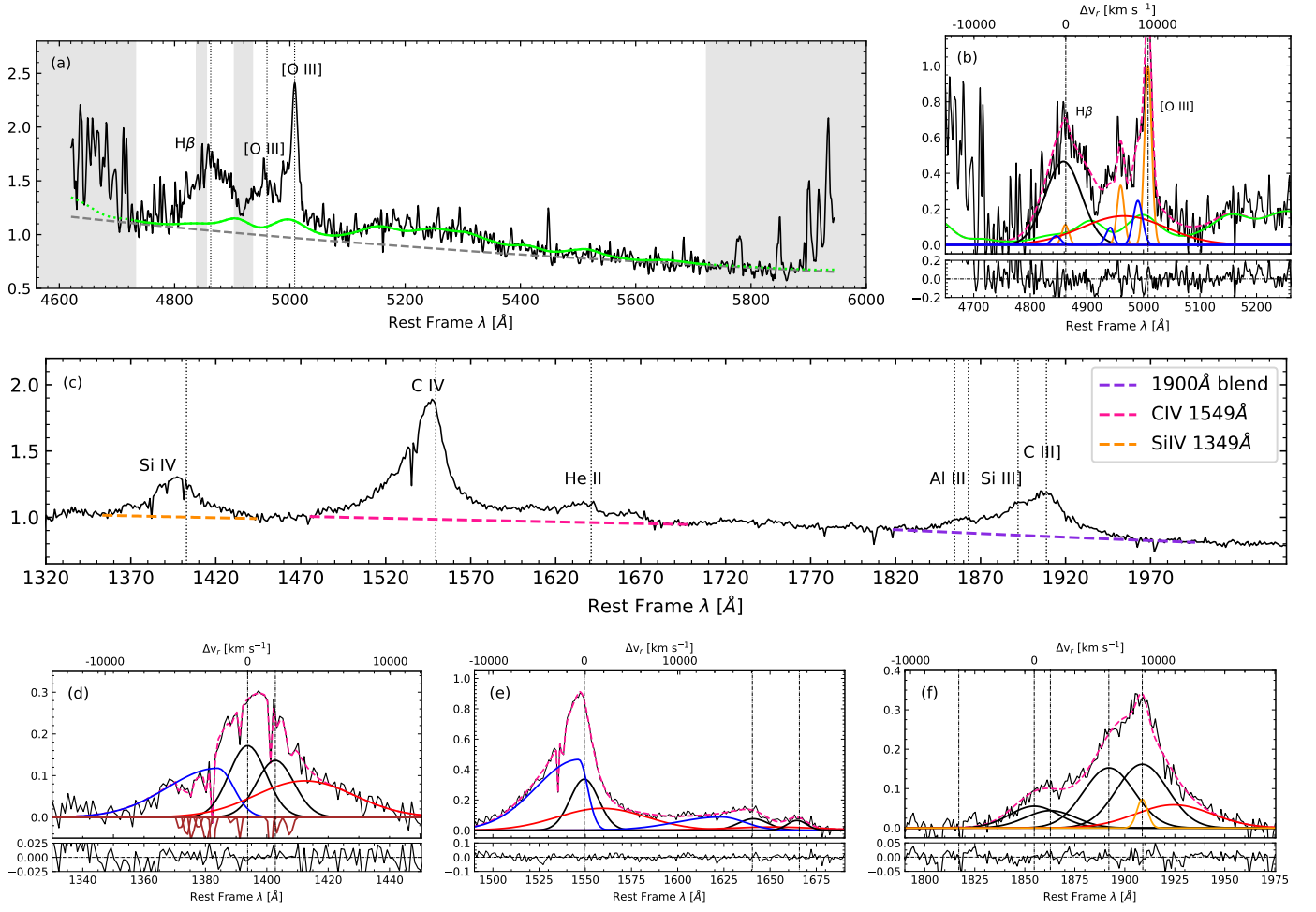
Appendix A: Multicomponent fits in the optical and UV ranges and individual notes
Appendix A.1: PKS0226-038


Fig. A.1. PKS0226-038. (a) Rest-frame spectrum covering the $H\beta$ spectral range obtained with VLT/ISAAC. The spectrum is normalised by the continuum at 5100 \AA . The grey dashed line traces the power law that represent the continuum level as obtained with the `specfit` multicomponent analysis. The green line shows the Fe II contribution. Dotted green line indicates the expected Fe II contribution for the other parts of the spectra that were not considered in the fitting. The vertical dotted lines indicate the rest-frame of the main emission lines in the $H\beta$ spectral range and the grey-shaded area indicate the regions that were not considered in the fittings and/or are affected by tellurics. The white area indicates the region used to anchor both the continuum and the Fe II template. (b) Result of the fitting after continuum subtraction (upper panel) and the respective residuals (bottom panel) for the $H\beta$ region. Pink dashed line shows the final fit. (c) Continuum-normalised UV spectrum with the adopted continuum marked in different colours depending on the spectral region. (d) Model of the $Si\text{ IV}\lambda 1397 + O\text{ IV}\lambda 1402$. (e) Model of the $C\text{ IV}\lambda 1549 + He\text{ II}\lambda 1640$. (f) Model of the 1900 \AA blend. Broad components (BC) are represented by a black line meanwhile red line shows the VBC. Orange lines represent narrow components and the blue ones correspond to the blueshifted components. The region in which the Fe II or Fe III template was fitted is represented by the solid green lines. Brown lines represent the absorptions seen in the spectrum and were modelled as negative-flux Gaussians.

VBC shift affected by telluric residual.

Appendix A.2: PKS0237-23

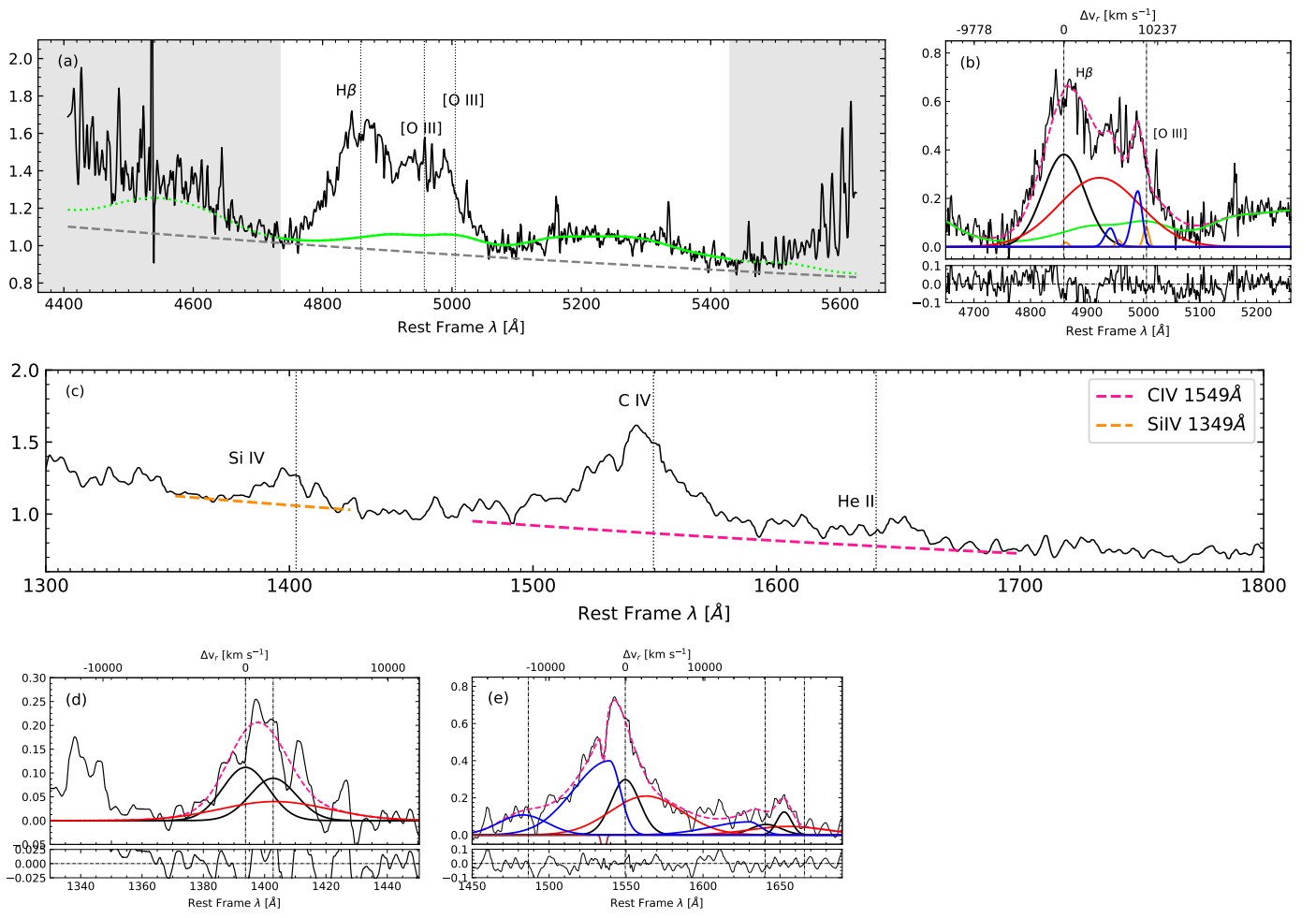


Fig. A.2. PKS0237-23. Colours and lines as Figure A.1.

Appendix A.3: BZQJ0544-2241

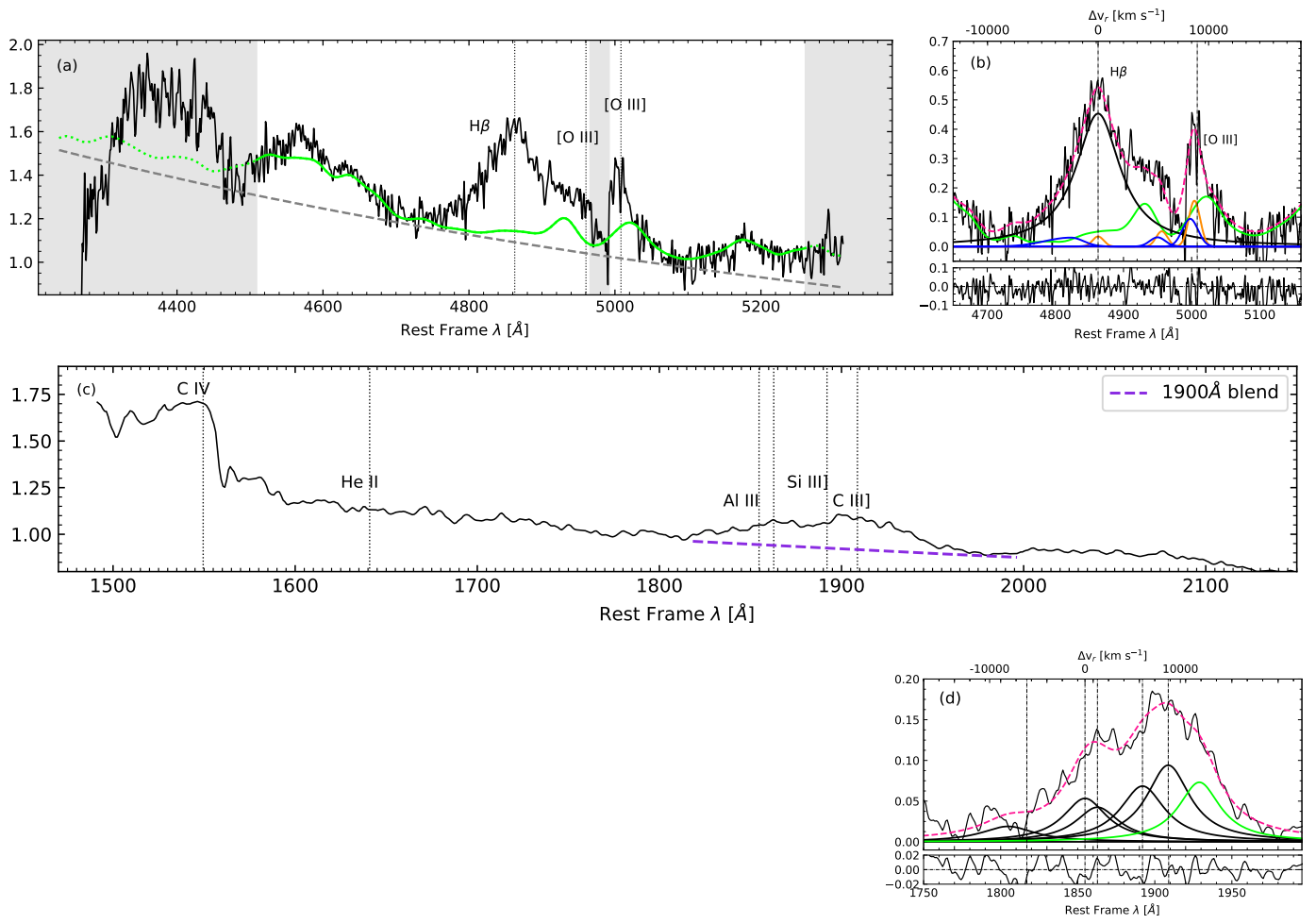


Fig. A.3. BZQJ0544-2241. Colours and lines as Figure A.1.

Appendix A.4: PKS0858-279

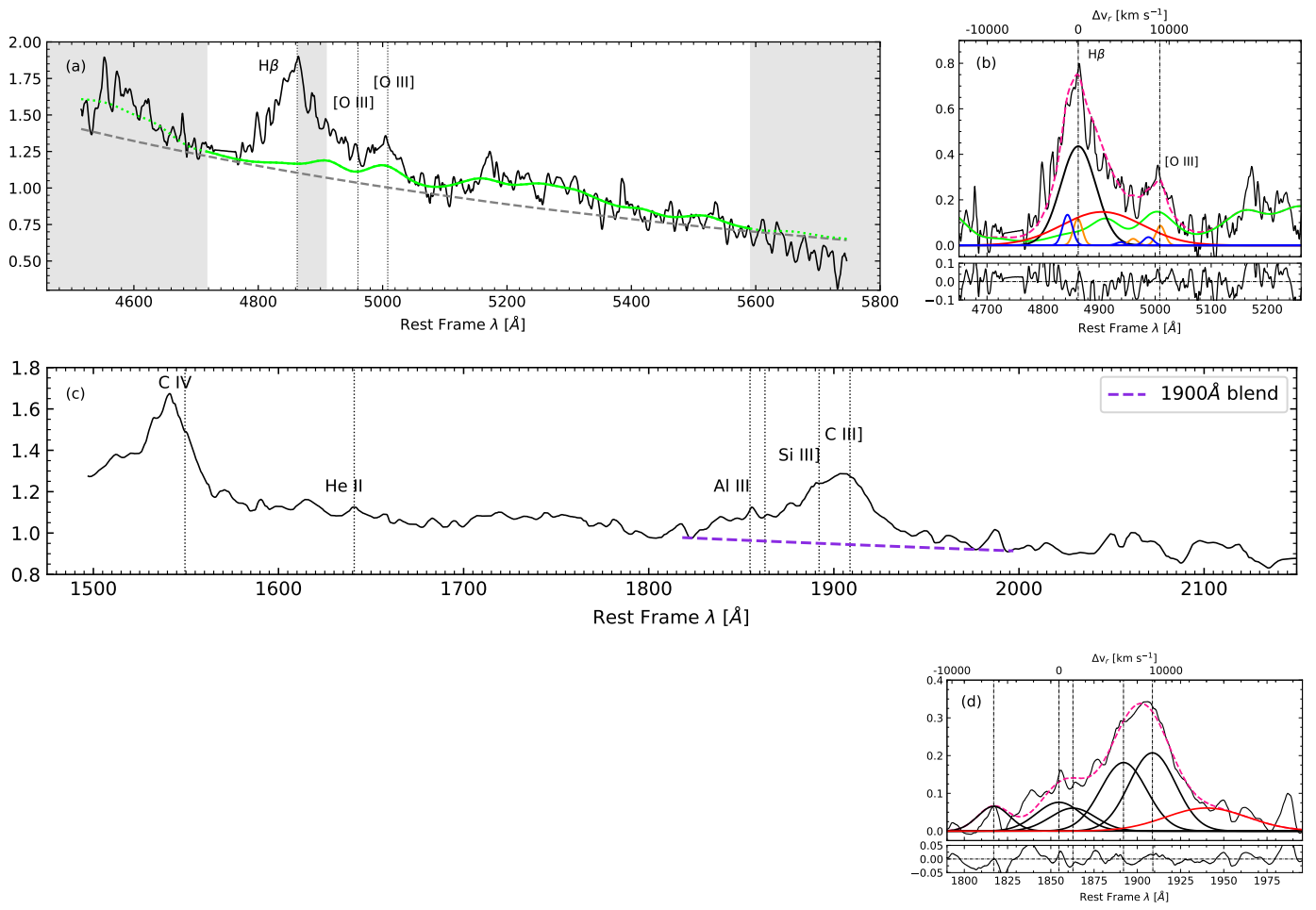


Fig. A.4. PKS0858-279. Colours and lines as Figure A.1.

Appendix A.5: CTSJ01.03

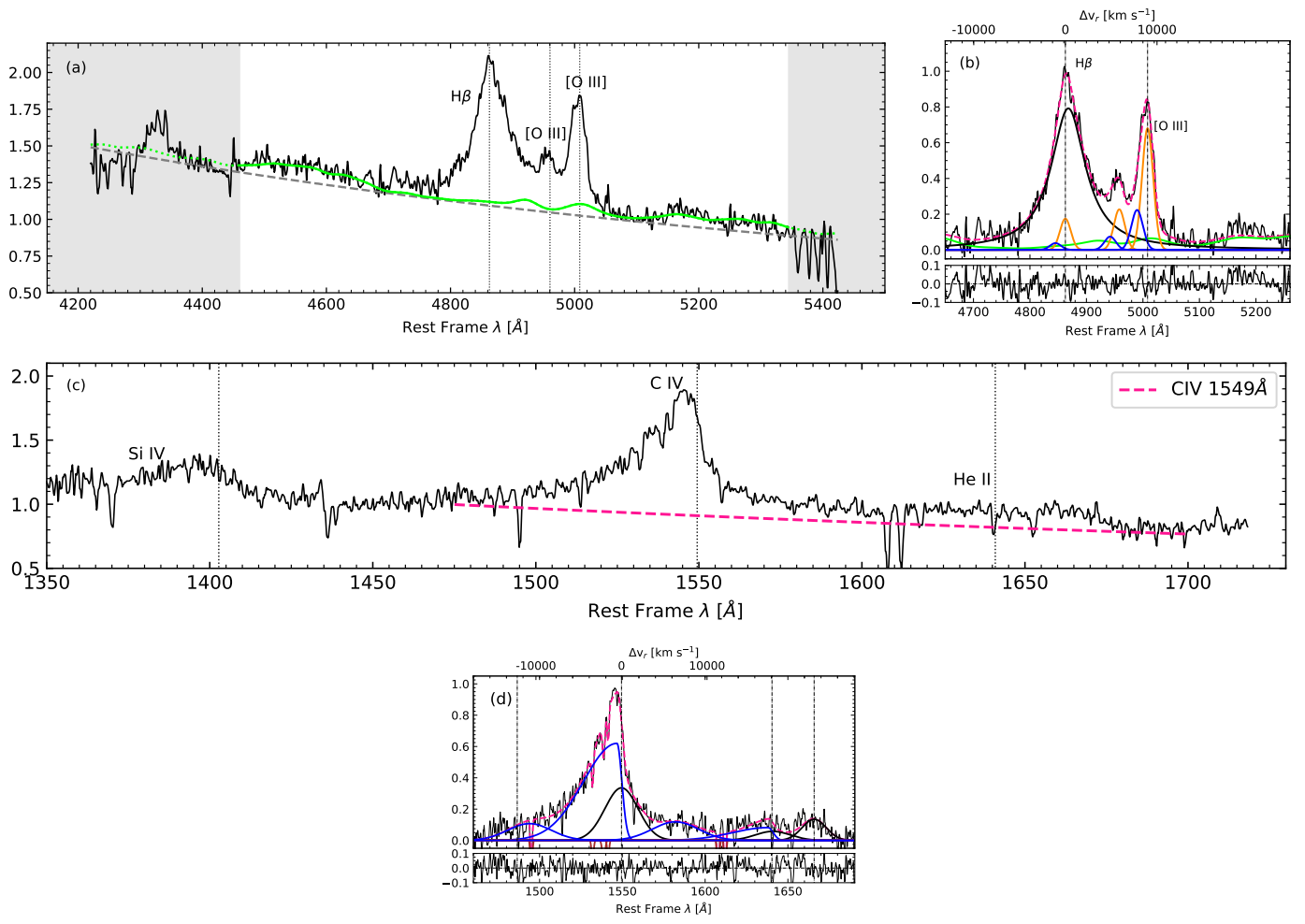


Fig. A.5. CTSJ01.03. Colours and lines as Figure A.1.

Appendix A.6: WB J0948+0855

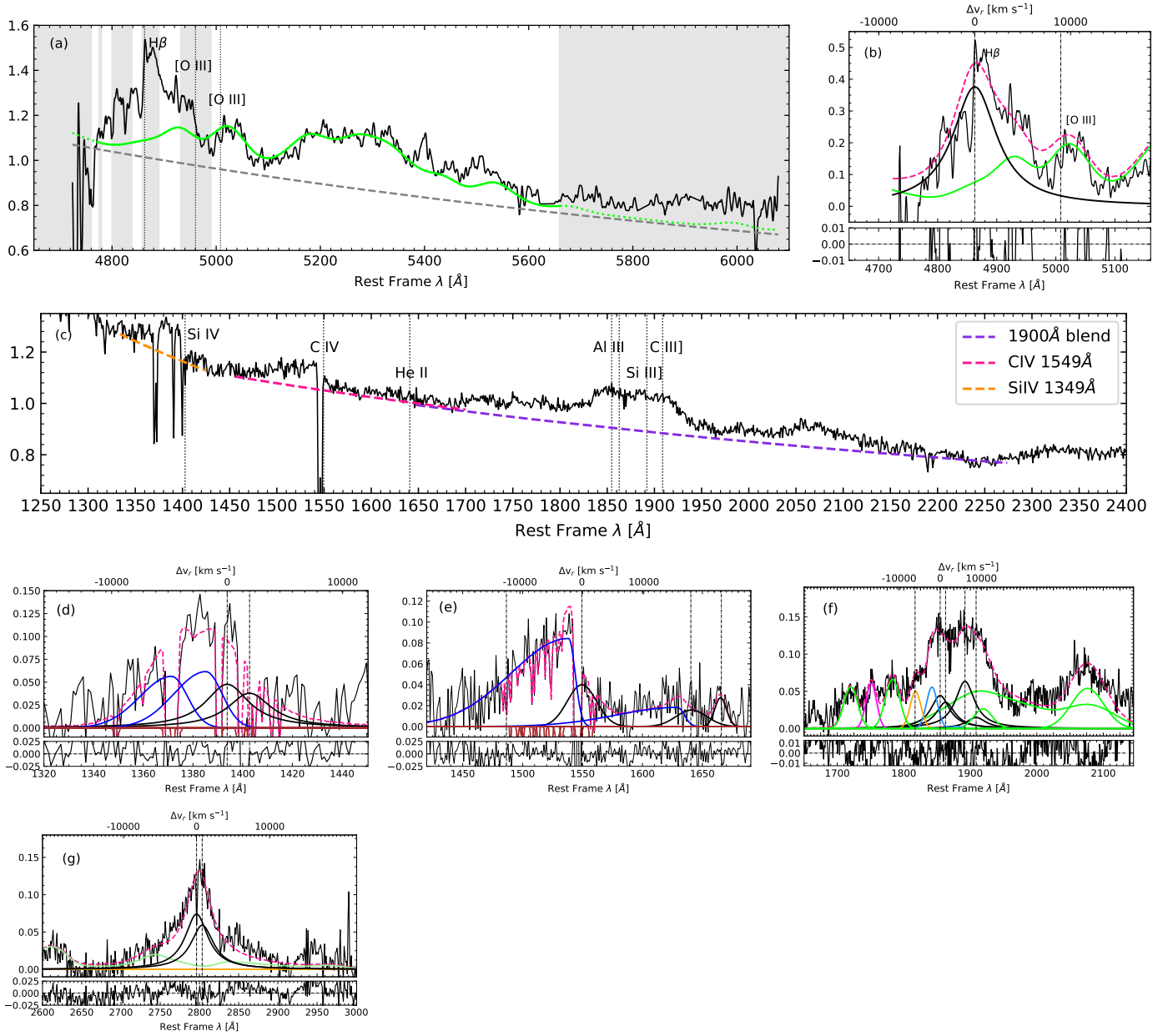


Fig. A.6. WB J0948+0855. Colours and lines as Figure A.1.

An H β BLUE component may be present, however we cannot detect it since the region is located exactly at the border of the spectrum. Due to the difficulty of isolating a narrow component in both H β and [O III] λ 5007 emission lines, the redshift of this source has been estimated based on the Mg II λ 2796,2803 doublet, since this line could be easily identified in the UV spectra (see panel (g) of Fig. A.6).

Appendix A.7: CTSJ03.14

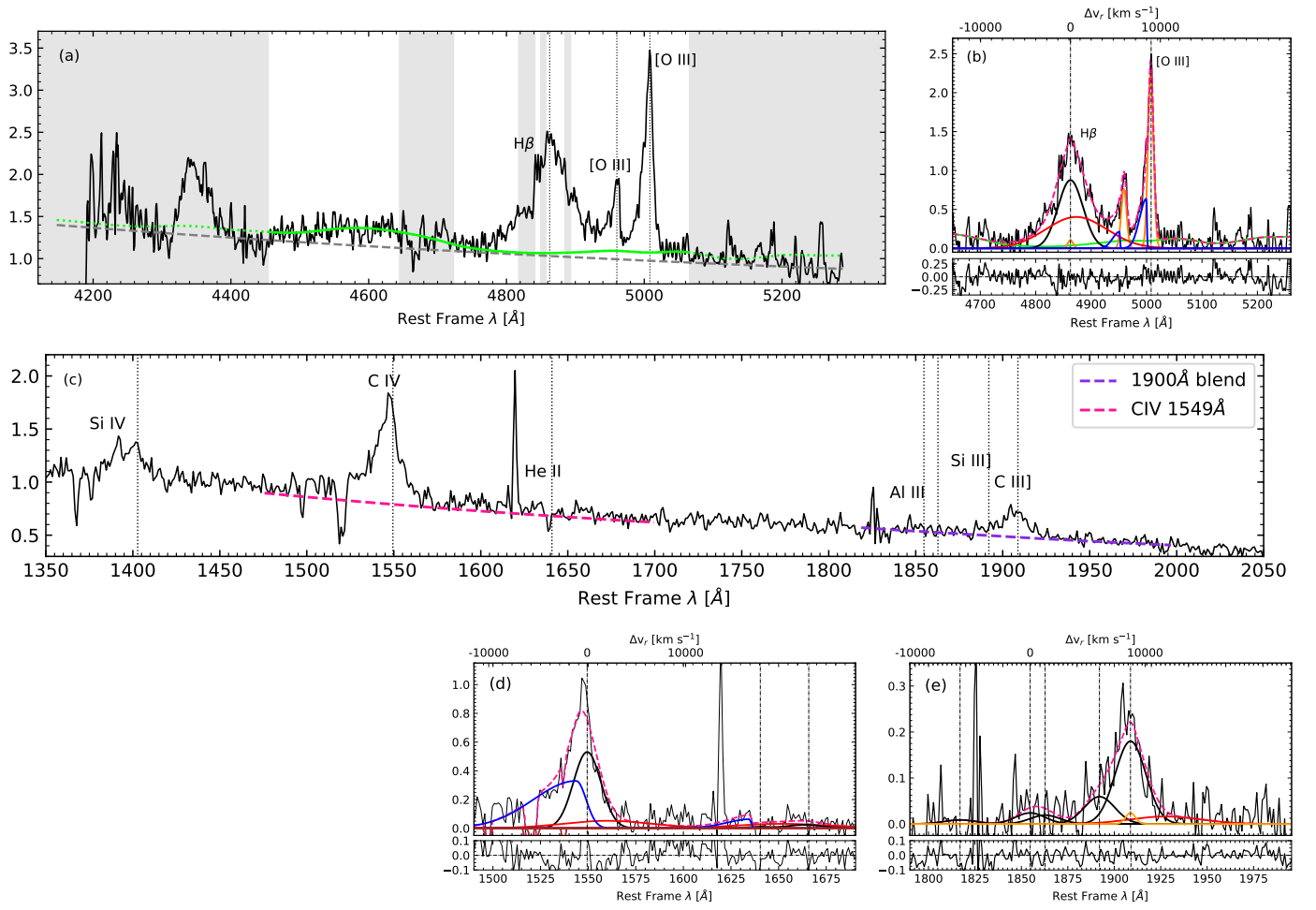


Fig. A.7. CTSJ03.14. Colours and lines as Figure A.1.

Appendix A.8: PKS1448-232

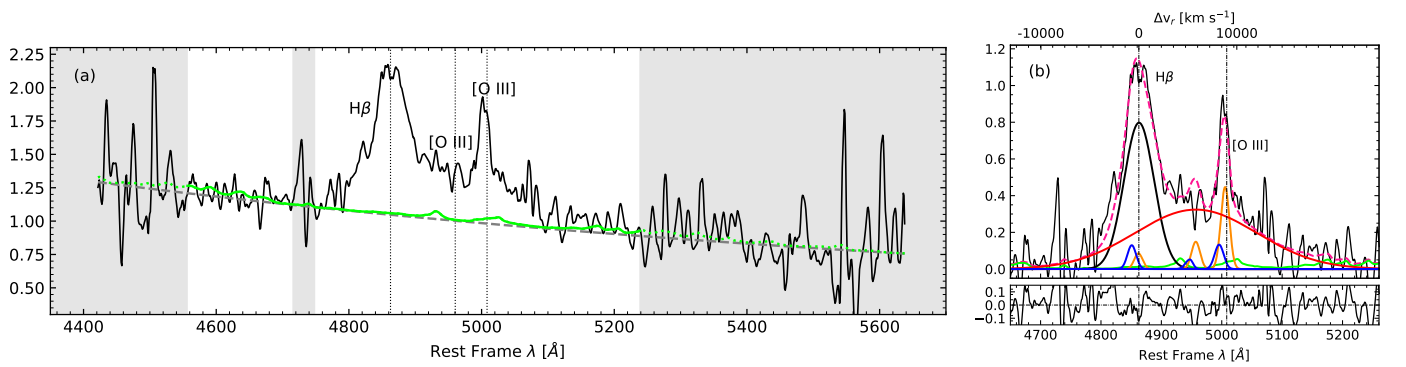


Fig. A.8. PKS1448-232. Colours and lines as Figure A.1.

Appendix A.9: [HB89]1559+088

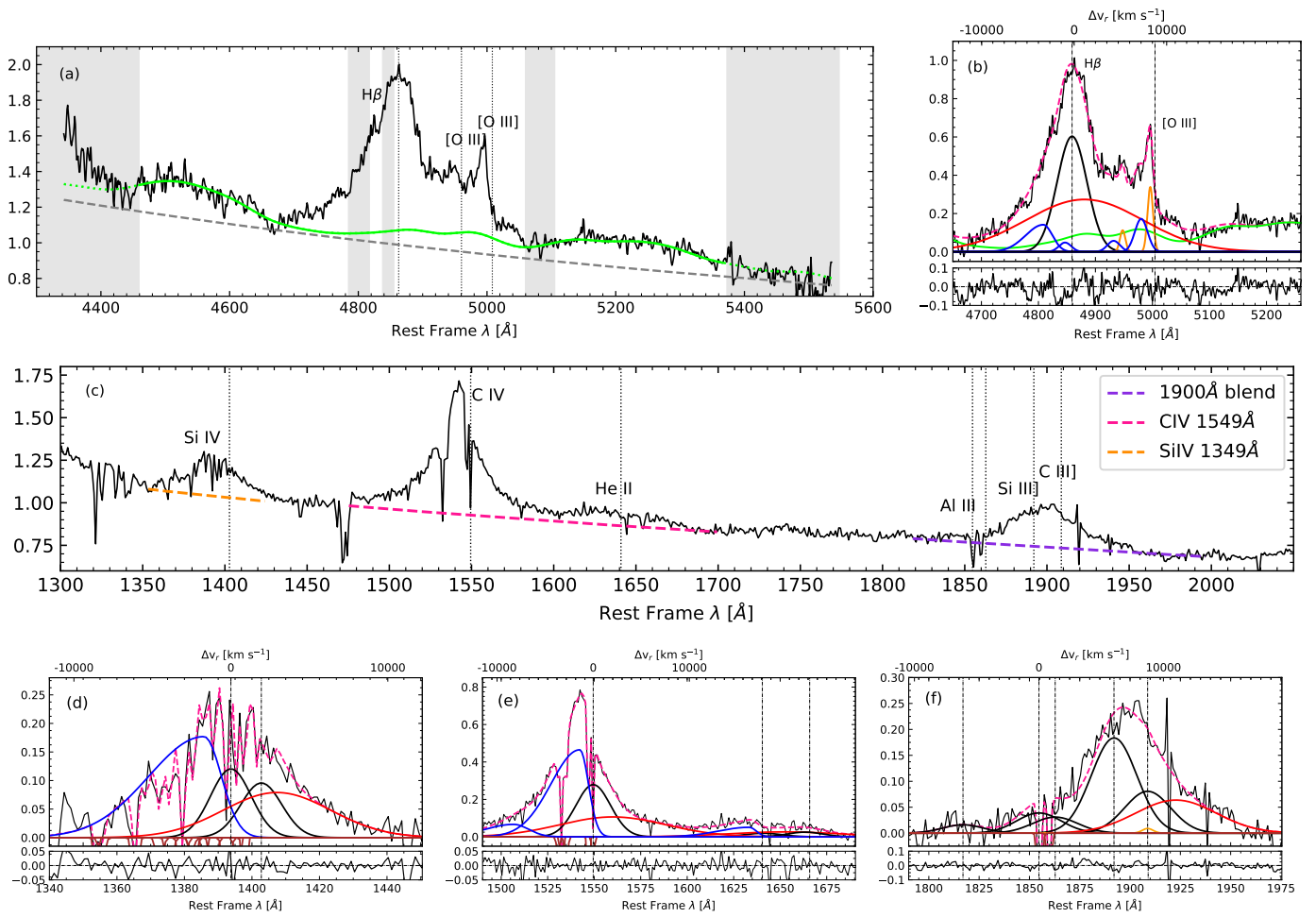


Fig. A.9. [HB89]1559+088. Colours and lines as Figure A.1.

Appendix A.10: FBQS J2149-0811

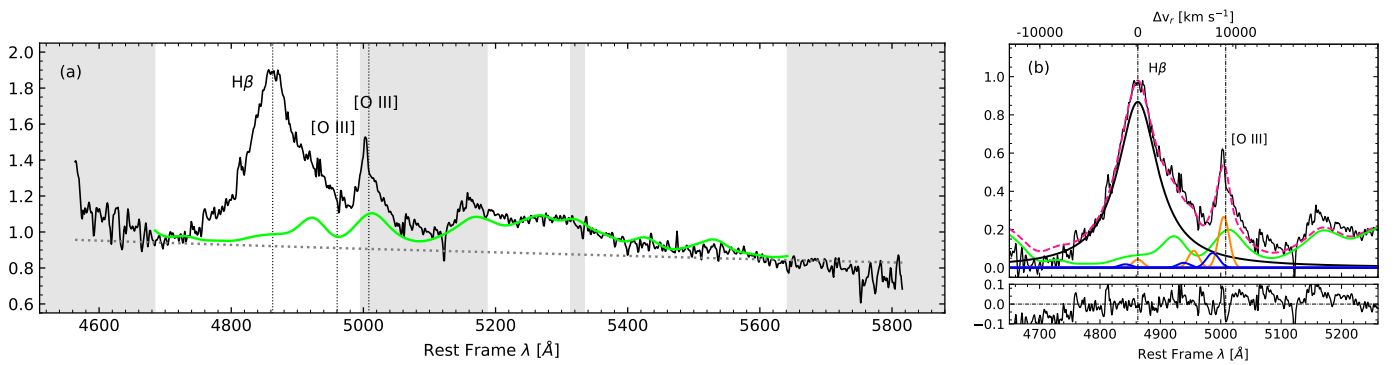


Fig. A.10. FBQS J2149-0811. Colours and lines as Figure A.1.

Appendix B: Radio properties and UV and optical parameters of the samples

Table B.1. Identification of the sources, radio properties, and results of the UV and optical parameters obtained through the re-analysis by multi-component fitting and used in this study for both the HEMS and FOS samples.

Source (1)	RA (2)	DEC (3)	z (4)	$P_{1.4\text{GHz}}$ (5)	$\log(R_K)$ (6)	Radio Class. (7)	[O III]		C IV	
							$c(1/4)$ [km s ⁻¹] (8)	$c(1/2)$ [km s ⁻¹] (9)	$c(1/4)$ [km s ⁻¹] (10)	$c(1/2)$ [km s ⁻¹] (11)
HEMS										
HE 0035-2853	00 38 06.5	-28 36 49	1.638	< 0.08	< 0.31	RQ	-137 ± 405	-33 ± 34	-1080 ± 970	-1530 ± 550
HE 0043-2300	00 45 39.5	-22 43 56	1.540	12.41	2.36	RL	-312 ± 144	-231 ± 55	-1110 ± 720	-980 ± 380
HE 0058-3231	01 00 39.2	-32 14 57	1.582	< 0.07	< 0.35	RQ	-109 ± 47	-109 ± 16	190 ± 1190	-290 ± 400
HE 0109-3518	01 11 43.5	-35 03 01	2.406	< 0.17	< -0.09	RQ	-32 ± 49	-32 ± 15	-1050 ± 530	-820 ± 260
HE 0122-3759	01 24 17.4	-37 44 23	2.200	< 0.14	< 0.23	RQ	-1051 ± 103	-965 ± 600	-4800 ± 540	-3930 ± 870
HE 0203-4627	02 05 52.4	-46 13 30	1.438	15.45	2.07	RL	-318 ± 259	-284 ± 18	-1020 ± 880	-910 ± 460
HE 0205-3756	02 07 27.2	-37 41 57	2.433	4.78	1.51	RQ	-480 ± 210	-480 ± 102	-3320 ± 1080	-2920 ± 330
HE 0248-3628	02 50 55.3	-36 16 35	1.536	0.77	0.83	RQ	-331 ± 286	-36 ± 29	-3950 ± 810	-2790 ± 400
HE 0251-5550	02 52 40.1	-55 38 32	2.351	< 0.43	< 0.23	RQ	-480 ± 220	-440 ± 180	-2170 ± 1860	-1640 ± 320
HE 0349-5249	03 50 59.3	-52 40 35	1.541	< 0.07	< -0.08	RQ	4 ± 109	4 ± 37	-1960 ± 900	-1750 ± 460
HE 0359-3959	04 01 14.0	-39 51 33	1.521	0.24	0.85	RQ	-	-	-5990 ± 610	-5880 ± 490
HE 0436-3709	04 38 37.3	-37 03 41	1.445	< 0.06	< 0.37	RQ	-114 ± 144	-114 ± 50	-1680 ± 1070	-1880 ± 580
HE 0507-3236	05 09 17.8	-32 32 45	1.577	< 0.07	< 0.18	RQ	-540 ± 175	-268 ± 65	-3100 ± 970	-1670 ± 430
HE 0512-3329	05 14 10.8	-33 26 23	1.587	< 0.07	< 0.06	RQ	-964 ± 151	-436 ± 73	-2960 ± 920	-2470 ± 340
HE 0926-0201	09 29 13.5	-02 14 47	1.682	< 0.01	< -0.82	RQ	-581 ± 146	-403 ± 99	-3280 ± 1030	-2280 ± 410
HE 0940-1050	09 42 53.5	-11 04 27	3.093	< 0.28	< 0.45	RQ	-1432 ± 121	-1378 ± 50	-3290 ± 660	-2800 ± 600
HE 1039-0724	10 42 19.3	-07 40 37	1.458	< 0.02	< 0.15	RQ	-592 ± 206	-199 ± 66	-490 ± 1250	-700 ± 740
HE 1104-1805	11 06 33.5	-18 21 25	2.319	< 0.16	< 0.17	RQ	-60 ± 20	-40 ± 18	-1630 ± 830	-1500 ± 370
HE 1120+0154	11 23 20.7	01 37 48	1.472	< 0.02	< -0.53	RQ	-147 ± 145	-60 ± 34	-1110 ± 1730	-670 ± 420
HE 1347-2457	13 50 38.8	-25 12 16	2.599	< 0.20	< 0.19	RQ	-	-	-5850 ± 660	-5490 ± 440
HE 1349+0007	13 51 50.5	00 07 39	1.444	< 0.02	< -0.11	RQ	-589 ± 303	-262 ± 36	-4090 ± 840	-3040 ± 460
HE 1409+0101	14 12 21.7	00 47 19	1.650	0.43	0.65	RQ	-806 ± 154	-731 ± 67	-2900 ± 1040	-2790 ± 420
HE 2147-3212	21 50 52.3	-31 58 26	1.543	< 0.07	< 0.33	RQ	-844 ± 189	-96 ± 65	-4440 ± 1090	-3110 ± 620
HE 2156-4020	21 59 54.7	-40 05 50	2.543	< 0.19	< 0.36	RQ	-768 ± 84	-724 ± 36	-1870 ± 900	-1850 ± 370
HE 2202-2557	22 05 29.8	-25 42 23	1.535	4.24	2.13	RL	-518 ± 110	-339 ± 126	-1280 ± 1000	-2080 ± 420
HE 2349-3800	23 52 10.7	-37 43 22	1.604	4.66	2.07	RL	-653 ± 116	-647 ± 45	-2810 ± 1120	-2070 ± 490
HE 2352-4010	23 55 34.5	-39 53 54	1.580	< 0.07	< 0.28	RQ	-1544 ± 162	-2113 ± 219	-4370 ± 720	-2390 ± 390
HE 2355-4621	23 58 09.2	-46 05 00	2.382	< 0.17	< 0.30	RQ	-151 ± 96	-151 ± 33	190 ± 1360	10 ± 350
FOS										
ICRF J000559.2+160949	00 05 59.2	+16 09 49	0.450	4.71	2.99	RL	11 ± 34	11 ± 12	254 ± 789	138 ± 157
Mrk 335	00 06 19.5	+20 12 10	0.025	10 ⁻⁴	0.31	RQ	69 ± 46	67 ± 16	-313 ± 468	-31 ± 87
LEDA 1790	00 29 13.7	+13 16 03	0.145	10 ⁻³	0.67	RQ	2 ± 31	1 ± 10	-1253 ± 1573	-69 ± 181
PG 0044+030	00 47 05.9	+03 19 54	0.623	0.09	1.12	RQ	-241 ± 78	-141 ± 53	-1054 ± 812	-729 ± 227
Mrk 1502	00 53 34.9	+12 41 35	0.061	10 ⁻⁴	0.33	RQ	-1311 ± 167	-857 ± 158	-2286 ± 398	-1458 ± 552
LBQS 0100+0205	01 03 12.9	+02 21 09	0.394	< 0.01	< 0.71	RQ	-62 ± 58	-61 ± 20	12 ± 744	-102 ± 165
3C 057	02 01 57.1	-11 32 33	0.671	37.92	4.31	RL	-496 ± 98	-341 ± 84	-943 ± 599	-1007 ± 185
3C 84	03 19 48.1	+41 30 42	0.018	0.17	3.65	RL	-119 ± 35	-120 ± 12	-122 ± 25	-190 ± 78
[HB89] 0403-132	04 05 34.0	-13 08 13	0.571	41.00	4.28	RL	-3 ± 38	-3 ± 13	455 ± 1171	239 ± 111
LEDA 75249	04 52 30.0	-29 53 35	0.286	0.02	1.27	RQ	-76 ± 53	-62 ± 18	-1501 ± 463	-1021 ± 233
Mrk 1095	05 16 11.4	-00 08 59	0.032	10 ⁻⁴	0.46	RQ	65 ± 40	65 ± 13	-566 ± 213	-236 ± 180
ICRF J074541.6+314256	07 45 41.6	+31 42 56	0.461	3.90	2.87	RL	-16 ± 51	5 ± 12	349 ± 1079	-240 ± 182
ICRF J084047.5+131223	08 40 47.5	+13 12 23	0.680	37.05	5.27	RL	-61 ± 86	4 ± 17	459 ± 668	225 ± 131
[HB89] 0850+440	08 53 34.2	+43 49 02	0.515	< 10 ⁻³	< 0.07	RQ	-1073 ± 203	-329 ± 212	-1669 ± 669	-1423 ± 298
LB 9308	09 06 31.8	+16 46 11	0.411	7.66	4.91	RL	204 ± 99	246 ± 18	420 ± 1845	142 ± 187
ICRF J092703.0+390220	09 27 03.0	+39 02 20	0.695	42.84	4.19	RL	-54 ± 46	-55 ± 15	1189 ± 1462	424 ± 138
PG 0947+396	09 50 48.3	+39 26 50	0.207	< 10 ⁻⁴	< 0.13	RQ	-97 ± 89	30 ± 19	2 ± 682	-231 ± 134
PG 0953+414	09 56 52.3	+41 15 22	0.235	< 10 ⁻⁴	< -0.73	RQ	-123 ± 85	-89 ± 25	-207 ± 682	-58 ± 128
Ton 469	09 58 20.9	+32 24 02	0.530	10.34	3.21	RL	65 ± 93	102 ± 28	1566 ± 1669	969 ± 465
SDSS J100402.61+285535.3	10 04 02.6	+28 55 35	0.330	< 10 ⁻³	< -0.01	RQ	-583 ± 97	-585 ± 25	-1725 ± 1034	-1149 ± 152
LEDA 29208	10 04 20.1	+05 13 00	0.161	< 10 ⁻⁴	< -0.09	RQ	-187 ± 75	-176 ± 23	-592 ± 726	-226 ± 144
FBQS J101027.5+413238	10 10 27.5	+41 32 39	0.613	5.64	3.24	RL	53 ± 98	47 ± 18	-213 ± 1008	-33 ± 198
NGC 3227	10 23 30.5	+19 51 54	0.004	10 ⁻⁵	1.27	RQ	40 ± 56	30 ± 17	-155 ± 89	-195 ± 105
7C 1028+3118	10 30 59.0	+31 02 55	0.178	0.19	2.73	RL	90 ± 33	85 ± 8	-321 ± 1078	35 ± 201
PG 1049-005	10 51 51.4	-00 51 17	0.359	< 10 ⁻³	< -0.13	RQ	-79 ± 84	-42 ± 18	-102 ± 793	-152 ± 131
2MASX J10523275+6125211	10 52 32.7	+61 25 20	0.421	5.01	3.67	RL	101 ± 37	101 ± 12	1143 ± 1574	149 ± 182
PG 1100+772	11 04 13.8	+76 58 58	0.312	6.25	3.26	RL	-54 ± 53	-46 ± 17	37 ± 1144	38 ± 286

Table B.1. Identification of the sources, radio properties, and results of the UV and optical parameters obtained through the re-analysis by multi-component fitting and used in this study for both the HEMS and FOS samples. (cont.)

Source	RA	DEC	z	$P_{1.4\text{GHz}}$	$\log(R_K)$	Radio Class.	[O III]		C IV	
							$c(1/4)$ [km s ⁻¹]	$c(1/2)$ [km s ⁻¹]	$c(1/4)$ [km s ⁻¹]	$c(1/2)$ [km s ⁻¹]
(1)	(2)	(3)	(4)	(5)	(6)	(7)	(8)	(9)	(10)	(11)
NGC 3516	11 06 47.4	+72 34 07	0.009	10 ⁻⁵	1.31	RQ	-58 ± 36	-42 ± 11	-861 ± 617	68 ± 43
ICRF J110715.0+162802	11 07 15.0	+16 28 02	0.632	10.51	3.60	RL	110 ± 50	101 ± 10	614 ± 755	323 ± 163
3C 254	11 14 38.7	+40 37 20	0.737	52.56	4.49	RL	211 ± 207	266 ± 17	1282 ± 1349	509 ± 116
PG 1114+445	11 17 06.3	+44 13 33	0.143	< 10 ⁻⁴	< -0.34	RQ	-61 ± 57	-35 ± 20	343 ± 734	145 ± 100
LEDA 34570	11 18 30.2	+40 25 54	0.154	10 ⁻³	0.60	RQ	-171 ± 47	-170 ± 16	-784 ± 710	-241 ± 150
PG 1116+215	11 19 08.6	+21 19 17	0.177	10 ⁻³	0.42	RQ	-280 ± 155	-106 ± 49	-1238 ± 722	-848 ± 235
2MASS J11243917+4201450	11 24 39.1	+42 01 45	0.225	< 10 ⁻⁴	< -0.09	RQ	67 ± 50	69 ± 16	-44 ± 389	-30 ± 76
LBQS 1138+0204	11 41 21.7	+01 48 03	0.382	< 10 ⁻³	< 0.09	RQ	15 ± 27	23 ± 9	-1076 ± 936	-871 ± 248
LBQS 1144-0115	11 47 18.0	-01 32 07	0.383	< 10 ⁻³	< -0.03	RQ	-455 ± 55**	-377 ± 30**	189 ± 983	267 ± 158
LB 2136	11 53 24.4	+49 31 08	0.334	4.86	4.04	RL	-29 ± 31	-21 ± 12	884 ± 777	416 ± 130
LEDA 38224	12 04 42.1	+27 54 11	0.165	< 10 ⁻⁴	< -0.16	RQ	-42 ± 74	-11 ± 16	-637 ± 937	-174 ± 111
PB 3894	12 14 17.6	+14 03 13	0.081	10 ⁻⁴	0.46	RQ	-45 ± 37	-38 ± 13	-198 ± 441	-138 ± 86
NGC 4253	12 18 26.5	+29 48 46	0.012	10 ⁻⁴	1.28	RQ	32 ± 31	32 ± 11	-91 ± 385	-89 ± 76
PG 1216+069	12 19 20.9	+06 38 38	0.332	10 ⁻³	0.25	RQ	10 ± 35	10 ± 12	-761 ± 1458	137 ± 158
3C 273	12 29 06.6	+02 03 08	0.158	23.86	3.45	RL	-312 ± 280	-268 ± 62	-618 ± 951	-549 ± 107
SBS 1250+568	12 52 26.3	+56 34 19	0.320	6.47	4.42	RL	110 ± 39	110 ± 13	133 ± 799	-60 ± 110
SBS 1259+593	13 01 12.9	+59 02 06	0.478	< 10 ⁻³	< -0.35	RQ	-102 ± 482	-81 ± 36	-3034 ± 597	-2681 ± 239
ICRF J130533.0-103319	13 05 33.0	-10 33 19	0.278	1.50	2.71	RL	-261 ± 91	-143 ± 69	619 ± 1585	9 ± 127
LEDA 45656	13 09 47.0	+08 19 48	0.155	< 10 ⁻⁴	< -0.33	RQ	-73 ± 67	-23 ± 18	103 ± 1049	117 ± 147
FBQS J131217.7+351521	13 12 17.7	+35 15 21	0.182	0.04	1.56	RQ	-128 ± 135	-33 ± 31	-1099 ± 1392	190 ± 464
2XMM J135315.8+634546	13 53 15.8	+63 45 45	0.088	10 ⁻³	1.22	RQ	-159 ± 98	-79 ± 24	195 ± 761	152 ± 107
PB 4142	13 54 35.6	+18 05 17	0.151	< 10 ⁻⁴	< -0.15	RQ	-227 ± 66	-122 ± 54	-376 ± 972	-101 ± 174
[HB89] 1354+195	13 57 04.4	+19 19 07	0.720	41.34	3.87	RL	-53 ± 41	-53 ± 14	731 ± 1199	13 ± 153
FBQS J1405+2555	14 05 16.2	+25 55 34	0.163	10 ⁻⁴	0.12	RQ	-179 ± 118	-195 ± 39	-853 ± 730	-454 ± 250
LEDA 50313	14 06 21.8	+22 23 46	0.097	10 ⁻⁴	0.42	RQ	-339 ± 84	-248 ± 35	-1571 ± 876 [†]	-1537 ± 875 [†]
[HB89] 1415+451	14 17 00.8	+44 56 06	0.115	10 ⁻⁴	0.36	RQ	-593 ± 40	-593 ± 13	-1103 ± 436	-974 ± 144
NGC 5548	14 17 59.5	+25 08 12	0.017	10 ⁻⁴	0.88	RQ	-15 ± 44	-2 ± 14	199 ± 993	274 ± 170
Mrk 813	14 27 25.0	+19 49 52	0.111	10 ⁻⁴	0.39	RQ	187 ± 70	176 ± 20	-161 ± 1561	-180 ± 411
[HB89] 1425+267	14 27 35.6	+26 32 14	0.363	0.40	2.40	RL	-244 ± 76	32 ± 30	-964 ± 1275	-908 ± 298
2MASS J14294306+4747262	14 29 43.0	+47 47 26	0.220	< 10 ⁻⁴	0.29	RQ	-160 ± 200	-143 ± 150	175 ± 511	175 ± 103
Mrk 478	14 42 07.4	+35 26 22	0.077	10 ⁻⁴	0.33	RQ	-15 ± 53	-10 ± 20	-955 ± 494	-755 ± 142
[HB89] 1444+407	14 46 45.9	+40 35 05	0.267	< 10 ⁻⁴	< -0.32	RQ	-169 ± 50	-174 ± 15	-1411 ± 670	-1284 ± 207
ICRF J145427.4-374733	14 54 27.4	-37 47 33	0.314	2.56	3.59	RL	21 ± 41	24 ± 13	1172 ± 814	698 ± 110
ICRF J151443.0+365050	15 14 43.0	+36 50 50	0.371	3.83	3.29	RL	99 ± 74	120 ± 11	-198 ± 891	-48 ± 271
[HB89] 1538+477	15 39 34.8	+47 35 31	0.772	0.17	1.26	RQ	-124 ± 52	-111 ± 17	-1338 ± 1231	-546 ± 306
[HB89] 1543+489	15 45 30.2	+48 46 08	0.398	0.01	0.70	RQ	-1985 ± 170	-1777 ± 88	-2287 ± 569	-1911 ± 228
ICRF J154743.5+205216	15 47 43.5	+20 52 16	0.266	0.91	2.88	RL	41 ± 56	37 ± 16	352 ± 1400	-114 ± 183
Mrk 493	15 59 09.6	+35 01 47	0.031	10 ⁻⁴	0.84	RQ	-21 ± 28	-22 ± 9	53 ± 313	51 ± 62
Ton 256	16 14 13.2	+26 04 16	0.131	10 ⁻³	1.29	RQ	-30 ± 40	-19 ± 13	1395 ± 1244	304 ± 111
3C 334	16 20 21.8	+17 36 23	0.556	2.18	2.88	RL	-31 ± 73	3 ± 21	109 ± 1402	-77 ± 374
SBS 1626+554	16 27 56.1	+55 22 31	0.133	< 10 ⁻⁴	< -0.39	RQ	-29 ± 62	-29 ± 24	10 ± 957	-208 ± 147
FBQS J163020.7+375656	16 30 20.7	+37 56 56	0.395	0.10	1.62	RQ	6 ± 76	70 ± 19	1573 ± 713	1174 ± 190
3C 345	16 42 58.8	+39 48 36	0.593	69.71	5.01	RL	16 ± 97	-2 ± 21	389 ± 245	250 ± 213
3C 351.0	17 04 41.3	+60 44 30	0.372	< 10 ⁻³	< 0.34	RQ	-45 ± 53	-27 ± 14	251 ± 1753	120 ± 238
4C 73.18	19 27 48.4	+73 58 01	0.302	9.89	3.79	RL	-4 ± 48	-2 ± 13	320 ± 859	76 ± 144
Mrk 509	20 44 09.7	-10 43 24	0.034	10 ⁻⁴	0.44	RQ	-19 ± 40	-15 ± 13	-820 ± 601	-481 ± 154
PG 2112+059	21 14 52.5	+06 07 42	0.461	0.01	0.27	RQ	307 ± 108	307 ± 37	-1774 ± 584	-1554 ± 209
[HB89] 2128-123	21 31 35.2	-12 07 04	0.500	12.94	3.22	RL	-19 ± 42	-9 ± 10	1019 ± 1392	400 ± 168
4C 31.63	22 03 14.9	+31 45 38	0.295	6.86	3.40	RL	-741 ± 76**	-728 ± 26**	-664 ± 1243	-135 ± 238
UGC 12163	22 42 39.3	+29 43 31	0.025	10 ⁻⁴	1.05	RQ	32 ± 31	32 ± 11	5 ± 323	-61 ± 318
[HB89] 2243-123	22 46 18.2	-12 06 51	0.626	22.28	3.96	RL	-244 ± 64	-221 ± 18	879 ± 1001	212 ± 95
MR 2251-178	22 54 05.8	-17 34 55	0.064	10 ⁻³	0.53	RQ	-23 ± 56	-23 ± 19	-613 ± 1153	-539 ± 189
4C 11.72	22 54 10.4	+11 36 38	0.326	4.21	3.18	RL	106 ± 65	113 ± 19	-312 ± 1513	-206 ± 127
NGC 7469	23 03 15.6	+08 52 26	0.016	10 ⁻³	0.87	RQ	-83 ± 48	-59 ± 12	-93 ± 258	386 ± 59
4C 09.72	23 11 17.7	+10 08 15	0.434	4.21	3.16	RL	-55 ± 114	-17 ± 18	368 ± 1839	114 ± 158
ICRF J234636.8+093045	23 46 36.8	+09 30 45	0.672	24.90	3.61	RL	42 ± 83	120 ± 28	-252 ± 1036	-129 ± 143
[HB89] 2349-014	23 51 56.1	-01 09 13	0.174	1.26	3.50	RL	187 ± 70	176 ± 20	-1585 ± 771	-985 ± 302

Notes. (1) Source identification. (2) Right ascension. (3) Declination. (4) Redshift. (5) Radio power at 1.4 GHz, in units of 10²⁶ W Hz⁻¹. (6) Radioloudness parameter. (7) Radio classification. (8), (9) Velocity centroids at $\frac{1}{4}$ and $\frac{1}{2}$ intensities of the [O III] full profile. (10), (11) Same for the C IV full profile. ** [O III] emission strongly affected by atmospheric lines. [†] C IV emission strongly affected by absorptions.

Appendix C: Details on the estimations of the outflow parameters

Appendix C.1: [O III]λ4959,5007

The expressions for the [O III]λ5007 outflow parameters were derived by [Marziani et al. \(2017\)](#) assuming a bipolar outflow structure (c.f. [Kim et al. 2023](#), and references therein). All the [O III]λ5007 outflow equations reported here are in accordance with the work of [Cano-Díaz et al. \(2012\)](#) and [Fiore et al. \(2017\)](#).

The [O III]λ5007 luminosity can be related to the outflow mass by

$$M_{\text{ion}} = 1 \times 10^7 L_{[\text{OIII}],44}^{\text{out}} \left(\frac{Z}{5Z_{\odot}} \right)^{-1} n_{\text{H},3}^{-1} [\text{M}_{\odot}], \quad (\text{C.1})$$

where $L_{[\text{OIII}],44}^{\text{out}}$ is the outflow-emitted luminosity of [O III]λ5007 emission line in units of $10^{44} \text{ erg s}^{-1}$, the density (n_{H}) and the metallicity (Z) have been scaled to 10^3 cm^{-3} and 5 times solar, respectively.

If we assume that the outflow is confined to a solid angle Ω , then the mass outflow rate $\dot{M}_{\text{ion}}^{\text{out}}$ at a distance r can be written as:

$$\dot{M}_{\text{ion}} = 30 L_{[\text{OIII}],44}^{\text{out}} v_{0,1000} r_{1\text{kpc}}^{-1} \left(\frac{Z}{5Z_{\odot}} \right)^{-1} n_{\text{H},3}^{-1} [\text{M}_{\odot} \text{ yr}^{-1}]. \quad (\text{C.2})$$

Even if part of a nuclear outflow, the [O III]λ4959,5007 emitting gas is probably not being anymore accelerated by radiation pressure, and so we consider as maximum outflow velocity v_0 the centroid at 1/2 intensity of the BLUE component. If we assume the [O III]λ5007 outflow to be nuclear, we can then suppose a super-solar chemical composition $Z = 5Z_{\odot}$ at low redshift, that is also consistent with the metallicity derived for the most metal rich bulge stars. At high redshift, there is no estimation we are aware of the chemical composition of the outflowing gas. A proxy is provided by the metallicity of the stellar component of the host galaxy ([Xu et al. 2018](#)), expected to be twice the solar value.

The thrust might be written as:

$$\dot{M}_{\text{ion}} v_0 = 1.9 \times 10^{35} L_{[\text{OIII}],44}^{\text{out}} v_{0,1000}^2 r_{1\text{kpc}}^{-1} \left(\frac{Z}{5Z_{\odot}} \right)^{-1} n_{\text{H},3}^{-1} [\text{g cm s}^{-2}]. \quad (\text{C.3})$$

Similarly, the kinetic power \dot{E}_{out} is then given by $\dot{E}_{\text{out}} \sim \frac{1}{2} \dot{M}_{\text{out}} v_0^2$, which leads to

$$\dot{\epsilon}_{\text{kin}} = 9.6 \times 10^{42} L_{[\text{OIII}],44}^{\text{out}} v_{0,1000}^3 r_{1\text{kpc}}^{-1} \left(\frac{Z}{5Z_{\odot}} \right)^{-1} n_{\text{H},3}^{-1} [\text{erg s}^{-2}]. \quad (\text{C.4})$$

Appendix C.2: C IVλ1549

Both C IVλ1549 and [O III]λ4959,5007 are predominantly produced by collisional excitation, for which the collisional excitation rate of Eq. 3.20 from [Osterbrock & Ferland \(2006\)](#) applies:

$$q_{12} = \frac{8.629 \cdot 10^{-6} \Upsilon}{T^{\frac{1}{2}} g_1} \exp(-h\nu/kT) [\text{cm}^3 \text{ s}^{-1}] \quad (\text{C.5})$$

where $h\nu$ is the energy of the photon emitted in the transition ($1.28 \times 10^{-11} \text{ erg}$ in the case of C IVλ1549), and k is the Boltzmann's constant in erg K^{-1} . Υ is the collision strength and is almost independent from temperature ([Osterbrock & Ferland \(2006\)](#) yield $\Upsilon \approx 8.91$). The $g_1 = (2J + 1) = 2$, as the lower level of the transition is the ground state ($^2S_{\frac{1}{2}}$). The exponential argument is $h\nu/kT_{10000} \approx 9.28 T_{10000}^{-1}$, and dominates over the factor $T^{-\frac{1}{2}}$.

The mass of ionized gas is given by

$$M_{\text{C}^{+3}} \sim \frac{L_{\text{CIV}}}{(h\nu)_{\text{CIV}} q_{12} n_{\text{H}} [\text{C}/\text{H}] X_{\text{C}^{+3}}} \cdot \mu m_{\text{p}}. \quad (\text{C.6})$$

Here L_{CIV} is the C IVλ1549 luminosity, $(h\nu)_{\text{CIV}}$ the C IVλ1549 photon energy, $[\text{C}/\text{H}]$ the relative abundance of Carbon with respect to Hydrogen, in number: $8.43 \approx 12 + \log [\text{C}/\text{H}]$ for solar abundance, implying $[\text{C}/\text{H}] \approx 2.69 \cdot 10^{-4}$. The factor $X_{\text{C}^{+3}} = [\text{C}^{+3}]/\sum_i [\text{C}^{+i}] \leq 1$ is the ionic fraction of triply ionized Carbon, and μm_{p} is the molecular mass of the gas, with $\mu \approx 1.4$ (neglecting the mass of the metals), and m_{p} the proton mass.

The mass of the emitting gas strongly depends on temperature. A single value of the dynamical temperature could be assumed, in keeping with the simplest assumptions. However, the T value should be chosen carefully.

Appendix C.2.1: Observational constraints

To estimate a typical value of the dynamical temperature, we can apply two main observational constraints on the blueshifted emission due to the outflow:

- C IVλ1549 equivalent width: in super-Eddington candidates, the equivalent width is typically very low $W \sim 10 \text{ \AA}$ and in Population A $W \lesssim 30 \text{ \AA}$ ([Kinney et al. 1990](#); [Sulentic et al. 2000c](#); [Marziani et al. 2016b](#); [Martínez-Aldama et al. 2018](#)). The sources that are radiating at high Eddington ratio are the ones showing the lowest W along the E1 main sequence, with a large fraction of them being weak lined quasars (WLQs) ([Shemmer et al. 2010](#); [Wu et al. 2012](#); [Marziani et al. 2016b](#); [Martínez-Aldama et al. 2018](#); [Jin et al. 2023](#)). Even for the Pop. B sources of the HEMS and ISAAC samples $W_{\text{CIV}\lambda 1549}$ is usually below $\approx 50 \text{ \AA}$.
- C IVλ1549/Hβ ratio: its value, due to the absence of a strong Hβ blueshifted component, can be assumed to be $\text{C IV}\lambda 1549/\text{H}\beta \gtrsim 5 \sim 10$ for blueshifted components.

The decomposition of the C IVλ1549 profile in two components reveals very different properties and physical conditions for the outflow and virial component. In the outflow case, the C IVλ1549 equivalent width is in the range from the detectability limit of a few \AA to a few tens \AA . This observational constraint suggests that the outflow component of the C IVλ1549 profile is not produced by gas in physical conditions optimized for its emission.

Appendix C.2.2: Photoionization modeling

The diagrams of Fig. C.1 show the W of C IVλ1549 (left panels) and the C IV/Hβ ratio (right panels) as a function of the ionization parameter U , according to CLOUDY 17.02 ([Ferland et al. 2017](#)) computations, assuming two cases: (1) $M_{\text{BH}} = 10^9 \text{ M}_{\odot}$, five times solar metallicity, and a standard AGN SED representative for low-redshift sources that have Eddington ratios $\gtrsim 0.1 - 0.2$ ([Mathews & Ferland 1987](#)) (upper panels); and (2) in bottom panels for $M_{\text{BH}} = 10^{9.5} \text{ M}_{\odot}$, five times solar metallicity and the SED defined by [Krawczyk et al. \(2013\)](#), more appropriate for representing our high- z high luminosity sources (see more details below). Very low W is possible in conditions of Carbon under-ionization and over-ionization with respect to C^{+3} . For the blueshifted component, a high-ionization solution has been found with typical values $\log U \sim -0.5 - 0$ ([Śniegowska et al. 2021](#); [Garnica et al. 2022](#)).

The upper left panel of Fig. C.1 shows that the expected $W(\text{C IV}\lambda 1549)$ at $U \sim 1$ is several tens of \AA , consistent with the observations if the covering factor is moderate ($\sim 0.2 - 0.5$), with a marginal dependence on density. The C IVλ1549/Hβ ratio is constrained to be $\gtrsim 5$, with C IVλ1549/Hβ ~ 10 for the density range $10^{9.5} - 10^{10} \text{ cm}^{-3}$.

The electron temperature associated with these conditions is high ($T \sim 20000 \text{ K}$), implying a very high efficiency for the collisional excitation. The point here is that, even if the collisional efficiency is high, the ionic fraction of C^{+3} is very low (~ 0.01), yielding a $\tilde{q}X$ factor $\approx (3 - 4) \cdot 10^{-11} \text{ cm}^3 \text{ s}^{-1}$.

At high luminosity, however, the softening of the accretion disk emission due to large masses makes the SED significantly different from that of [Mathews & Ferland \(1987\)](#). The peak of the disk emission can be displaced toward lower frequency by a factor ~ 10 ([Duras](#)

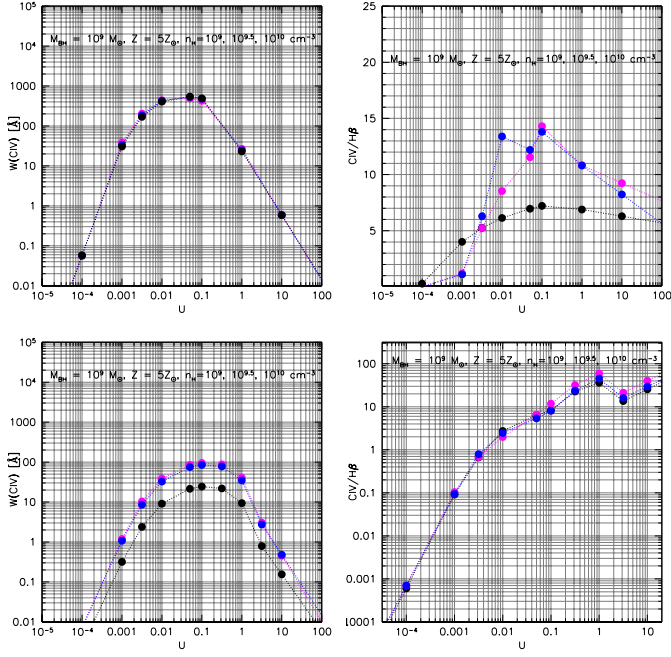


Fig. C.1. Relation between $W(\text{C IV}\lambda 1549)$ (left panels) and intensity ratio $\text{C IV}\lambda 1549/\text{H}\beta$ (right panels) with the ionization parameter U for three density values $\log n_{\text{H}} = 9, 9.5, 10$ [cm^{-3}] (black, blue, and magenta symbols, respectively), column density $N_{\text{c}} = 10^{22} \text{ cm}^{-2}$, 5 times solar metallicity. Top: For $\log M_{\text{BH}} = 10^9 [M_{\odot}]$, and a Mathews & Ferland (1987) SED. Bottom: $\log M_{\text{BH}} = 10^{9.5} [M_{\odot}]$, and a Krawczyk et al. (2013) SED.

et al. 2017, 2020), reducing significantly the amount of ionizing photons. We therefore considered a different SED, defined for intermediate redshift quasars with $W(\text{C IV}) \lesssim 30 \text{ \AA}$ (Krawczyk et al. 2013). The simulations predict lower $W(\text{C IV})$ by a factor ≈ 5 (bottom panels on Fig. C.1) with respect to the Mathews & Ferland (1987) SED. The $W(\text{C IV})$ and the $\text{C IV}/\text{H}\beta$ ratio provide some constraints over the ionization parameter and density. The $\text{C IV}/\text{H}\beta$ ratio falls within a range of $\sim 8 - 33$ for the ISAAC sources where the BLUE of $\text{H}\beta$ has been detected, and the $W \sim 10 \text{ \AA}$. For $\log n_{\text{H}} \approx 9.5$, these conditions imply a $\log U$ between -0.7 and 0.3 . In this case, for $\log U \approx -0.2$, and computing a weighted average over r^2 , we obtain a much higher efficiency, $\overline{Xq(T)}$ to $\approx 1.22 \cdot 10^{-10} \text{ cm}^3 \text{ s}^{-1}$. Much lower efficiencies are possible if $\log U \rightarrow 0$ and $\log n_{\text{H}} \rightarrow 9$. In this case the predicted $W(\text{C IV})$ might be below 10 \AA , as found for weak lined quasars (Diamond-Stanic et al. 2009; Shemmer et al. 2010; Marziani et al. 2016a).

Fig. C.2 shows the trends expected for the ionization parameter and electron temperature as a function of radius, for the value of the density $\log n_{\text{H}} = 9.5 [\text{cm}^{-3}]$. The intercepts between the expected range of ionization parameter and radius does not fall in correspondence of the peak ionization fraction in the case of the Mathews & Ferland (1987) SED, while it does in the high-luminosity case due to the “softer” Krawczyk et al. (2013) SED (bottom panels of Fig. C.2). The lower limit assumed for $\log U \approx -0.5$ implies a condition of over-ionization for the line emitting gas. Electron temperature is around $T_{\text{e}} \approx 20000 \text{ K}$.

The photoionization computations predict an equivalent width more than an order of magnitude higher than the observed value if $\text{C IV}\lambda 1549$ emission is due to gas at $\log U \sim -1.3$ in the case of the Mathews & Ferland (1987) SED appropriate for low- z sources (upper right panel of Fig. C.1). In addition, the distance expected for $\log U = -1.3$ and $\log n_{\text{H}} \approx 9.0$ is $\log r \approx 18.8 [\text{cm}]$, more than one order of magnitude higher than the scaling radius of Kaspi et al. (2021), $\log r \approx 17.43 [\text{cm}]$ (see the ionic fraction distribution in the lower half of the upper panel of Fig. C.2).

Taking into account previous considerations, we use for the ionized mass the following expression:

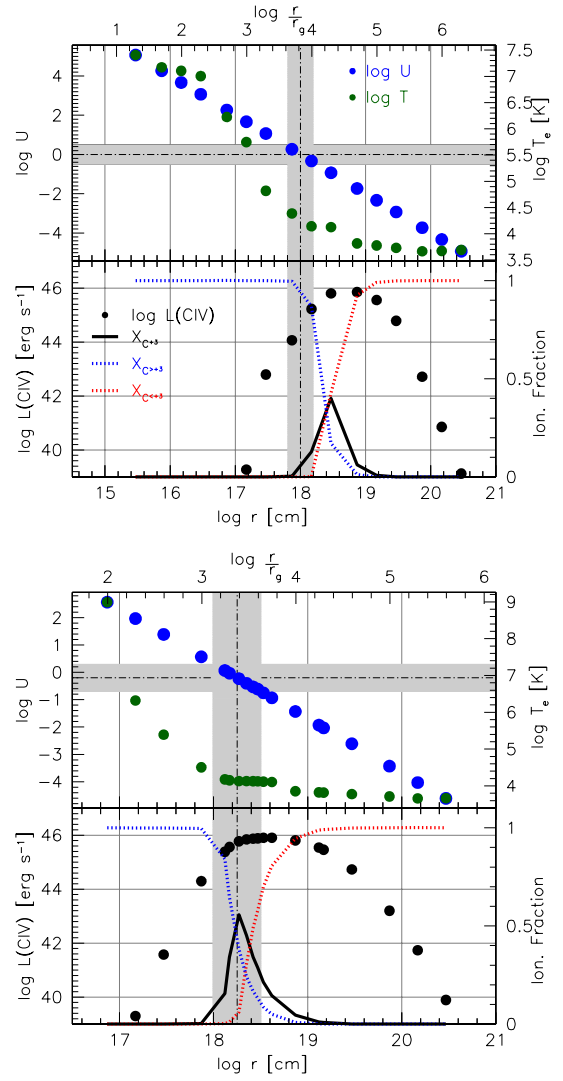


Fig. C.2. Behavior of ionization parameter, electron temperature, $\text{C IV}\lambda 1549$ luminosity, and ionic fraction as a function of radius for density value $\log n_{\text{H}} = 9.5 [\text{cm}^{-3}]$, and for the two adopted SEDs for the low (top panels) and high- z (bottom panels) samples. *Top, upper panel:* behavior of the ionization parameter (left axis scale, blue dots) and electron temperature (right axis scale, green dots) as a function of radius for a $M_{\text{BH}} = 10^9 M_{\odot}$ radiating at Eddington limit and illuminating a slab of gas. We assume column density $N_{\text{c}} = 10^{22} \text{ cm}^{-2}$, Mathews & Ferland (1987) SED, and the metallicity five times solar in all cases. *Top, lower panel:* logarithm of $\text{C IV}\lambda 1549$ luminosity (black dots) and ionic fraction as a function of radius. The blue and red line represent the ionic stages higher and lower than 3, respectively, and the black circles ionic stage 3. *Bottom, upper and lower panels:* same as top panels, for $\log M_{\text{BH}} = 9.5 [M_{\odot}]$, and SED from Krawczyk et al. (2013). In both the top and bottom panels, the horizontal grey bands indicate the range of ionization parameters consistent with the observed C IV equivalent width and the $\text{C IV}/\text{H}\beta$ ratio. The vertical bands represent the corresponding range of permitted radii.

$$M_{\text{ion}} \approx 6.5 \cdot 10^2 L_{\text{CIV},45}^{\text{out}} \left[\frac{Z}{5Z_{\odot}} \right]^{-1} n_{\text{H},9.5}^{-1} [M_{\odot}] \quad (\text{C.7})$$

which incorporates the average over density in the range $10^{9.5} - 10^{10.5} \text{ cm}^{-3}$ of $Xq(T)$ for $\log U = 0$, $\overline{Xq(T)} \approx 3.3 \cdot 10^{-11} \text{ cm}^3 \text{ s}^{-1}$. Averaging over $\log U = -0.5, 0, +0.5$, would imply an increase of $\overline{Xq(T)}$ to $\approx 5.65 \cdot 10^{-11} \text{ cm}^3 \text{ s}^{-1}$, by a factor ≈ 1.7 . Such increase in the efficiency in C IV production would only reinforce the conclusion on the weakness of the outflows at low- z .

Appendix C.2.3: Wind dynamical parameters

To estimate the wind dynamical parameters we assume the same simple model utilized for [O III] $\lambda\lambda 4959,5007$. The mass outflow rate is therefore given by:

$$\dot{M}_{\text{ion}} \approx 10 L_{\text{CIV},45}^{\text{out}} v_{5000} r_{1\text{pc}}^{-1} \left(\frac{Z}{5Z_{\odot}} \right)^{-1} n_{\text{H},9.5}^{-1} [\text{M}_{\odot} \text{ yr}^{-1}] \quad (\text{C.8})$$

where L_{45}^{out} is the luminosity of the blueshifted component in units of $10^{45} \text{ erg s}^{-1}$, the outflow velocity v_{5000} is scaled to 5000 km s^{-1} , the gas density is in units of $10^{9.5}$, and the radius is now in parsec units. For this paper, we assume that the CIV outflow is accelerated to a final, terminal velocity $v \approx c(1/2) + 2\sigma \approx c(1/2) + \text{FWHM}_{\text{BLUE}}/1.18$, where $c(1/2)$ corresponds to the centroid velocity at half intensity of the CIV BLUE component.

The thrust $\dot{M}_{\text{ion}} v$ and kinetic power can then be computed as:

$$\dot{M}_{\text{ion}} v \approx 3.15 \cdot 10^{35} L_{\text{CIV},45}^{\text{out}} v_{5000}^2 r_{1\text{pc}}^{-1} \left(\frac{Z}{5Z_{\odot}} \right)^{-1} n_{\text{H},9.5}^{-1} [\text{g cm s}^{-2}] \quad (\text{C.9})$$

$$\dot{E}_{\text{kin}} = \frac{1}{2} \dot{M}_{\text{ion}} v^2 \approx 7.9 \cdot 10^{43} L_{\text{CIV},45}^{\text{out}} v_{5000}^3 r_{1\text{pc}}^{-1} \left(\frac{Z}{5Z_{\odot}} \right)^{-1} n_{\text{H},9.5}^{-1} [\text{erg s}^{-2}] \quad (\text{C.10})$$

These expressions, used to calculate the dynamical parameters of the outflows for our low- z FOS sample, are quantitatively similar to the ones reported in earlier works (Marziani et al. 2016b, 2017). Those authors assumed an ad hoc temperature to account for the low CIV $\lambda 1549$ radiative efficiency of the emitting gas suggested by the observed low equivalent width of CIV $\lambda 1549$.

At high luminosity, for the ISAAC and HEMS samples, and by considering the results from the CLOUDY computations by using the more appropriate SED from Krawczyk et al. (2013) and for an estimated $\log U \approx -0.2$, and an efficiency, $\overline{Xq(T)} \approx 1.22 \cdot 10^{-10} \text{ cm}^3 \text{ s}^{-1}$ (see section C.2.2), Eqs. C.7, C.8, C.9, and C.10 should be divided by a factor ≈ 3.63 . Eqs. C.7, once the constants are divided by the factor reported above yields estimates that are in basic agreement with those of Vietri et al. (2020): they differ by a factor ~ 2 -3 in \dot{M}_{ion} , and the difference comes from the assumed efficiency of the CIV $\lambda 1549$ emission. Additional factors accounting for differences in the estimated values concern the geometry: a factor 3 from the assumption of a thin flat layer in place of a spherical surface element, and an additional factor of 2 for the unseen contribution of the receding cone enters in Eqs. C.7, C.8, C.9 and C.10.